

# RAMAN SPECTRA OF DISORDERED OXIDES FROM FIRST PRINCIPLES

THÈSE N° 2774 (2003)

PRÉSENTÉE À LA FACULTÉ SCIENCES DE BASE

Institut des théories des phénomènes physiques

SECTION DE PHYSIQUE

ÉCOLE POLYTECHNIQUE FÉDÉRALE DE LAUSANNE

POUR L'OBTENTION DU GRADE DE DOCTEUR ÈS SCIENCES

PAR

**Paolo UMARI**

laurea in fisica, Università degli Studi di Trieste, Italie  
et de nationalité italienne

acceptée sur proposition du jury:

Prof. A. Pasquarello, directeur de thèse

Prof. A. Baldereschi, rapporteur

Prof. F. Lévy, rapporteur

Prof. M. Parrinello, rapporteur

Prof. R. Resta, rapporteur

Lausanne, EPFL  
2003



# Abstract

This thesis is devoted to the study of Raman scattering from first-principles. We develop two different methods to calculate Raman spectra of large model structures.

The first method concerns the extension of the perturbative variational approach for the calculation of dielectric tensors to the case of ultrasoft pseudopotentials, allowing a significant improvement in the size of the affordable systems.

The second method permits to treat finite electric fields in Car-Parrinello molecular dynamics simulations with periodic boundary conditions. Applied to the calculation of Raman spectra, this approach, in the case of large systems, gives a further significant reduction of the computational effort required to obtain Raman spectra.

The methods we develop in the first part of the thesis are then applied to the study of vitreous silica and vitreous boron oxide. By applying our perturbative approach, we obtain the Raman spectrum for a model structure of vitreous silica. The accurate description of the Raman couplings allows us to derive an estimate from the experimental spectrum for the concentration of oxygen atoms in three- and four-membered rings.

Finally, we apply the finite field method to calculate the Raman spectrum of a large model structure of vitreous boron oxide. By investigating the contributions to the Raman spectrum from vibrations of different symmetry, we can extract from the experimental spectrum an estimate for the concentration of boron atoms belonging to three-membered rings.



# Compendio

Questa tesi é dedicata allo studio di diffusione Raman da principi primi. Nella prima parte della tesi sviluppiamo nuovi approcci teorici che vengono poi impiegati nella seconda parte per studiare spettri Raman di due materiali vetrosi: la silice amorfa (v-SiO<sub>2</sub>) e il triossido di boro amorfo (v-B<sub>2</sub>O<sub>3</sub>).

Il primo metodo teorico che sviluppiamo estende l'approccio perturbativo variazionale per il calcolo di tensori dielettrici al trattamento di pseudopotenziali di tipo *ultrasoft*. Con il secondo metodo, introduciamo uno schema generale per la trattazione di campi elettrici finiti in simulazioni di dinamica molecolare di tipo Car-Parrinello con condizioni al bordo periodiche.

Applicando il primo metodo teorico alla silice amorfa, calcoliamo lo spettro Raman per un modello strutturale precedentemente ottenuto da principi-primi. Grazie ad una accurata analisi delle proprietà microscopiche all'origine dello spettro Raman, siamo in grado di stimare la concentrazione in tale materiale di anelli contenenti tre e quattro atomi di ossigeno.

Il secondo metodo viene utilizzato per studiare lo spettro Raman di un modello di triossido di boro amorfo di grandi dimensioni. Anche in questo caso, l'informazione ottenuta da principi primi permette di ricavare dallo spettro sperimentale importanti informazioni strutturali; riusciamo, infatti, a stimare la concentrazione di anelli contenenti tre atomi di ossigeno.



# Contents

<b>1</b>	<b>Introduction</b>	<b>1</b>
1.1	Ring structures in disordered materials . . . . .	1
1.2	Brief description of Raman scattering . . . . .	4
1.3	First-principles modeling of disordered systems . . . . .	6
1.4	Outline of the thesis . . . . .	7
<b>2</b>	<b>Perturbational schemes for <math>\epsilon_\infty</math></b>	<b>9</b>
2.1	The PAW formalism for ultrasoft pseudopotentials . . . . .	10
2.2	Variational formalism for $\epsilon_\infty$ . . . . .	14
2.3	Implementation . . . . .	18
2.4	Application to small molecules: H <sub>2</sub> O, CH <sub>4</sub> , and NH <sub>3</sub> . . . . .	19
<b>3</b>	<b>Finite electric fields</b>	<b>25</b>
3.1	Introduction . . . . .	25
3.2	The method . . . . .	26
3.3	Application to bulk MgO . . . . .	30
3.4	Convergence of the dielectric constant with cell size . . . . .	36
3.5	Extension to ultrasoft pseudopotentials . . . . .	43
<b>4</b>	<b>Application to v-SiO<sub>2</sub></b>	<b>45</b>
4.1	Raman spectrum of $\alpha$ -quartz . . . . .	45
4.1.1	Theoretical formulation: Raman activities in crystals . . . . .	45

4.1.2	Raman scattering in $\alpha$ -quartz . . . . .	48
4.2	Raman spectrum of vitreous silica . . . . .	56
4.2.1	Theoretical formulation . . . . .	56
4.2.2	First-principles Raman spectrum of v-SiO <sub>2</sub> . . . . .	57
4.2.3	Concentration of three- and four-membered rings . . . . .	61
4.2.4	Comparison with the vibrational density of states . . . . .	63
<b>5</b>	<b>Application to v-B<sub>2</sub>O<sub>3</sub></b>	<b>69</b>
5.1	The structure . . . . .	69
5.2	Neutron static structure factor . . . . .	71
5.3	Vibrational density of states . . . . .	73
5.4	Infrared spectrum . . . . .	76
5.5	Raman spectrum . . . . .	78
5.6	Concentration of boroxol rings . . . . .	86
<b>6</b>	<b>Conclusions</b>	<b>91</b>
<b>A</b>	<b>Local Models for Raman susceptibilities</b>	<b>93</b>
A.1	Bond polarizability model . . . . .	93
A.2	Model dependent on local symmetry . . . . .	95
A.3	Transferability . . . . .	98
<b>B</b>	<b>Minimization of second order variational functionals</b>	<b>103</b>



# Chapter 1

## Introduction

### 1.1 Ring structures in disordered materials

Materials which do not exhibit translational symmetry are referred to as disordered. In this thesis we address topological disorder consisting in a nonperiodic atomic structure. In contrast to the case of crystalline materials where the structural properties can be easily determined experimentally, the characterization of the structure remains challenging for disordered materials. Experiments alone are not sufficient to provide a complete atomic-scale description and accurate theoretical modeling is required to properly analyze experimental probes. This thesis is devoted to the study of two disordered oxides: vitreous silica ( $v\text{-SiO}_2$ ) and vitreous boron trioxide ( $v\text{-B}_2\text{O}_3$ ).

The structure of such disordered materials is usually described by considering specific order properties at different scale lengths. The order in which the first neighbor atoms are disposed is usually referred to as short range order. In covalent-bonded materials, such as in  $v\text{-SiO}_2$  and  $v\text{-B}_2\text{O}_3$ , the geometry of the first coordination shell is well determined: in  $v\text{-SiO}_2$  the silicon atom is tetrahedrally bonded with four oxygen atoms, in  $v\text{-B}_2\text{O}_3$  the boron atom occupies the center of a symmetric planar  $\text{BO}_3$  triangle.

As far as the long-range order is concerned, the current understanding of such materials is based on the concept of continuous random network [1]. The structural basic units, such as the  $\text{SiO}_4$  tetrahedra in vitreous silica and the  $\text{BO}_3$  triangles in boron oxide are arranged

in a non periodic way by varying the Si-O-Si and the B-O-B angles which bridge different units in  $v\text{-SiO}_2$  and in  $v\text{-B}_2\text{O}_3$ , respectively (see Fig. 1.1).

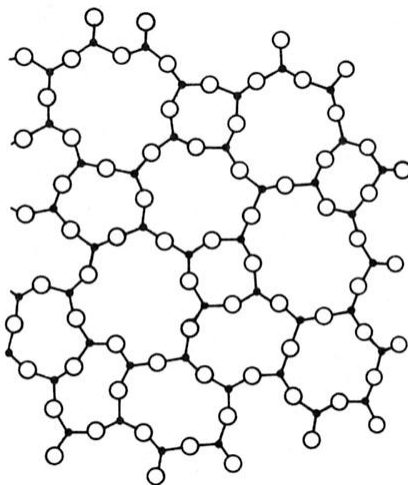


Figure 1.1: Continuous random network model, reduced on a plane, for  $v\text{-B}_2\text{O}_3$ .

At intermediate range distances, the disordered network can be characterized in terms of the statistics of closed rings using the shortest path analysis [2]. For every given silicon (boron) atom, one considers the shortest closed paths along the network bonds, which contain the given atom. The number of encountered oxygen atoms along the path specifies the size of the ring.

In  $v\text{-SiO}_2$ , the presence of small rings has long been debated. Finally two sharp defect lines (known as  $D_1$  and  $D_2$ ) [3, 4] in the Raman spectrum have definitely been assigned to breathing vibrations of oxygen atoms in four- and three-membered ring structures, respectively [5, 6] (see Fig. 1.2). However, other vibrational spectroscopy techniques, such as infrared [7] and inelastic neutron scattering [8] spectroscopies do not present any trace of these small rings. Hence, an accurate theoretical description of Raman spectra is required to evaluate the concentration of three- and four-fold rings in  $v\text{-SiO}_2$ , which are in principle related to the intensities of the defect lines.

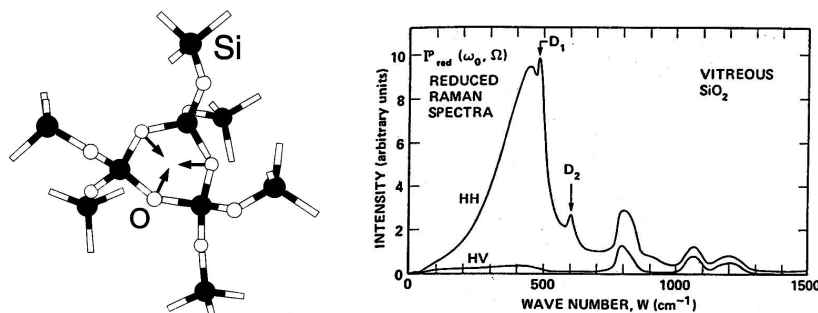


Figure 1.2: The breathing mode of oxygen atoms in three-fold rings is responsible for the  $D_2$  line in the Raman spectrum of  $v\text{-SiO}_2$  [6].

In  $v\text{-B}_2\text{O}_3$ , breathing vibrations of oxygen atoms in planar three-membered rings have been proved to be responsible for the very strong sharp line at  $\sim 800\text{ cm}^{-1}$  in the Raman spectrum [9] (see Fig. 1.3). The concentration of such rings, called boroxol rings, has long been debated, with estimations for the concentration of boron atoms belonging to boroxol rings varying from 0% to 80%. The fraction of 0% was derived from the analysis of a continuous random network [10]. Based on reverse Monte Carlo analysis of neutron and x-ray diffraction spectra a fraction of 20-30% was estimated [11, 12]. Finally, nuclear magnetic resonance [13] and neutron diffraction studies [14] are consistent with a fraction of 80%.

Because of the high sensitivity of the Raman spectrum to small rings structures embedded in the disordered network in  $v\text{-SiO}_2$  and  $v\text{-B}_2\text{O}_3$ , a quantitative description of the intermediate range order can in principle be achieved by an accurate theoretical modeling of the Raman scattering in these glasses. In particular, this analysis could determine the concentrations of three- and four-fold rings in  $v\text{-SiO}_2$  and of boroxol rings in  $v\text{-B}_2\text{O}_3$ . This is the aim of this thesis.

The theoretical framework accounting for Raman scattering in solids and molecules has been well established for a long time (for a review see Ref. [16]). In this thesis, we

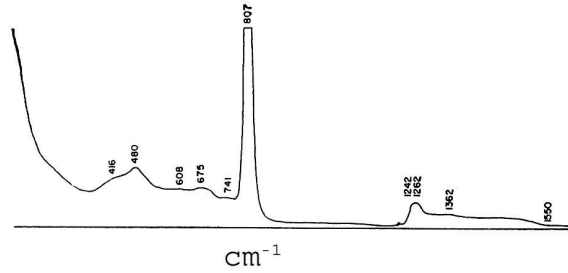


Figure 1.3: The breathing mode of oxygen atoms in boroxol rings embedded in the structure of  $v\text{-B}_2\text{O}_3$  are responsible for the strong line at  $\sim 800 \text{ cm}^{-1}$  in the Raman spectrum. Data from Ref.[15]

apply appropriate methods to study the quantities involved in the formulation of Raman scattering cross sections for materials as  $v\text{-SiO}_2$  and  $v\text{-B}_2\text{O}_3$ .

## 1.2 Brief description of Raman scattering

The inelastic scattering of light by vibrational excitations takes the name of Raman scattering. At first order, an incoming photon of frequency  $\omega_L$  and of polarization  $\mathbf{e}_L$  is scattered by creating (or annihilating) a vibrational excitation (a phonon in solid materials) of frequency  $\omega_k$  and an outgoing photon of frequency  $\omega_S$  and of polarization  $\mathbf{e}_S$  (see Fig. 1.4).

If the phonon is created (annihilated) the scattering process is referred to as a Stokes (anti-Stokes) process. The energy conservation during the process implies that the frequency of the outgoing photon is  $\omega_S = \omega_L + \omega_k$  in the Stokes process and  $\omega_S = \omega_L - \omega_k$  in the anti-Stokes one. Because of the large difference between photon wavelengths and crystal periodicity, the momentum conservation implies that, in crystals, only phonons with a  $\mathbf{k}$  vector close to the center of the Brillouin zone can participate to first-order Raman processes. By contrast, because of the lack of translational periodicity, all vibrational

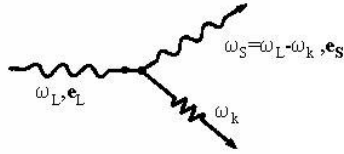


Figure 1.4: Sketch of a first order anti-Stokes Raman scattering process: a photon of frequency  $\omega_L$  and polarization  $\mathbf{e}_L$  is scattered into a photon of frequency  $\omega_S = \omega_L - \omega_k$  and polarization  $\mathbf{e}_S$  and a phonon of frequency  $\omega_k$ .

excitations in disordered solids contribute to first-order Raman processes.

Raman spectra are usually recorded with a specific choice for the polarization of the incoming  $\mathbf{e}_L$  and outgoing  $\mathbf{e}_S$  photons. In disordered materials the observed polarizations are usually taken parallel (HH or horizontal-horizontal case) or perpendicular (HV or horizontal-vertical case). An explicit derivation of the Raman scattering cross-section can be derived assuming the Placzek approximation [17]: the exciting frequency  $\omega_L$  is inferior to any electronic excitation energy and the adiabatic approximation applies. In this limit, the power Raman anti-Stokes cross-section reads (in esu units):

$$\frac{d\sigma}{d\Omega} = \frac{\omega_S^4 V}{c^4} \left| \mathbf{e}_S \cdot \frac{d\chi}{d\xi} \cdot \mathbf{e}_L \right|^2 \frac{\hbar}{2\omega_k} (n_k + 1), \quad (1.1)$$

where  $V$  is the volume of the scattering sample,  $c$  is the speed of light, and  $n_k$  is the Boson factor,

$$n_k = \frac{1}{\exp(\hbar\omega_k/k_B T) - 1}. \quad (1.2)$$

The tensor  $d\chi/d\xi$  is the derivative of the dielectric susceptibility tensor  $\chi$  with respect to the phonon displacement  $\xi$ . For the Stokes process the statistical factor in Eq. (1.1) becomes  $n_k$ . Because of technical difficulties, the intensity of Raman spectra of solid materials are usually only given on an arbitrary scale.

From Eq. (1.1), one can see that the ingredients required to model Raman spectra are (i) a description of the structure, (ii) a description of the vibrational properties, and (iii) a description of how the dielectric susceptibility depends on the vibrational excitations. The

dielectric susceptibility is defined as a second order derivative of the energy with respect to an applied static homogeneous electric field. In this thesis, we model the Raman spectra of  $v\text{-SiO}_2$  and  $v\text{-B}_2\text{O}_3$  by calculating all these ingredients using a first-principles approach.

### 1.3 First-principles modeling of disordered systems

A reliable modeling of the atomic structure of a disordered material requires an accurate description of the interatomic interactions. Such a careful description of the chemical bonding can be achieved by the precise characterization of the electronic structure obtained from first-principles density functional approaches. Furthermore, the application of perturbation theory to density functional schemes [19] allows one to obtain by first-principles the dielectric properties which are necessary for the calculation of Raman spectra.

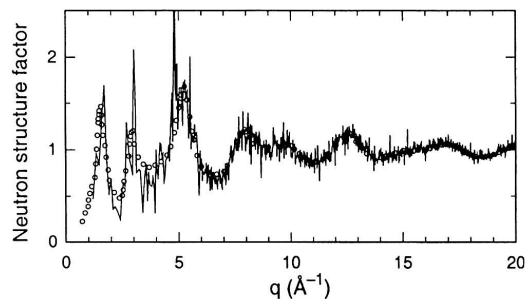


Figure 1.5: Total neutron structure factor for a model structure of  $v\text{-SiO}_2$ : comparison between simulation (solid) and experiment (open dots) [21].

The Car-Parrinello method [18], in which the electronic and the ionic degrees of freedom evolve simultaneously as a function of time, opened the way to first-principles molecular dynamics simulations of systems of reasonable size. Furthermore, the combination of the Car-Parrinello method with ultrasoft pseudopotentials [20] permitted the treatment of oxide systems at an affordable computational cost. In the ultrasoft scheme the interaction

between the valence and the core electrons is described by a nonlocal potential and the valence charge is expressed in terms of the expectation value of a nonlocal operator. The advantage of this scheme is that the wave functions are smoother than in previous methods. When the wave functions are expanded on a plane-wave basis set, this results in the use of a smaller number of plane-waves. Using these techniques, liquid and vitreous  $\text{SiO}_2$  were simulated by first principles molecular dynamics [21]. By quenching to low temperatures a model of liquid silica, a model of  $v\text{-SiO}_2$  was obtained. This model showed excellent structural and vibrational properties (see Fig. 1.5). Furthermore, the theoretical inelastic neutron scattering response [22] and infrared absorption spectrum [23], for this model structure, were found in good agreement with their experimental counterparts.

In order to extend the comparison with experimental vibrational spectroscopies, it is therefore of interest to calculate within a first-principles approach the Raman spectrum for the same model of  $v\text{-SiO}_2$ . Similarly, it is of interest and to apply the same techniques for investigating the structural and vibrational properties of  $v\text{-B}_2\text{O}_3$ . For this purpose, it is necessary to formulate a theoretical scheme to obtain dielectric properties, i.e. the dielectric tensors for a scheme based on ultrasoft pseudopotentials.

## 1.4 Outline of the thesis

This thesis concerns both the introduction of new general methods to calculate by first-principles the dielectric response of solids and the application of these methods to the study of  $v\text{-SiO}_2$  and  $v\text{-B}_2\text{O}_3$ . On the theory side, we, first, extend a variational formulation [24] for the second derivative of the energy with respect to an applied static electric field to the case of ultrasoft pseudopotentials. Then, we introduce a new general method to treat finite homogeneous electric fields in density functional calculations with periodic boundary conditions [25]. With this approach it is possible to obtain easily Raman couplings avoiding the use of perturbational schemes. On the application side, we first study, for evaluating the accuracy of first-principles approaches, the Raman spectra of crystalline  $\text{SiO}_2$  polymorphs, finding good agreement with experimental results [26]. Subsequently, we apply the variational method we developed to our model of  $v\text{-SiO}_2$ . By investigating at

the atomic level the calculated Raman spectrum, we can estimate from the *experimental* Raman spectrum the concentration of three- and four-fold rings in this glass [27]. The new method for treating finite electric fields is applied to calculate the infrared and Raman spectra for a model structure of v-B<sub>2</sub>O<sub>3</sub> previously obtained within our research group [A. Pasquarello, unpublished]. For this large system (160 atoms), we present a complete analysis of the structural and vibrational properties. Similarly to the case of v-SiO<sub>2</sub>, we are able to estimate from the *experimental* Raman spectrum the concentration of boroxol rings.

The thesis is organized as follows: in Chapter 2, we present a method based on the theory of perturbations to calculate dielectric tensors in the case of ultrasoft pseudopotentials. In Chapter 3, we present a new method allowing the treatment of finite homogeneous electric fields in density functional calculation with periodic boundary conditions. Chapter 4 is devoted to the study of v-SiO<sub>2</sub> using the method explained in Chapter 2. In Chapter 5, we present a complete first-principles study of v-B<sub>2</sub>O<sub>3</sub>. The dielectric properties are obtained by applying the method described in Chapter 3. Finally, the conclusions are drawn in Chapter 6.



## Chapter 2

# Perturbational schemes for $\epsilon_\infty$

In this chapter, we extend the variational formulation for the calculation of dielectric tensors in periodic solids [24] to the case of ultrasoft pseudopotentials (US) [20]. We adopt the following strategy: first, we consider the general *all-electron* expression for the second order variational energy functional with respect to the electric field of Ref. [24], which permits to calculate the high-frequency dielectric tensor. Then, we introduce in this expression pseudopotentials by using the same formalism introduced by P.E. Blöchl in the projector augmented-wave (PAW) method [28]. Our method is fully general and can also be applied to the projector augmented-wave method. A similar approach was applied in Ref. [23] for the calculation of effective Born charges and in Ref. [29] for investigating the NMR response. Our approach differs from that of Ref. [56], where, for calculating vibrational properties, a perturbative scheme is directly applied to an *unperturbed* Hamiltonian expressed in terms of ultrasoft pseudopotentials. We report some details regarding the implementation of this scheme in a new computer code based on the code described in Ref. [20]. Results for Raman intensities of the water, the methane, and the ammonia molecule illustrate the accuracy of this new approach.

## 2.1 The PAW formalism for ultrasoft pseudopotentials

In an important paper, P.E. Blöchl introduced the projector augmented-wave method [28] which extended both the linear augmented-wave method [30] and the pseudopotential method. In particular, the ultrasoft pseudopotential method [31, 20] can be expressed in a clear and concise form by adopting the PAW formalism.

We consider an electronic system describing the interaction with a single ionic core. The valence *all-electron* wave functions  $\Psi_i$  present strong oscillations inside the core region. To deal with smoother wave functions inside a core region defined by a distance  $R$  from the nucleus, we introduce a linear operator  $T$ :

$$T = 1 + \sum_i (|\Phi_i\rangle - |\tilde{\Phi}_i\rangle)\langle\beta_i|, \quad (2.1)$$

where the all-electron and pseudo atomic wave functions  $\Phi_i$  and  $\tilde{\Phi}_i$  coincide outside the core. Inside the core region the projectors  $\beta_i$  satisfy the following completeness relation:

$$\sum_i |\tilde{\Phi}_i\rangle\langle\beta_i| = 1. \quad (2.2)$$

The *all-electron* wave functions  $\Psi_i$  can be expressed in terms of the *pseudo* wave functions  $\tilde{\Psi}_i$ :

$$|\Psi_i\rangle = T|\tilde{\Psi}_i\rangle. \quad (2.3)$$

The *pseudo* wave functions match the corresponding *all-electron* ones outside the core and are smoother inside the core region. Any operator  $A$  acting on the space of the all-electron wave functions can be evaluated by evaluating the *pseudo* operator  $\tilde{A}$ , directly on the pseudo wave functions:

$$\begin{aligned} \langle\Psi_i|A|\Psi_j\rangle &= \langle\tilde{\Psi}_i|T^\dagger AT|\tilde{\Psi}_j\rangle \\ &= \langle\tilde{\Psi}_i|\tilde{A}|\tilde{\Psi}_j\rangle, \end{aligned} \quad (2.4)$$

where the *pseudo* operator  $\tilde{A}$  is defined as  $T^\dagger AT$ . When the operator  $A$  is quasilocal (i.e. it depends locally on the wave functions and locally on the space derivatives of the wave functions), the respective pseudo-operator  $\tilde{A}$  is given by [28]:

$$\tilde{A} = A + \sum_{i,j} |\beta_i\rangle (\langle \Phi_i | A | \Phi_j \rangle - \langle \tilde{\Phi}_i | A | \tilde{\Phi}_j \rangle) \langle \beta_j|. \quad (2.5)$$

Eq. (2.5) is based on the completeness relation in Eq. (2.2). The ground state of the system can be found by minimizing with respect to the pseudo wave functions the energy functional:

$$E = \sum_i \langle \tilde{\Psi}_i | \tilde{H} | \tilde{\Psi}_i \rangle, \quad (2.6)$$

where  $\tilde{H} = T^\dagger HT$  is the pseudo-Hamiltonian operator and the pseudo-wave functions must satisfy the constraints:

$$\langle \tilde{\Psi}_i | S | \tilde{\Psi}_j \rangle = \delta_{ij}, \quad (2.7)$$

where  $S$  is the pseudo-identity operator  $T^\dagger T$ . In the ultrasoft pseudopotential scheme (US) [31, 20] only a finite set of projectors  $\beta_i$  is considered, and the pseudo-operators are obtained by applying Eq. (2.5) [32]. The pseudo density operator  $|\mathbf{r}\rangle\langle\mathbf{r}|$  is usually referred to as  $K(\mathbf{r})$  in the US scheme, and is defined on the basis of Eq. (2.5) as:

$$K(\mathbf{r}) = |\mathbf{r}\rangle\langle\mathbf{r}| + \sum_{i,j} |\beta_i\rangle Q_{i,j}(\mathbf{r}) \langle \beta_j|, \quad (2.8)$$

where the augmentation functions  $Q_{i,j}$  are defined as:

$$Q_{i,j}(\mathbf{r}) = \Phi_i^*(\mathbf{r})\Phi_j(\mathbf{r}) - \tilde{\Phi}_i^*(\mathbf{r})\tilde{\Phi}_j(\mathbf{r}). \quad (2.9)$$

For a generic all-electron Hamiltonian  $H$  with an external local potential  $V_{loc}$ :

$$H = -\frac{\hbar^2}{2m}\nabla^2 + V_{loc}(\mathbf{r}), \quad (2.10)$$

the pseudo Hamiltonian, adopting the US notation of Ref. [20], reads:

$$\tilde{H} = H + \sum_{i,j} |\beta_i\rangle D_{i,j} \langle \beta_j|, \quad (2.11)$$

where

$$\begin{aligned} D_{i,j} &= D_{i,j}^0 + \int_R Q_{i,j}(\mathbf{r}) V_{loc}(\mathbf{r}) d\mathbf{r} \\ D_{i,j}^0 &= -\frac{\hbar^2}{2m} \int_R \left[ \Phi_i^*(\mathbf{r}) \nabla^2 \Phi_j(\mathbf{r}) + \tilde{\Phi}_i^*(\mathbf{r}) \nabla^2 \tilde{\Phi}_j(\mathbf{r}) \right] d\mathbf{r}, \end{aligned}$$

where  $R$  denotes that the integral is limited to the core region inside the radius  $R$ .

*Normconserving* pseudopotentials can be expressed by adopting the same formalism. For these pseudopotentials, the total pseudocharge in the core region is equal to the corresponding all-electron charge. This implies that:

$$\int_R \Phi_i^*(\mathbf{r}) \Phi_j(\mathbf{r}) d\mathbf{r} = \int_R \tilde{\Phi}_i^*(\mathbf{r}) \tilde{\Phi}_j(\mathbf{r}) d\mathbf{r} \quad (2.12)$$

Hence, the operator  $S = T^\dagger T$  becomes the identity operator. While the pseudo-kinetic operator  $\tilde{\nabla}^2$  is obtained by Eq. (2.5), the pseudo density operator  $|\mathbf{r}\rangle\langle\mathbf{r}|$  is further approximated to be identical to the all-electron one:  $|\mathbf{r}\rangle\langle\mathbf{r}| = |\mathbf{r}\rangle\langle\mathbf{r}|$ . More generally, the pseudo-wave functions are treated in the *normconserving* scheme in the same way as all-electron ones and the pseudo-Hamiltonian differs from the all-electron Hamiltonian by the presence of the  $D_{ij}^0$  term. The complete PAW formalism further differs from pseudopotential formalisms for the treatment of *core* electrons, which are not explicitly treated in pseudopotential schemes [32]. Here, the PAW formalism will be applied only to *valence* electrons.

The PAW formalism for US pseudopotentials can be extended to the case of a periodic (crystalline) system. According to the Bloch theorem, the *all-electron* wave functions can be written as:

$$\Psi_{\mathbf{k},i}(\mathbf{r}) = (2\pi)^{3/2} (\Omega)^{-1/2} e^{i\mathbf{k}\cdot\mathbf{r}} u_{\mathbf{k},i}(\mathbf{r}), \quad (2.13)$$

where  $\Omega$  is the volume of the primitive cell,  $\mathbf{k}$  belongs to the Brillouin zone, and  $u_{\mathbf{k},i}$  are the *all-electron* periodic wave functions. The valence charge density is periodic and is expressed, in units of electrons per cell, by:

$$n(\mathbf{r}) = \frac{\Omega}{(2\pi)^3} \int \sum_v u_{\mathbf{k},v}^*(\mathbf{r}) u_{\mathbf{k},v}(\mathbf{r}) d\mathbf{k}, \quad (2.14)$$

where the integral is limited on the Brillouin zone, and the index  $v$  runs over the valence states. Any operator  $A$  can be expressed as acting on the Hilbert space of periodic functions  $u_{\mathbf{k}}(\mathbf{r})$  like:

$$A_{\mathbf{k},\mathbf{k}'}(\mathbf{r}, \mathbf{r}') = e^{i\mathbf{k}\cdot\mathbf{r}} A(\mathbf{r}, \mathbf{r}') e^{-i\mathbf{k}'\cdot\mathbf{r}'} \quad (2.15)$$

The Hamiltonian operator is cell periodic. Therefore, it is diagonal when expressed on Bloch states.

For a periodic system the  $T$  operator reads:

$$T = 1 + \sum_{\mathbf{R},\alpha,i} \left( |\Phi_{\mathbf{R},\alpha,i}\rangle - |\tilde{\Phi}_{\mathbf{R},\alpha,i}\rangle \right) \langle \beta_{\mathbf{R},\alpha,i}| \quad (2.16)$$

where the vector  $\mathbf{R}$  describes the periodic lattice and the index  $\alpha$  runs over the ionic cores in the primitive cell. The functions  $\Phi_{\mathbf{R},\alpha,i}$  and  $\tilde{\Phi}_{\mathbf{R},\alpha,i}$  are centered on the ionic cores in the primitive cell and obey the following translational property:

$$\begin{cases} \Phi_{i,\mathbf{R},\alpha}(\mathbf{r} - (\mathbf{R} + \tau_{\alpha})) = \Phi_{\alpha,i}(\mathbf{r}) \\ \tilde{\Phi}_{i,\mathbf{R},\alpha}(\mathbf{r} - (\mathbf{R} + \tau_{\alpha})) = \tilde{\Phi}_{\alpha,i}(\mathbf{r}) \\ \beta_{i,\mathbf{R},\alpha}(\mathbf{r} - (\mathbf{R} + \tau_{\alpha})) = \beta_{\alpha,i}(\mathbf{r}), \end{cases} \quad (2.17)$$

where  $\mathbf{R} + \tau_{\alpha}$  is the position of the ion  $\alpha$  in the cell labeled by the vector  $\mathbf{R}$ . The operator  $T$  has the periodicity of the lattice, and becomes diagonal when expressed on a basis set of periodic functions  $u_{\mathbf{k}}(\mathbf{r})$  as in Eq. (2.15). Hence, periodic *pseudo* wave functions  $\tilde{u}_{\mathbf{k},i}$  are defined in a straightforward way:

$$|u_{\mathbf{k},i}\rangle = T_{\mathbf{k},\mathbf{k}} |\tilde{u}_{\mathbf{k},i}\rangle. \quad (2.18)$$

Thus, the *all-electron* wave functions  $\Psi_{\mathbf{k},i}$  can be expressed in terms of periodic *pseudo* wave functions:

$$\begin{cases} |\Psi_{\mathbf{k},i}\rangle = T |\tilde{\Psi}_{\mathbf{k},i}\rangle \\ \tilde{\Psi}_{\mathbf{k},i}(\mathbf{r}) = (2\pi)^{3/2} (\Omega)^{-1/2} e^{i\mathbf{k}\cdot\mathbf{r}} \tilde{u}_{\mathbf{k},i}(\mathbf{r}) \end{cases} \quad (2.19)$$

To simplify the notation, we indicate in the following with  $A_{\mathbf{k}}$  the diagonal term  $A_{\mathbf{k},\mathbf{k}}$  of a generic operator  $A$ .

We define the following functions having Bloch symmetry:

$$\begin{aligned} |\Phi_{i,\mathbf{R},\alpha,\mathbf{k}}\rangle &= e^{-i\mathbf{k}(\mathbf{r}-\mathbf{R})} |\Phi_{i,\mathbf{R},\alpha}\rangle \\ |\tilde{\Phi}_{i,\mathbf{R},\alpha,\mathbf{k}}\rangle &= e^{-i\mathbf{k}(\mathbf{r}-\mathbf{R})} |\tilde{\Phi}_{i,\mathbf{R},\alpha}\rangle \\ |\beta_{i,\mathbf{R},\alpha,\mathbf{k}}\rangle &= e^{-i\mathbf{k}(\mathbf{r}-\mathbf{R})} |\beta_{i,\mathbf{R},\alpha}\rangle. \end{aligned} \quad (2.20)$$

The operator  $T_{\mathbf{k}}$  can be expressed directly as:

$$T_{\mathbf{k}} = 1 + \sum_{i,\mathbf{R},\alpha} \left( |\Phi_{i,\mathbf{R},\alpha,\mathbf{k}}\rangle - |\tilde{\Phi}_{i,\mathbf{R},\alpha,\mathbf{k}}\rangle \right) \langle \beta_{i,\mathbf{R},\alpha,\mathbf{k}}|. \quad (2.21)$$

The completeness relation of Eq. (2.2) can be written for every vector  $\mathbf{k}$  as:

$$\sum_i |\tilde{\Phi}_{i,\mathbf{R},\alpha,\mathbf{k}}\rangle \langle \beta_{i,\mathbf{R},\alpha,\mathbf{k}}| = 1, \quad (2.22)$$

and for a quasilocal operator  $A$  a relation equivalent to that of Eq. (2.5) holds:

$$\begin{aligned} T_{\mathbf{k}}^\dagger A_{\mathbf{k}} T_{\mathbf{k}} &= A_{\mathbf{k}} + \sum_{i,j,\mathbf{R},\alpha} \left( |\beta_{i,\mathbf{R},\alpha,\mathbf{k}}\rangle \left( \langle \Phi_{i,\mathbf{R},\alpha,\mathbf{k}}| A_{\mathbf{k}} | \Phi_{j,\mathbf{R},\alpha,\mathbf{k}}\rangle \right. \right. \\ &\quad \left. \left. - \langle \tilde{\Phi}_{i,\mathbf{R},\alpha,\mathbf{k}}| A_{\mathbf{k}} | \tilde{\Phi}_{j,\mathbf{R},\alpha,\mathbf{k}}\rangle \right) \langle \beta_{j,\mathbf{R},\alpha,\mathbf{k}}| \right). \end{aligned} \quad (2.23)$$

## 2.2 Variational formalism for $\epsilon_\infty$

The dielectric tensor  $\epsilon_\infty$  is determined by the second order derivative of the electronic energy with respect to the electric field [33]:

$$\epsilon_{\infty,\alpha,\beta} = \delta_{\alpha,\beta} - 4\pi \frac{\partial^2 E}{\partial \mathcal{E}_\alpha \partial \mathcal{E}_\beta}, \quad (2.24)$$

where the indices  $\alpha$  and  $\beta$  run over the Cartesian directions of the electric field  $\mathcal{E}$ . The second order derivatives  $\frac{\partial^2 E}{\partial \mathcal{E}_\alpha^2}$ , which do not mix electric fields of different directions, can be found by minimizing with respect to the first order *all-electron* periodic wave functions  $\frac{\partial}{\partial \mathcal{E}_\alpha} u_{\mathbf{k},v}^0$  the selfconsistent variational functional described in Ref. [24]:

$$\begin{aligned} \frac{\partial^2 E}{\partial \mathcal{E}_\alpha^2} &= \frac{\Omega}{(2\pi)^3} \int_{BZ} \sum_v \left( \left\langle \frac{\partial}{\partial \mathcal{E}_\alpha} u_{\mathbf{k},v}^0 \middle| H^0 - \epsilon_{\mathbf{k},v}^0 \middle| \frac{\partial}{\partial \mathcal{E}_\alpha} u_{\mathbf{k},v}^0 \right\rangle \right. \\ &\quad \left. + \left\langle \frac{\partial}{\partial \mathcal{E}_\alpha} u_{\mathbf{k},v}^0 \middle| i \frac{\partial}{\partial k_\alpha} u_{\mathbf{k},v}^0 \right\rangle + \left\langle i \frac{\partial}{\partial k_\alpha} u_{\mathbf{k},v}^0 \middle| \frac{\partial}{\partial \mathcal{E}_\alpha} u_{\mathbf{k},v}^0 \right\rangle \right) d\mathbf{k} \\ &\quad + \frac{1}{2} \int \frac{n^1(\mathbf{r})n^1(\mathbf{r}')}{|\mathbf{r}-\mathbf{r}'|} d\mathbf{r}d\mathbf{r}' + \int \frac{\delta V_{xc}}{\delta n} \Big|_{n^0} (n^1(\mathbf{r}))^2 d\mathbf{r}, \end{aligned} \quad (2.25)$$

where the index  $v$  runs over the valence wave functions,  $H^0$  is the unperturbed Hamiltonian operator,  $u_{\mathbf{k},v}^0$  are the unperturbed periodic ground state wave functions of energy  $\epsilon_{\mathbf{k},v}^0$ ,  $V_{xc}$  is the exchange-correlation potential, which, for simplicity, is taken as in the local density approximation,  $n^0$  is the unperturbed charge density, and  $n^1$  is the first-order derivative of the charge density defined as:

$$n^1(\mathbf{r}) = \frac{\Omega}{(2\pi)^3} \int_{BZ} \sum_v \left( u_{\mathbf{k},v}^{0*}(\mathbf{r}) \frac{\partial}{\partial \mathcal{E}_\alpha} u_{\mathbf{k},v}^0(\mathbf{r}) + \frac{\partial}{\partial \mathcal{E}_\alpha} u_{\mathbf{k},v}^{0*}(\mathbf{r}) u_{\mathbf{k},v}^0(\mathbf{r}) \right) d\mathbf{k}. \quad (2.26)$$

The first order wave functions  $\frac{\partial}{\partial \mathcal{E}_\alpha} u_{\mathbf{k},v}^0$  must satisfy the constraints:

$$\left\langle \frac{\partial}{\partial \mathcal{E}_\alpha} u_{\mathbf{k},v}^0 | u_{\mathbf{k},v'}^0 \right\rangle + \left\langle u_{\mathbf{k},v'}^0 | \frac{\partial}{\partial \mathcal{E}_\alpha} u_{\mathbf{k},v}^0 \right\rangle = 0, \quad (2.27)$$

The derivatives of the wave functions  $u_{\mathbf{k},v}^0$  with respect to  $k_\alpha$  can be calculated by minimizing with respect to the first-order wave functions  $\frac{\partial}{\partial k_\alpha} u_{\mathbf{k},v}^0$  the following non-selfconsistent variational functional [24]:

$$\begin{aligned} E^2[u_{\mathbf{k},v}^0, \frac{\partial}{\partial k_\alpha} u_{\mathbf{k},v}^0] &= \left\langle \frac{\partial}{\partial k_\alpha} u_{\mathbf{k},v}^0 | H_{\mathbf{k}}^0 - \epsilon_{\mathbf{k},v}^0 | \frac{\partial}{\partial k_\alpha} u_{\mathbf{k},v}^0 \right\rangle \\ &+ \left\langle u_{\mathbf{k},v}^0 | \frac{\partial}{\partial k_\alpha} H_{\mathbf{k}}^0 | \frac{\partial}{\partial k_\alpha} u_{\mathbf{k},v}^0 \right\rangle + \left\langle \frac{\partial}{\partial k_\alpha} u_{\mathbf{k},v}^0 | \frac{\partial}{\partial k_\alpha} H_{\mathbf{k}}^0 | u_{\mathbf{k},v}^0 \right\rangle, \end{aligned} \quad (2.28)$$

where the first order wave functions must satisfy the constraints:

$$\left\langle u_{\mathbf{k},v'}^0 | \frac{\partial}{\partial k_\alpha} u_{\mathbf{k},v}^0 \right\rangle + \left\langle \frac{\partial}{\partial k_\alpha} u_{\mathbf{k},v}^0 | u_{\mathbf{k},v'}^0 \right\rangle = 0. \quad (2.29)$$

A nonvariational functional then gives access to the mixed terms  $\frac{\partial^2 E_{\text{tot}}}{\partial \mathcal{E}_\alpha \partial \mathcal{E}_\beta}$  [24]:

$$\frac{\partial^2 E_{\text{tot}}}{\partial \mathcal{E}_\alpha \partial \mathcal{E}_\beta} = \frac{\Omega}{2(2\pi)^3} \int_{BZ} \sum_v \left( \left\langle \frac{\partial}{\partial \mathcal{E}_\alpha} u_{\mathbf{k},v}^0 | i \frac{\partial}{\partial k_\beta} u_{\mathbf{k},v}^0 \right\rangle + \left\langle i \frac{\partial}{\partial k_\alpha} u_{\mathbf{k},v}^0 | \frac{\partial}{\partial \mathcal{E}_\beta} u_{\mathbf{k},v}^0 \right\rangle \right) d\mathbf{k}. \quad (2.30)$$

The variational functional in Eq. (2.25) can also be found with a conventional perturbation scheme, as given in Ref [19]. The perturbation induced by a homogeneous static electric field  $-\mathbf{E} \cdot \mathbf{r}_\alpha$  is in principle ill-defined for a periodic solid. Nevertheless, the first order wave functions can be taken orthogonal to the unperturbed valence wave functions, so that, only off-diagonal terms appear in the functional for the second order derivatives of the energy with respect to the field:

$$\left\langle \frac{\partial}{\partial \mathcal{E}_\alpha} \Psi_{\mathbf{k},v}^0 | r_\alpha | \Psi_{\mathbf{k},v}^0 \right\rangle. \quad (2.31)$$

Following Ref. [19], this term can be written as:

$$\begin{aligned} \left\langle \frac{\partial}{\partial \mathcal{E}_\alpha} \Psi_{\mathbf{k},v}^0 | r_\alpha | \Psi_{\mathbf{k},v}^0 \right\rangle &= \left\langle \frac{\partial}{\partial \mathcal{E}_\alpha} \Psi_{\mathbf{k},v}^0 \sum_c |\Psi_{\mathbf{k},c}^0\rangle \langle \Psi_{\mathbf{k},c}^0| \frac{(\epsilon_{\mathbf{k},c}^0 - \epsilon_{\mathbf{k},v}^0)}{(\epsilon_{\mathbf{k},c}^0 - \epsilon_{\mathbf{k},v}^0)} r_\alpha | \Psi_{\mathbf{k},v}^0 \right\rangle \\ &= \left\langle \frac{\partial}{\partial \mathcal{E}_\alpha} \Psi_{\mathbf{k},v}^0 \sum_c |\Psi_{\mathbf{k},c}^0\rangle \langle \Psi_{\mathbf{k},c}^0| \frac{[H^0, r_\alpha]}{(\epsilon_{\mathbf{k},c}^0 - \epsilon_{\mathbf{k},v}^0)} | \Psi_{\mathbf{k},v}^0 \right\rangle, \end{aligned} \quad (2.32)$$

where the index  $c$  runs over the unoccupied states. By considering  $H_{\mathbf{k}} = e^{i\mathbf{k}\cdot\mathbf{r}} H e^{-i\mathbf{k}\cdot\mathbf{r}}$ , and by applying the theory of perturbations, we can now find the same terms appearing in Eq. (2.25):

$$\begin{aligned} \langle u_{\mathbf{k},c}^0 | \frac{[H^0, r_\alpha]_{\mathbf{k}}}{(\epsilon_{\mathbf{k},c}^0 - \epsilon_{\mathbf{k},v}^0)} | u_{\mathbf{k},v}^0 \rangle &= -i \langle u_{\mathbf{k},c}^0 | \frac{\frac{\partial}{\partial k_\alpha} H_{\mathbf{k}}}{(\epsilon_{\mathbf{k},c}^0 - \epsilon_{\mathbf{k},v}^0)} | u_{\mathbf{k},v}^0 \rangle \\ &= \langle u_{\mathbf{k},c}^0 | i \frac{\partial}{\partial k_\alpha} u_{\mathbf{k},v}^0 \rangle. \end{aligned} \quad (2.33)$$

With the formalism developed in Section 2.1 we can express the scheme for the calculation of the dielectric tensors in terms of *pseudo* wave functions. The variational self-consistent functional of Eq. (2.25) now reads (the operator  $T_{\mathbf{k}}$  does not depend on the electric field):

$$\begin{aligned} \frac{\partial^2 E_{\text{tot}}}{\partial \mathcal{E}_\alpha^2} &= \frac{\Omega}{(2\pi)^3} \int_{BZ} \sum_v \left( \left\langle \frac{\partial}{\partial \mathcal{E}_\alpha} \tilde{u}_{\mathbf{k},v}^0 | T_{\mathbf{k}}^\dagger (H_{\mathbf{k}}^0 - \epsilon_{\mathbf{k},v}) T_{\mathbf{k}} | \frac{\partial}{\partial \mathcal{E}_\alpha} \tilde{u}_{\mathbf{k},v}^0 \right\rangle \right. \\ &\quad \left. + \left\langle \frac{\partial}{\partial \mathcal{E}_\alpha} \tilde{u}_{\mathbf{k},v}^0 | T_{\mathbf{k}}^\dagger i \frac{\partial}{\partial k_\alpha} T_{\mathbf{k}} | \tilde{u}_{\mathbf{k},v}^0 \right\rangle + \langle \tilde{u}_{\mathbf{k},v}^0 | T_{\mathbf{k}}^\dagger \left( i \frac{\partial}{\partial k_\alpha} \right)^\dagger T_{\mathbf{k}} | \frac{\partial}{\partial \mathcal{E}_\alpha} \tilde{u}_{\mathbf{k},v}^0 \rangle \right) d\mathbf{k} \\ &\quad + \frac{1}{2} \int \frac{n^1(\mathbf{r}) n^1(\mathbf{r}')}{|\mathbf{r} - \mathbf{r}'|} d\mathbf{r} d\mathbf{r}' + \int \frac{\delta V_{xc}}{\delta n} \Big|_{n^0} [n^1(\mathbf{r})]^2 d\mathbf{r}. \end{aligned} \quad (2.34)$$

This functional is minimized with respect to the first-order *pseudo* wave functions  $\frac{\partial}{\partial \mathcal{E}_\alpha} \tilde{u}_{\mathbf{k},i}^0$ , which must satisfy the constraints:

$$\left\langle \frac{\partial}{\partial \mathcal{E}_\alpha} \tilde{u}_{\mathbf{k},v}^0 | T_{\mathbf{k}}^\dagger T_{\mathbf{k}} | \tilde{u}_{\mathbf{k},v'}^0 \right\rangle + \text{c.c.} = 0. \quad (2.35)$$

This functional can be written in a more compact way by introducing *pseudo* operators:

$$\frac{\partial^2 E_{\text{tot}}}{\partial \mathcal{E}_\alpha^2} = \frac{\Omega}{(2\pi)^3} \int_{BZ} \sum_v \left( \left\langle \frac{\partial}{\partial \mathcal{E}_\alpha} \tilde{u}_{\mathbf{k},v}^0 | \tilde{H}_{\mathbf{k}}^0 - \epsilon_{\mathbf{k},v} S_{\mathbf{k}} | \frac{\partial}{\partial \mathcal{E}_\alpha} \tilde{u}_{\mathbf{k},v}^0 \right\rangle \right) \quad (2.36)$$



$$\begin{aligned}
& + \left\langle \frac{\partial}{\partial \mathcal{E}_\alpha} \tilde{u}_{\mathbf{k},v}^0 | T_{\mathbf{k}}^\dagger i \frac{\partial}{\partial k_\alpha} T_{\mathbf{k}} | \tilde{u}_{\mathbf{k},v}^0 \right\rangle + \left\langle \tilde{u}_{\mathbf{k},v}^0 | T_{\mathbf{k}}^\dagger \left( i \frac{\partial}{\partial k_\alpha} \right)^\dagger T_{\mathbf{k}} | \frac{\partial}{\partial \mathcal{E}_\alpha} \tilde{u}_{\mathbf{k},v}^0 \right\rangle d\mathbf{k} \\
& + \frac{1}{2} \int \frac{n^1(\mathbf{r})n^1(\mathbf{r}')}{|\mathbf{r}-\mathbf{r}'|} d\mathbf{r}d\mathbf{r}' + \int \frac{\delta V_{xc}}{\delta n} \Big|_{n^0} [n^1(\mathbf{r})]^2 d\mathbf{r}.
\end{aligned}$$

Similarly the constraints read:

$$\left\langle \frac{\partial}{\partial \mathcal{E}_\alpha} \tilde{u}_{\mathbf{k},v}^0 | S_{\mathbf{k}} | \tilde{u}_{\mathbf{k},v'}^0 \right\rangle + \text{c.c.} = 0. \quad (2.37)$$

The term  $T_{\mathbf{k}}^\dagger i \frac{\partial}{\partial k_\alpha} T_{\mathbf{k}}$  can be expanded by using Eq. (2.23):

$$\begin{aligned}
T_{\mathbf{k}}^\dagger i \frac{\partial}{\partial k_\alpha} T_{\mathbf{k}} &= i \frac{\partial}{\partial k_\alpha} + \sum_{i,j,\mathbf{R},\gamma} \left[ \right. \quad (2.38) \\
& \left. |\beta_{i,\mathbf{R},\gamma,\mathbf{k}} \rangle \left( \langle \Phi_{i,\mathbf{R},\gamma,\mathbf{k}} | i \frac{\partial}{\partial k_\alpha} | \Phi_{j,\mathbf{R},\gamma,\mathbf{k}} \rangle - \langle \tilde{\Phi}_{i,\mathbf{R},\gamma,\mathbf{k}} | i \frac{\partial}{\partial k_\alpha} | \tilde{\Phi}_{j,\mathbf{R},\gamma,\mathbf{k}} \rangle \right) \langle \beta_{j,\mathbf{R},\gamma,\mathbf{k}} | \right], \quad (2.39)
\end{aligned}$$

where  $i \frac{\partial}{\partial k_\alpha}$  acts also on  $\beta_{j,\mathbf{R},\gamma,\mathbf{k}}$ . By using Eqs. (2.20), we finally find:

$$\begin{aligned}
T_{\mathbf{k}}^\dagger i \frac{\partial}{\partial k_\alpha} T_{\mathbf{k}} &= i \frac{\partial}{\partial k_\alpha} + \sum_{i,j,\mathbf{R},\gamma} \left[ |\beta_{i,\mathbf{R},\gamma,\mathbf{k}} \rangle d_{\alpha,ij} \langle \beta_{j,\mathbf{R},\gamma,\mathbf{k}} | \right. \\
& \left. - |\beta_{i,\mathbf{R},\gamma,\mathbf{k}} \rangle Q_{i,j} \langle \beta_{j,\mathbf{R},\gamma,\mathbf{k}} | (\mathbf{r} - \mathbf{R}) | + |\beta_{i,\mathbf{R},\gamma,\mathbf{k}} \rangle Q_{i,j} \langle \beta_{j,\mathbf{R},\gamma,\mathbf{k}} | i \frac{\partial}{\partial k_\alpha} \right],
\end{aligned}$$

where we define:

$$\begin{aligned}
Q_{i,j} &= \langle \Phi_{i,\mathbf{R},\gamma,\mathbf{k}} | \Phi_{j,\mathbf{R},\gamma,\mathbf{k}} \rangle - \langle \tilde{\Phi}_{i,\mathbf{R},\gamma,\mathbf{k}} | \tilde{\Phi}_{j,\mathbf{R},\gamma,\mathbf{k}} \rangle \quad (2.40) \\
\mathbf{d}_{i,j} &= \langle \Phi_{i,\mathbf{R},\gamma,\mathbf{k}} | \mathbf{r} - \mathbf{R} | \Phi_{j,\mathbf{R},\gamma,\mathbf{k}} \rangle - \langle \tilde{\Phi}_{i,\mathbf{R},\gamma,\mathbf{k}} | \mathbf{r} - \mathbf{R} | \tilde{\Phi}_{j,\mathbf{R},\gamma,\mathbf{k}} \rangle.
\end{aligned}$$

The terms  $Q_{i,j}$  and  $\mathbf{d}_{i,j}$  do not depend on the particular cell labeled by  $\mathbf{R}$ . The first order *pseudo* wave functions  $\frac{\partial}{\partial k_\alpha} \tilde{u}_{\mathbf{k},v}^0$  are found by minimizing the following second order nonselfconsistent variational functional:

$$E^2[\tilde{u}_{\mathbf{k},v}^0, \frac{\partial}{\partial k_\alpha} \tilde{u}_{\mathbf{k},v}^0] = \left\langle \frac{\partial}{\partial k_\alpha} \tilde{u}_{\mathbf{k},v}^0 | \tilde{H}_{\mathbf{k}}^0 - \epsilon_{\mathbf{k}}^0 S_{\mathbf{k}} | \frac{\partial}{\partial k_\alpha} \tilde{u}_{\mathbf{k},v}^0 \right\rangle \quad (2.41)$$

$$\begin{aligned}
& + \left\langle \frac{\partial}{\partial k_\alpha} \tilde{u}_{\mathbf{k},v}^0 | \frac{\partial}{\partial k_\alpha} \tilde{H}_{\mathbf{k}}^0 - \epsilon_{\mathbf{k}}^0 \frac{\partial}{\partial k_\alpha} S_{\mathbf{k}} | \tilde{u}_{\mathbf{k},v}^0 \right\rangle \quad (2.42) \\
& + \left\langle \tilde{u}_{\mathbf{k},v}^0 | \frac{\partial}{\partial k_\alpha} \tilde{H}_{\mathbf{k}}^0 - \epsilon_{\mathbf{k}}^0 \frac{\partial}{\partial k_\alpha} S_{\mathbf{k}} | \frac{\partial}{\partial k_\alpha} \tilde{u}_{\mathbf{k},v}^0 \right\rangle,
\end{aligned}$$

where the first order wave functions must satisfy the constraints:

$$\left( \left\langle \frac{\partial}{\partial k_\alpha} \tilde{u}_{\mathbf{k},i}^0 \middle| \tilde{u}_{\mathbf{k},i}^0 \right\rangle + \text{c.c.} \right) + \left\langle \tilde{u}_{\mathbf{k},i}^0 \middle| \frac{\partial}{\partial k_\alpha} S_{\mathbf{k}} \middle| \epsilon_{\mathbf{k}}^0 \right\rangle = 0. \quad (2.43)$$

The operator  $\frac{\partial}{\partial k_\alpha} \tilde{H}_{\mathbf{k}}^0$  is calculated from:

$$\frac{\partial}{\partial k_\alpha} \tilde{H}_{\mathbf{k}} = i[\tilde{H}, r_\alpha]_{\mathbf{k}} \quad (2.44)$$

## 2.3 Implementation

The scheme, for the calculation of dielectric tensors of periodic solids with ultrasoft pseudopotentials, described in the previous section, has been implemented into a new software package based on the CPV Car-Parrinello code available in our group [20]. For addressing large models of disordered materials, the Brillouin zone is sampled at the sole  $\Gamma$ -point, and the wave functions are considered real. In this way, the required memory to store the wave functions is reduced by a factor of two. We developed two Fortran codes named CPVR and CPVE. The code CPVR calculates the derivatives of the unperturbed wave functions—previously calculated by the CPV code—with respect to the  $\mathbf{k}$  vector by minimizing the nonselfconsistent energy functional described in Eq. (2.41). Because of the  $\Gamma$ -point sampling, the first order wave functions can be taken purely imaginary. In Eq. (2.41), the required unperturbed wave functions are eigenstates of the unperturbed Hamiltonian. Therefore, before the minimization, a suitable unitary transformation is applied to the subspace of the unperturbed wave functions obtained from the CPV code. The first order wave functions are found by performing a damped Car-Parrinello dynamics for the electronic degrees of freedom. The constraint relations of Eq. (2.43) can be imposed in two different ways either via a set of Lagrange multipliers, which are updated at each time step, or by projecting the gradient of functional (2.41) with respect to the first order wave functions on the subspace spanned by the unoccupied states. The projector operator

which must be applied is (see Appendix B):

$$S_{\mathbf{k}} \sum_c |\tilde{u}_{\mathbf{k},c}^0\rangle \langle \tilde{u}_{\mathbf{k},c}^0| = 1 - S_{\mathbf{k}} \sum_v |\tilde{u}_{\mathbf{k},v}^0\rangle \langle \tilde{u}_{\mathbf{k},v}^0|. \quad (2.45)$$

The choice of the way in which the constraint relations are imposed has no influence on the results.

In the CPVE code, we implemented the minimization of the selfconsistent variational functional of Eq. (2.36). The first order derivatives of the wave function with respect to the  $\mathbf{k}$  vector and the unperturbed wave functions are given by the programs CPVR and CPV, respectively. Because of the  $\Gamma$ -point sampling, the first order wave functions with respect to the electric field can be taken real, as expected from the conservation of the time reversal symmetry in the presence of an electric field. As in the CPVR code, a Car-Parrinello dynamics is applied to minimize the second order energy. In this case the  $S$  operator does not depend on the perturbation, and, consequently, the constraints relations are simpler than in the code CPVR and are imposed by projecting the gradient of the functional (2.36) with respect to the first order wave functions on the subspace spanned by the unoccupied states. The applied projector operator is the same as the one defined in Eq. (2.45). In the CPVE code, the first order variation of the electronic charge is computed at each time step and the selfconsistent potential is updated. Finally, the complete dielectric tensor is computed with the nonvariational functional of Eq. (2.30).

## 2.4 Application to small molecules: H<sub>2</sub>O, CH<sub>4</sub>, and NH<sub>3</sub>

The validity of the scheme for obtaining dielectric tensors with ultrasoft pseudopotentials has been assessed by calculating the Raman intensities of three small molecules: the water, the methane, and the ammonia molecule. For these molecules, experimental and theoretical results are available in the literature. To calculate the Raman intensities, two ingredients are required: the derivatives of the polarizability tensor with respect to the atomic displacements, and the vibrational frequencies and modes. The polarizability tensors are defined as the second order derivative of the electronic energy with respect to

the electric field:

$$\alpha_{ij} = \frac{\partial^2 E}{\partial \mathcal{E}_i \partial \mathcal{E}_j}, \quad (2.46)$$

and are computed with the scheme exposed in the previous section. We use finite displacements to calculate the derivatives of  $\alpha_{ij}$  with respect to atomic displacements:

$$P_{ijak} = \frac{\partial \alpha_{ij}}{\partial R_{ak}}, \quad (2.47)$$

where the index  $a$  runs over the atoms of the molecule and the index  $k$  runs over the Cartesian directions. The vibrational modes and frequencies correspond to the eigenvectors and to the square roots of the eigenvalues of the dynamical matrix, respectively. The dynamical matrix is defined as:

$$D_{ai,bj} = \frac{1}{\sqrt{M_a M_b}} \frac{\partial^2 E}{\partial R_{ai} \partial R_{bj}}, \quad (2.48)$$

where  $M_a$  and  $M_b$  are the masses of atoms  $a$  and  $b$ , respectively. We calculate the dynamical matrix by taking finite differences of the atomic forces. The Raman tensors are defined as the derivative of the polarizability with respect to the vibrational modes and can be expressed as:

$$Q_{ij}^n = \sum_{ak} P_{ijak} \frac{v_{ak}^n}{\sqrt{M_a}}, \quad (2.49)$$

where  $v^n$  is the  $n$ -th normalized eigenmode. When no particular choice is made for the polarization of the observed outgoing photons, the Raman intensities are obtained by averaging on the spatial orientations [16]:

$$I^n = d^n (45\alpha_n'^2 + 7\gamma_n'^2), \quad (2.50)$$

where  $d^n$  is the degeneracy of the  $n$ -th mode and:

$$\begin{aligned} \alpha_n' &= \frac{1}{3} \sum_i Q_{ii}^n \\ \gamma_n'^2 &= \frac{1}{2} \left\{ (Q_{11}^n - Q_{22}^n)^2 + (Q_{11}^n - Q_{33}^n)^2 + (Q_{22}^n - Q_{33}^n)^2 \right. \\ &\quad \left. + 6[Q_{12}^{n2} + Q_{13}^{n2} + Q_{23}^{n2}] \right\}. \end{aligned} \quad (2.51)$$

The depolarization ratio  $\rho^n$ , giving the ratio between the intensity observed taking perpendicular and parallel the polarizations of incoming and outgoing photons, is expressed

as:

$$\rho^n = \frac{3\gamma_n'^2}{45\alpha_n'^2 + 4\gamma_n'^2}. \quad (2.52)$$

The depolarization ratio can vary from zero to 3/4, and vanishes for totally symmetric modes.

To study the water molecule we used ultrasoft pseudopotentials for both hydrogen and oxygen atoms. The valence wave functions and the electron density are described by plane-wave basis sets defined by cutoff energies of 40 and 160 Ry, respectively. The exchange and correlation energy is given within the local density approximation. We considered an O-H bond of length 1.85 bohr and a H-O-H angle of 105.9°, corresponding to the relaxed structure for a cell of size  $L = 20$  bohr. We calculated the Raman tensors and the dynamical matrix by taking finite differences of the polarizability and of the atomic forces, respectively. We chose atomic displacements of  $\pm 0.05$  bohr, and a cubic cell with a side of 25 bohr. For these displacements, the polarizabilities and the forces are in the linear regime. In Tab. 2.1, we report the vibrational frequencies and the corresponding Raman intensities and depolarization ratios. The agreement with the experimental results [34] is very good. The experimental frequencies are taken from Ref. [38]. To compare our results with other calculations, we also report the results of Refs. [35] and [36] which were obtained by a all-electron LDA methodology with localized basis sets.

For the methane molecule we used the same hydrogen pseudopotential adopted for the water molecule, and an ultrasoft pseudopotential for the carbon atom. We applied a cutoff of 40 Ry for the wave functions and of 160 Ry for the electronic charge density. The C-H bond length was determined by relaxing the structure in a cubic cell with a side of 25 bohr. We found a C-H bond length of 2.1 bohr. To calculate the Raman tensors and the dynamical matrix, we chose atomic displacements of  $\pm 0.5$  bohr. In Tab. 2.2, we report the vibrational frequencies and the corresponding Raman intensities and depolarization ratios. As for the water molecule, the agreement with the experimental results of Ref. [37] is very good. The experimental frequencies are taken from Ref. [38]. To compare our results with other calculations, we also report the results of Refs. [35] and [36].

For the ammonia molecule, we used an ultrasoft pseudopotential for the nitrogen atom

Table 2.1: Raman intensities (RAM), frequencies ( $\omega$ ) and depolarization ratio ( $\rho$ ) of the water molecule. The Raman intensity is given in  $\text{\AA}^4 \cdot \text{amu}^{-1}$ , the frequency is given in  $\text{cm}^{-1}$ . The results of Refs. [35] and [36] are from all-electron LDA calculations. The experimental values are taken from Ref. [34].

Present			Expt. [34]			Ref. [35]		Ref. [36]	
$\omega$	RAM	$\rho$	$\omega$	RAM	$\rho$	$\omega$	RAM	RAM	$\rho$
1502	0.71	0.61	1595	$0.9 \pm 2$	0.74	1547	0.67	1.0	0.59
3725	119	0.05	3657	$108 \pm 14$	0.03	3714	110	111	0.04
3848	25.6	0.75	3756	$19.2 \pm 2.1$	0.75	3823	24.9	25	0.75

Table 2.2: Raman intensities (RAM), frequencies ( $\omega$ ) and depolarization ratio ( $\rho$ ) of the methane molecule. The Raman intensity is given in  $\text{\AA}^4 \cdot \text{amu}^{-1}$ , the frequency is given in  $\text{cm}^{-1}$ . The results of Refs. [35] and [36] are from all-electron LDA calculations. The experimental values are taken from Ref. [37].

Present			Expt. [37]			Ref. [35]		Ref. [36]	
$\omega$	RAM	$\rho$	$\omega$	RAM	$\rho$	$\omega$	RAM	RAM	$\rho$
1226	0.11	0.75	1306	$\leq 0.24$	0.75	1250	0.27	0.01	0.75
1469	2.6	0.75	1534	$7.0 \pm 0.4$	0.75	1480	4.40	7.4	0.75
2940	254	0	2917	$230 \pm 12$	0	2957	247	252	0
3053	144	0.75	3019	$128 \pm 7$	0.75	3085	141	149	0.75

Table 2.3: Raman intensities (RAM), frequencies ( $\omega$ ) and depolarization ratio ( $\rho$ ) of the ammonia molecule. The Raman intensity is given in  $\text{\AA}^4 \cdot \text{amu}^{-1}$ , the frequency is given in  $\text{cm}^{-1}$ . The results of Ref. [36] are from all-electron LDA calculations. The experimental values are taken from Ref. [39].

Present			Expt. [39]		Ref. [36]	
$\omega$	RAM	$\rho$	$\omega$	RAM	RAM	$\rho$
959	3.4	0.26	950		1.4	0.23
1571	1.48	0.75	1627		4.5	0.75
3395	191.4	0.01	3337	182 $\pm$ 2	208	0.01
3504	80.7	0.75	3444		104	0.75

and adopted the same cutoffs, cell parameters, and atomic displacements used for studying the methane molecule. After relaxation, the N-H bond length was 1.95 bohr, and the H-N-H angle was  $105.5^\circ$ . These structural parameters compare well with the corresponding experimental ones [38]: 1.91 bohr and  $106.7^\circ$ , respectively. In Tab. (2.3), we report the vibrational frequencies and the corresponding Raman intensities and depolarization ratios. The experimental Raman intensities and depolarization ratios are from Ref. [39]. The experimental frequencies are taken from Ref. [38]. To compare our results with other calculations, we also report the results of Ref. [35].

The comparison of the calculated Raman intensities and polarization ratios with both experimental and previous theoretical results is excellent. This validates our scheme for the calculation of Raman spectra with the use of ultrasoft pseudopotentials.





## Chapter 3

# Finite electric fields

### 3.1 Introduction

Density functional calculations applied to periodic solids have demonstrated their reliability in describing material properties and have become a routinely used tool for investigation. However, the application of these methods to systems in an external electric field have remained limited, in sharp contrast with the widespread use of electric fields in experimental setups. Several theoretical studies have shown that it is possible to account for the effect of an electric field within a perturbational approach [40, 19, 41, 33, 42]. However, the study of dynamical transformations in an electric field would greatly benefit from the possibility of considering *finite* fields. In fact, the energy of the electronic ground state in an extended electric field does not have a lower bound [43, 44, 45]. Nonetheless, it is of interest to describe the long-living metastable physical state which arises in response to the field [44, 45].

The difficulty of treating finite electric fields is related to the intrinsic nonperiodic nature of the position operator. The advent of the modern theory of polarization [46, 47] has revitalized the study of electric fields in periodic electronic structure calculations [45, 48, 49]. In particular, Nunes and Gonze [49] introduced a periodic energy functional depending on the applied electric field and recovered the same derivatives with respect to the field as given by more conventional perturbational methods [19, 33].

Here, we introduce an energy functional to treat *finite* electric fields in first-principles electronic structure calculations. We prove that its derivatives with respect to the field coincide with those of perturbational approaches [19, 33, 42, 49] for any order of perturbation. The present functional provides a practical way for investigating dielectric properties. Furthermore, by calculating derivatives with respect to atomic positions, we show that this functional is suitable for application in *ab initio* molecular dynamics schemes [18]. Using bulk MgO as a test case, we calculate by finite differences the high-frequency dielectric constant and the Born effective charges, and find excellent accord with results obtained with perturbational methods. We also show how the static dielectric constant can be obtained by performing a molecular dynamics relaxation, entirely avoiding the calculation of normal modes. To illustrate the potential of our scheme for systems of large size, we calculate the high- and low-frequency dielectric constants for a model of vitreous silica, finding good agreement with experiment. Finally, we discuss the convergence of the dielectric constant with respect to the size of the periodic supercell.

## 3.2 The method

For a system obeying periodic boundary conditions, we describe its metastable state induced by the presence of a finite electric field  $\mathcal{E}$  (taken along  $x$ ) by the variational energy functional:

$$E^{\mathcal{E}}[\{\psi_i\}] = E^{(0)}[\{\psi_i\}] - \Omega \mathcal{E} \cdot P[\{\psi_i\}], \quad (3.1)$$

where  $\Omega$  is the volume of the unit cell,  $E^{(0)}[\{\psi_i\}]$  is the usual energy functional in the absence of an electric field and  $P[\{\psi_i\}]$  the polarization along the direction of  $\mathcal{E}$ , as defined by Resta [50]:

$$P[\{\psi_i\}] = -\frac{1}{\Omega} \frac{L}{\pi} \text{Im} \left( \ln \det S[\{\psi_i\}] \right), \quad (3.2)$$

where  $L$  is the periodicity of the cell and  $S[\{\psi_i\}]$  a matrix calculated for the set of doubly occupied wave functions  $\{\psi_i\}$ <sup>1</sup>:

$$S_{ij} = \langle \psi_i | e^{2\pi i x/L} | \psi_j \rangle. \quad (3.3)$$

For simplicity, we here consider cubic unit cells. The same functional as in (3.1) was studied in Ref. [42] within a perturbational approach.

In Ref. [49], Nunes and Gonze investigate the perturbative development of functional (3.1). In particular, they formulate, starting from the thermodynamic limit of functional (3.1) for a crystalline system (i.e. a dense sampling of the Brillouin zone), two series of variational functionals for the derivatives of the energy with respect to the electric field, both holding for a discrete sampling of the Brillouin zone. The first series of functionals is found by first applying the perturbative expansion directly in the thermodynamic limit, and by subsequently discretizing the Brillouin zone integration. This approach corresponds to conventional perturbational methods [19, 33]. To obtain the second series of functionals, the discretization is applied before the perturbative expansion. Both approaches were obtained by considering at any order the conservation of the Bloch symmetry for the wave functions. The two approaches converge in the thermodynamic limit. The second approach was first used in Ref. [42] for the second order derivative of the energy with respect to the electric field, in the case of a  $\Gamma$ -point sampling of the Brillouin zone.

For a crystalline material, it is of interest to compare our formulation, which adopts a supercell and a sampling of the Brillouin zone at the sole  $\Gamma$ -point, to those of Ref. [49], which adopts a primitive cell and a sampling of the Brillouin zone with a discrete number of  $\mathbf{k}$ -points. We first consider the case of a vanishing electric field. Applied to a crystalline system with periodicity  $a$  in the direction of the field, with  $L = N \cdot a$ , the definition (3.2) of the polarization coincides with that of Nunes and Gonze provided a discrete number  $N$  of equally spaced  $k$ -points are used [50]. However, when the field is turned on, the states  $\{\psi_i\}$  minimizing the functional (3.1) are allowed to vary in a Hilbert space which does not necessarily impose the Bloch symmetry. This enhanced variational freedom constitutes, in

---

<sup>1</sup>conforming to standard notations we use the symbol  $S$ , which should not be confused with the pseudo identity operator identified in Chapter 2 with the same symbol.

principle, a *qualitative* difference with respect to approaches in which the perturbation is assumed to preserve from the outset the periodicity  $a$  of the minimal unit cell [19, 33, 49].

The physical observables correspond to the thermodynamic limit  $N \rightarrow \infty$  of the derivatives of the energy (3.1) at vanishing field:

$$E^{(n)} = \frac{1}{n!} \lim_{N \rightarrow \infty} \frac{1}{N} \left. \frac{d^n E_N^\mathcal{E}}{d\mathcal{E}^n} \right|_{\mathcal{E}=0}. \quad (3.4)$$

We show, for any  $N$ , that the optimized wave functions preserve the Bloch symmetry and that our results for  $(1/N)d^n E_N^\mathcal{E}/d\mathcal{E}^n$  coincide with those obtained by Nunes and Gonze in their second approach, in which the Bloch symmetry of the states was assumed *a priori*. As shown by Nunes and Gonze, these results coincide, at the thermodynamic limit, with those obtained by *periodic* conventional perturbational methods [19, 33]. This indicates that the result obtained with a periodic scheme is recovered identically *even when the periodic symmetry is relaxed*.

For the lowest orders,  $E^{(0)}$  and  $E^{(1)}$  depend only on the unperturbed eigenstates  $\{\psi_i^{(0)}\}$ , which obey the Bloch symmetry. The equivalence with perturbational methods can then be demonstrated as in Ref. [50]. We extend the correspondence to the second and third order of the energy by considering an expansion of the perturbed wave functions  $\psi_i^\mathcal{E}$  up to first order in  $\mathcal{E}$  [51]. For a crystalline system with  $L = N \cdot a$ :

$$|\psi_i^\mathcal{E}\rangle = e^{ik_i x} |u_i^{(0)}\rangle + \mathcal{E} \sum_{k'} e^{ik' x} |u_{k_i \rightarrow k'}^{(1)}\rangle + O(\mathcal{E}^2), \quad (3.5)$$

where the functions  $u_i^{(0)}$  and  $u_{k \rightarrow k'}^{(1)}$  are periodic with periodicity  $a$ , and the sum runs over  $k' = 2\pi n/L$  with  $n = 0, \dots, N-1$ . The expansion in (3.5) explicitly allows for mixing between different  $k$ -points. At second order, the perturbation term in (3.1) gives:

$$2\Omega \left. \frac{dP}{d\mathcal{E}} \right|_{\mathcal{E}=0} = -\frac{2L}{\pi} \text{Im} \frac{1}{D^{(0)}} \left. \frac{d}{d\mathcal{E}} \det S[\{\psi_i^\mathcal{E}\}] \right|_{\mathcal{E}=0}, \quad (3.6)$$

where  $D^{(0)} = \det S[\{\psi_i^{(0)}\}]$ . When replacing (3.5) in (3.6), only terms diagonal in  $k$  survive, i.e.

$$|u_{k_i \rightarrow k'}^{(1)}\rangle = \delta_{k_i k'} |u_{k_i \rightarrow k_i}^{(1)}\rangle, \quad (3.7)$$

owing to the property that the operator  $e^{2\pi ix/L}$  in  $S$  only couples wave functions of symmetry  $k_i$  and  $k_i + 2\pi/L$ . The proof is then extended at any order of perturbation by induction.

We treat finite electric fields by implementing the functional (3.1) within the widespread scheme based on plane-wave basis sets and pseudopotentials. We consider the following extended Car-Parrinello Lagrangian, which allows us to study the simultaneous evolution of the ionic and electronic degrees of freedom in the presence of an electric field:

$$\mathcal{L} = \mu \sum_i \int d\mathbf{r} \left| \frac{d\psi_i(\mathbf{r})}{dt} \right|^2 + \frac{1}{2} \sum_I M_I \left( \frac{d\mathbf{R}_I}{dt} \right)^2 - E^{\mathcal{E}}[\{\psi_i\}] + \mathcal{E} \cdot P_{\text{ion}}, \quad (3.8)$$

where  $\mu$  is the fictitious electron mass,  $\mathbf{R}_I$  and  $M_I$  are the position and the mass of the  $I$ th ion, respectively, and  $P_{\text{ion}}$  is the ionic polarization defined as:

$$P_{\text{ion}} = \sum_{I=1}^{N_{\text{ion}}} Z_I \cdot X_I, \quad (3.9)$$

where  $X_I$  and  $Z_I$  are the position coordinate of the  $I$ th ion in the direction of the applied field and its core charge, respectively. Consistently with the definition of the polarization (3.2), the wave functions  $\psi_i$  are taken at the  $\Gamma$  point of the Brillouin zone. The Lagrangian (3.8) is subjected to the orthonormality constraints for the wave functions:

$$\langle \psi_i | \psi_j \rangle = \delta_{ij}. \quad (3.10)$$

The Euler equations of motion describing the evolution of the electronic and ionic degrees of freedom become:

$$\mu \frac{d^2 \psi_i}{dt^2} = - \frac{\delta E^{(0)}}{\delta \psi_i^*} + \mathcal{E} \cdot \frac{L}{\pi} \text{Im} \sum_j (S^{-1})_{ij} \psi_j + \sum_j \Lambda_{ij} \psi_j \quad (3.11)$$

$$M_I \frac{d^2 \mathbf{R}_I}{dt^2} = - \frac{\partial E^{(0)}}{\partial \mathbf{R}_I} + \mathcal{E} Z_I \hat{x}, \quad (3.12)$$

where  $\hat{x}$  is a unitary vector along the direction of the electric field, and  $\Lambda_{ij}$  are Lagrange multipliers used to ensure the orthonormality constraints (3.10). To derive the Euler equations (3.11), we used the relation:

$$d(\ln \det S) = \sum_{ij} (S^{-1})_{ij} dS_{ji}. \quad (3.13)$$

The computational overhead of our implementation with respect to a conventional Car-Parrinello scheme is limited to the inversion of the matrix  $S$  (3.3).

The pathological behavior of functional (3.1), which arises in the limit of a dense  $k$ -point sampling in the work of Ref. [49], corresponds in our formulation to the limit of infinite cell size  $L$ . For a given cell size  $L$ , our formulation therefore guarantees the occurrence of a well defined minimum. Once the Riemann plane defining the logarithmic function in (3.2) is chosen, this minimum is uniquely defined. We note that, for a fixed cell size  $L$ , an instability develops when the electric field exceeds a given critical value  $\mathcal{E}_c$ . This occurs when the difference in electric potential across the cell size  $L$  is of the order of the electronic gap.

In our formulation, we take advantage of the time-reversal symmetry to use *real* wave functions as in a conventional Car-Parrinello scheme. Indeed, it can be shown that, taking real wave functions as a starting point, the evolution as defined by the Euler equation (3.11) preserves the real character of the wave functions. The formulation presented here applies to norm-conserving pseudopotentials but can readily be extended to the case of ultrasoft ones [20] (see Sec. 3.5).

In parallel to our work, a method based on similar concepts was proposed independently by Souza, Íñiguez, and Vanderbilt [52]. By reasoning in terms of the density matrix of an *extended* system, these authors proved that a perturbation based on the *true* position operator  $\vec{r}$  preserves the Bloch symmetry. Therefore, they only considered only wave functions with Bloch symmetry in their approach.

### 3.3 Application to bulk MgO

To examine the reliability of this approach, we focused on the dielectric properties of bulk MgO. We modeled MgO by a periodic cubic cell containing 64 atoms at the experimental lattice constant. Only valence wave functions were treated explicitly, while core-valence interactions were described by ultrasoft pseudopotentials [31]. The exchange and correlation energy was described by the local density approximation.

First, we investigated the stability of the energy functional (3.1) as a function of the

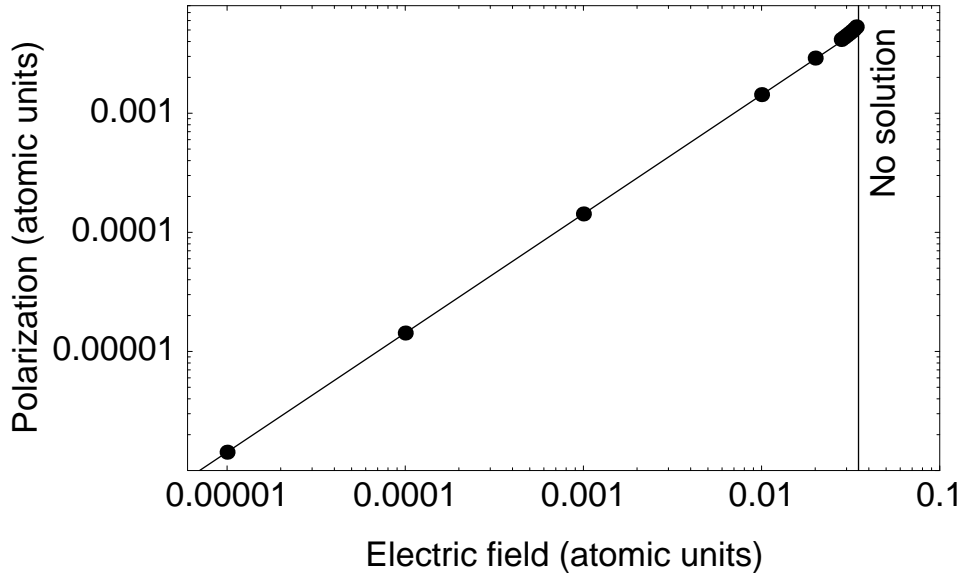


Figure 3.1: Calculated polarization per unit volume versus electric field for bulk MgO (discs). The solid line corresponds to the result from linear response [42] (see Sec. 3.5). The polarization is given as a difference with respect to the case of vanishing field. For electric fields higher than  $\sim 0.035$  a.u. the functional (3.1) could not be minimized.

Table 3.1: Dielectric properties of bulk MgO. We used an electric field  $\mathcal{E}$  of  $10^{-3}$  a.u.. The reference values were calculated without finite fields (see text).

	Finite $\mathcal{E}$	Reference	Experiment
$Z^*$	1.96	1.96	1.98
$\epsilon_\infty$	2.79	2.79	2.96
$\Delta\epsilon_0$	5.14	5.09	6.67

applied electric field for *fixed* atomic positions. A variational minimum was found for field intensities ranging over several orders of magnitude up to 0.034 atomic units, corresponding to 1.7 V/Å. Beyond this value of the field, the functional could not be minimized. The instability occurs for fields of the same order as the critical field  $E_{\text{gap}}/L = 0.5$  V/Å, where  $L$  is the periodicity of our simulation cell. In Fig. (3.1), the variation of the polarization  $\Delta P^\mathcal{E} = P^\mathcal{E} - P^0$  shows a close to linear behavior for fields  $\mathcal{E}$  in the range of stability of the energy functional. Within the linear regime, the high-frequency dielectric constant can be estimated from

$$\epsilon_\infty = 4\pi \frac{\Delta P^\mathcal{E}}{\mathcal{E}} + 1, \quad (3.14)$$

valid for cubic crystals. For a field of  $10^{-3}$  a.u., we found  $\epsilon_\infty = 2.79$ . To check the validity of this result, we used the linear response approach of Ref. [42] generalized to treat ultrasoft pseudopotentials ( see Sec. 3.5), and found a numerically equivalent result (within  $10^{-4}$ ). This application illustrates that functional (3.1) also provides reliable results for *finite*  $\mathcal{E}$ .

The Born effective charges  $Z^*$  are defined as the derivatives of the atomic forces with respect to the electric field [47]. The  $Z^*$  can then be obtained in a straightforward way by using the atomic force  $F^\mathcal{E}$  acting on the ions in the presence of a field  $\mathcal{E}$ :

$$Z^* = \frac{F^\mathcal{E}}{\mathcal{E}}, \quad (3.15)$$

where we used  $F^{\mathcal{E}=0} = 0$  and the cubic symmetry of the crystal. For a field  $\mathcal{E} = 10^{-3}$  a.u., we obtained  $Z^* = 1.96$ . The charges  $Z^*$  can alternatively be defined as derivatives of the polarization with respect to atomic displacements at vanishing electric field [47]. Using a



Table 3.2: High-frequency dielectric constant  $\epsilon_\infty$  and the difference  $\Delta\epsilon$  between low- and high-frequency dielectric constants for a model of vitreous silica [21]. The reference values for  $\epsilon_\infty$  and  $\Delta\epsilon$  are obtained by linear response [42] (see Sec. 3.5) and taken from Ref. [23], respectively. A field  $\mathcal{E}$  of  $10^{-2}$  a.u. was applied along each of the Cartesian directions (see text).

	$\epsilon_\infty$		$\Delta\epsilon$			
	Finite $\mathcal{E}$	Ref.	Expt.	Finite $\mathcal{E}$	Ref.	Expt.
$x$	1.99	1.99		1.43	1.46	
$y$	2.01	2.01		1.70	1.67	
$z$	2.01	2.01		1.56	1.55	
average	2.00	2.00	2.1	1.56	1.56	1.8

finite difference approach in which the Mg and O sublattices are relatively displaced by 0.2 bohr, we derived a value of  $Z^* = 1.96$ , numerically coincident with the value obtained with the finite field method.

To check the validity of the method for describing *atomic relaxations* in a finite electric field, we investigated the static dielectric constant. The difference between the low- and high-frequency dielectric constants is generally expressed in terms of the Born effective charges, the vibrational frequencies, and their associated eigenmodes [24]. For bulk MgO:

$$\Delta\epsilon = \epsilon_0 - \epsilon_\infty = \frac{4\pi}{\Omega_0} \frac{(Z^*)^2}{\mu\omega^2}, \quad (3.16)$$

where  $\omega$  is the frequency of the zone-center optical phonon,  $\mu$  the reduced mass of Mg and O atoms, and  $\Omega_0$  the volume of the fcc primitive cell. We obtained the zone-center frequency  $\omega$  by a frozen phonon calculation. Direct application of (3.16) then gives  $\Delta\epsilon = 5.09$ .

The functional (3.1) offers an alternative procedure for obtaining static dielectric constants, which entirely avoids the calculation of normal modes. We performed a damped molecular dynamics relaxation, in which the atomic positions are allowed to relax fully in the presence of a finite electric field  $\mathcal{E}$ . In this case,  $\Delta\epsilon$  can be expressed in terms of a

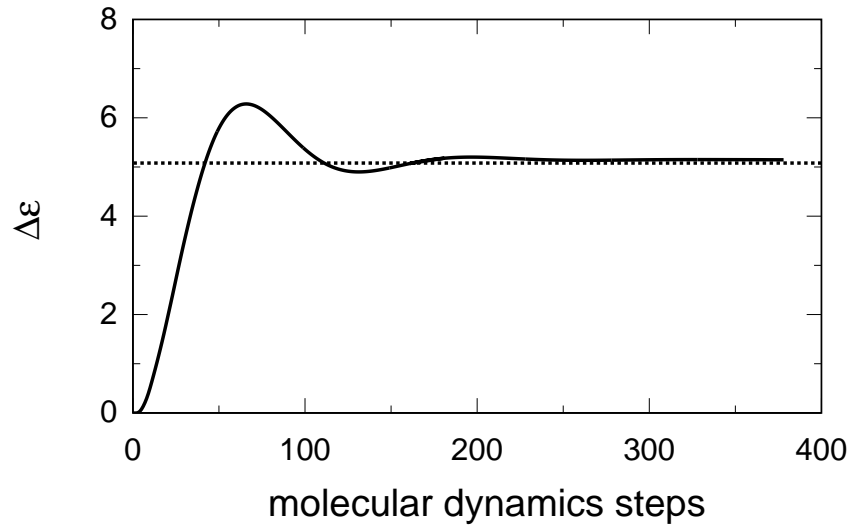


Figure 3.2: Evolution of  $\Delta\epsilon$  for a model of MgO during a damped molecular dynamics relaxation in a finite electric field of  $10^{-3}$  a.u. The dotted line corresponds to the result from linear response (3.16).

difference between polarizations associated with atomic configurations before ( $P_{\text{nonrelaxed}}^{\mathcal{E}}$ ) and after ( $P_{\text{relaxed}}^{\mathcal{E}}$ ) atomic relaxation:

$$\Delta\epsilon = 4\pi \frac{P_{\text{relaxed}}^{\mathcal{E}} - P_{\text{nonrelaxed}}^{\mathcal{E}}}{\mathcal{E}}, \quad (3.17)$$

where both polarizations,  $P_{\text{nonrelaxed}}^{\mathcal{E}}$  and  $P_{\text{relaxed}}^{\mathcal{E}}$ , are calculated in the presence of a field  $\mathcal{E}$ . In Fig. (3.2), we plot the evolution of  $\Delta\epsilon$  during the relaxation of the atomic positions in an electric field of  $10^{-3}$  a.u. After a few oscillations,  $\Delta\epsilon$  converges rapidly to 5.14, differing by less than the numerical accuracy from the estimate of 5.09, derived from (3.16). The dielectric properties obtained for MgO are summarized in Table (3.1), where the experimental results [57] have been included for comparison.

To illustrate the potential of functional (3.1) for treating complex systems of large size, we considered the dielectric properties of a model structure of vitreous silica [21], for which the Born effective charges [23] and the vibrational properties [22] were obtained previously. Through an electronic relaxation in a field of  $10^{-2}$  a.u., we obtained via (3.14) a high-frequency dielectric constant of 2.00, in good agreement with the experimental value for vitreous silica ( $\epsilon_{\infty}^{\text{expt}} = 2.1$  [53]). Applying the linear response method of Ref. [42] generalized to treat ultrasoft pseudopotentials (see Sec. 3.5), we yielded the same value for  $\epsilon_{\infty}$ , thereby confirming this result (Table 3.2).

The advantage of using the functional (3.1) is impressive for the calculation of the Born effective charges and of the difference  $\Delta\epsilon$  between low- and high-frequency dielectric constants. All the Born effective charges could be obtained via (3.15) using just three electronic relaxations. This should be contrasted with the method in Ref. [23], which required three electronic relaxations for each atom in the model.<sup>2</sup> The Born effective charges calculated with the two methods are identical within numerical accuracy. Using the molecular dynamics relaxation scheme, we obtained  $\Delta\epsilon$  via (3.17). We found a value of 1.6, in accord with the result in Ref. [23]. We note that the structural relaxations, required by the finite field method, imply a substantially smaller computational effort than the calculation of the full dynamical matrix [23, 22]. The theoretical value for  $\Delta\epsilon$  (1.6) compares well with the experimental one (1.8).

---

<sup>2</sup>For the calculation of  $Z^*$ , the present scheme is computationally as efficient as perturbational methods.

### 3.4 Convergence of the dielectric constant with cell size

When a supercell of size  $L$  is used to describe a system, the dielectric properties and, in particular, the dielectric constant can be calculated by two different expressions which coincide in the limit of large  $L$ , as discussed in Sec. 3.2. The first expression for the dielectric constant is given by a conventional perturbational (CP) approach [19, 33]. The second expression is obtained by the finite field approach [25, 42]. We study the convergence of the dielectric constant given by these two expressions with supercell size  $L$ , using a  $\Gamma$ -point sampling of the electronic structure, as done in the previous section.

We first focus on the polarizability of an isolated system. For sufficiently large supercells for which the wave functions can be considered localized, the CP polarizability has converged, whereas the finite-field polarizability still converges like  $1/L^2$  to the asymptotic value. Similarly, for an extended crystalline system, we demonstrate that the difference between the CP and finite-field dielectric constants converges like  $1/L^2$ . We illustrate this behavior for the cases of the isolated water molecule and bulk silicon.

We address the polarizability of an isolated system as obtained in a periodic supercell approach. To simplify the notation, we consider a one-dimensional system of one electron in a cell of size  $L$ , described by a Hamiltonian  $H^0$ . For cell sizes larger than  $L_f$ , we assume that the electronic ground state has converged to  $\Psi^0$ , for which  $H^0\Psi^0 = E^0\Psi^0$ . Hence, for  $L > L_f$ , the electronic wave function is localized. The dielectric polarizability can then be derived by minimizing the following variational functional with respect to the first-order wave function  $\Psi^1$  (using atomic units):

$$\alpha[\Psi^1] = -2 \left( \begin{aligned} &\langle \Psi^1 | H^0 - E^0 | \Psi^1 \rangle \\ &- \langle \Psi^1 | x | \Psi^0 \rangle - \langle \Psi^0 | x | \Psi^1 \rangle \end{aligned} \right), \quad (3.18)$$

with the constraint:

$$\langle \Psi^0 | \Psi^1 \rangle + \langle \Psi^1 | \Psi^0 \rangle = 0. \quad (3.19)$$

For  $L > L_f$ , the position operator  $x$  in (3.18) is well defined because of the localization of  $\Psi^0$ . Furthermore, in this regime, the polarizability (3.18) corresponds identically to the

expression derived in CP schemes [19, 33]. Hence, for increasing  $L$ , the CP polarizability converges as soon as  $\Psi^0$  and  $\Psi^1$  have converged.

In the perturbational scheme obtained from the functional (3.1) the polarizability is obtained by minimizing the variational functional [42]:

$$\alpha[\Psi^1] = -2 \left( \langle \Psi^1 | H^0 - E^0 | \Psi^1 \rangle - \frac{1}{G} \text{Im} \frac{\langle \Psi^1 | e^{iGx} | \Psi^0 \rangle + \langle \Psi^0 | e^{iGx} | \Psi^1 \rangle}{\langle \Psi^0 | e^{iGx} | \Psi^0 \rangle} \right), \quad (3.20)$$

where  $G = 2\pi/L$ , with the same constraint (3.19). The functional (3.20) is equivalent to the second-order derivative with respect to the electric field of the energy functional (3.1). The argument of the Im function on the right hand side of Eq. (3.20) can be expanded in terms of  $G$ . The zeroth- and second-order terms of this argument are real and do not contribute to functional (3.20). The first contributing term in this argument is the first-order one, and corresponds to the interaction term in functional (3.18). The higher order terms can thus be seen as a perturbation to functional (3.18). The first nonvanishing term in this perturbation series is of order  $G^2$ . Therefore, for  $L > L_f$ , the polarizability calculated within the finite-field scheme converges as  $1/L^2$  to the one calculated in the CP scheme.

We calculated the polarizability of the water molecule using the CP and the finite-field schemes for cubic cells of varying size. For the CP scheme we used the codes described in Chapter 2. In the finite-field scheme, we used a finite electric field intensity of  $1 \cdot 10^{-3}$  a.u. We checked that for this field intensity the same result is achieved as in the corresponding perturbational scheme. We used ultrasoft pseudopotentials for both hydrogen and oxygen atoms [20]. The valence wave functions and the electron density are described by plane-wave basis sets defined by cutoff energies of 20 and 150 Ry, respectively. The exchange and correlation energy is given within the local density approximation. When the cell size was varied, the internal molecular coordinates were kept fixed. We took a OH bond of length 1.85 bohr and a H-O-H angle of  $105.9^\circ$ , corresponding to the relaxed structure for a cell of size  $L = 20$  bohr. In Fig. 3.3, we report the calculated polarizabilities of the water

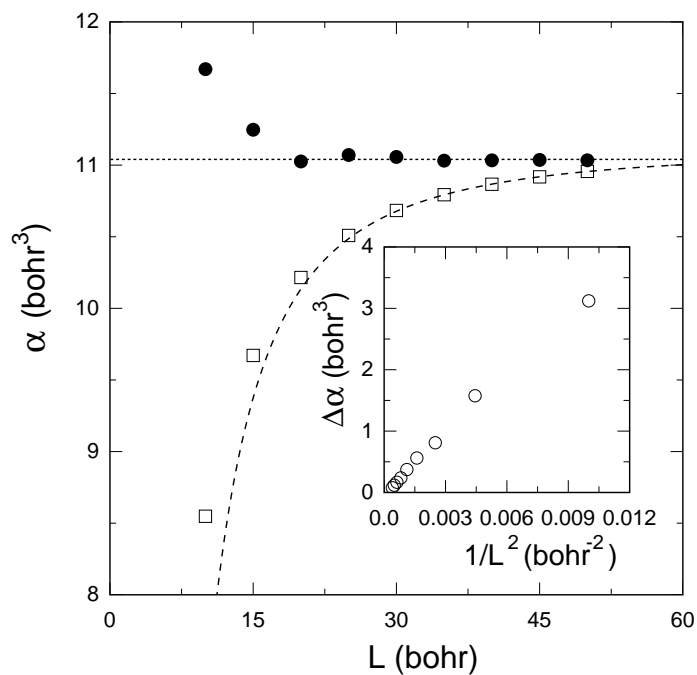


Figure 3.3: Polarizability of the  $\text{H}_2\text{O}$  molecule versus the size  $L$  of the adopted cubic cell, in the conventional perturbational (disc) and the finite-field (square) schemes, for a  $\Gamma$ -point sampling. The polarizability is calculated along the bisector of the H-O-H angle. The lines are guides to the eyes. Inset: Difference between the polarizabilities obtained with the two schemes, plotted versus  $1/L^2$ .

molecule, along the direction bisecting the H-O-H angle. For cells larger than  $\sim 30$  bohr, the polarizability calculated within the CP scheme is converged. We found a value of 11.0 bohr<sup>3</sup>, in good agreement with other similar calculations (10.8 bohr<sup>3</sup>) [54] and with the experimental value (9.6 bohr<sup>3</sup>) [55]. The polarizability calculated in the finite-field scheme shows a slower convergence. The inset in Fig. 3.3 shows that the difference between the two polarizabilities converges like  $1/L^2$ , in accord with the above derivation.

We now address the case of an extended crystalline system. We focus on a one-dimensional periodic system with a single electron per primitive cell, and limit the discussion to a nonselfconsistent Hamiltonian. We consider a supercell of size  $L$  containing  $N$  primitive cells of length  $a$ :  $L = N \cdot a$ . Treating this supercell at the  $\Gamma$  point is equivalent to sampling the Brillouin zone of the primitive cell with  $N$  equally spaced  $k$ -points:

$$k_i = \frac{2\pi}{Na}i, \quad \text{with } i = 0, \dots, N-1. \quad (3.21)$$

This equivalence is trivially verified for the CP scheme and has been demonstrated rigorously for the finite-field methods in Section 3.2. To address the convergence properties of the dielectric constant, we here adopt the multiple  $k$ -point formulation. The high-frequency dielectric constant for a crystalline system is related to the second-order derivative of the energy with respect to the electric field:

$$\epsilon_\infty = 1 - \frac{4\pi}{a} \frac{d^2 E}{d\mathcal{E}^2}, \quad (3.22)$$

where  $E$  is the energy per primitive cell and  $\mathcal{E}$  the intensity of the electric field.

In the CP scheme, the derivative  $d^2 E/d\mathcal{E}^2$  is found by minimizing the following variational functional with respect to the first-order wave functions  $u_{k_i}^1$  of periodicity  $a$  [24]:

$$\begin{aligned} \frac{d^2 E}{d\mathcal{E}^2} = \frac{2}{N} \sum_{i=0}^{N-1} \left( \langle u_{k_i}^1 | H_{k_i, k_i}^0 - E_{k_i}^0 | u_{k_i}^1 \rangle \right. \\ \left. + \langle u_{k_i}^1 | i \frac{du_{k_i}^0}{dk} \rangle + \langle i \frac{du_{k_i}^0}{dk} | u_{k_i}^1 \rangle \right), \end{aligned} \quad (3.23)$$

with the constraints:

$$\langle u_{k_i}^0 | u_{k_i}^1 \rangle + \langle u_{k_i}^1 | u_{k_i}^0 \rangle = 0. \quad (3.24)$$

We here use the same notation as in Ref. [24]. In the nonselfconsistent expression (3.23), the contribution of each  $k$ -point independently contributes to the average.

In the finite-field scheme, the interaction per primitive cell is given by the term:

$$\mathcal{E} \frac{a}{2\pi} \text{Im} \ln \det S, \quad (3.25)$$

where

$$\det S = \prod_{i=0}^{N-1} \langle u_{k_i} | u_{k_{i+1}} \rangle. \quad (3.26)$$

This results in a variational functional for  $d^2 E / d\mathcal{E}^2$  which couples states of symmetry  $k_i$  to states of symmetry  $k_{i+1}$ :

$$\begin{aligned} \frac{d^2 E}{d^2 \mathcal{E}^2} &= \frac{2}{N} \left[ \sum_{i=0}^{N-1} \left( \langle u_{k_i}^1 | H_{k_i, k_i}^0 - E_{k_i}^0 | u_{k_i}^1 \rangle \right) \right. \\ &\quad \left. - \frac{Na}{2\pi} \text{Im} \sum_{i=0}^{N-1} \left( \frac{\langle u_{k_i}^1 | u_{k_{i+1}}^0 \rangle}{\langle u_{k_i}^0 | u_{k_{i+1}}^0 \rangle} + \frac{\langle u_{k_i}^0 | u_{k_{i+1}}^1 \rangle}{\langle u_{k_i}^0 | u_{k_{i+1}}^0 \rangle} \right) \right]. \end{aligned} \quad (3.27)$$

When the distance  $\Delta k = 2\pi / (Na)$  between two consecutive  $k$ -points is small, the states  $u_{k_{i\pm 1}}^0$  can be expanded in a series with respect to  $\Delta k$ :

$$\begin{aligned} |v_{k_i}^{\pm}(\Delta k)\rangle &= |u_{k_{i\pm 1}}^0\rangle \\ &= |u_{k_i}^0\rangle \pm \left| \frac{d}{dk} u_{k_i}^0 \right\rangle \Delta k + \frac{1}{2!} \left| \frac{d^2}{dk^2} u_{k_i}^0 \right\rangle \Delta k^2 \pm \dots, \end{aligned} \quad (3.28)$$

which defines the states  $v_{k_i}^{\pm}(\Delta k)$ . The argument of the Im function in the interaction term of functional (3.27) can then be written as a function of  $\Delta k$  (a similar development was used in Ref. [61]):

$$\sum_{i=0}^{N-1} \left( \frac{\langle u_{k_i}^1 | v_{k_i}^+(\Delta k) \rangle}{\langle u_{k_i}^0 | v_{k_i}^+(\Delta k) \rangle} + \frac{\langle v_{k_i}^-(\Delta k) | u_{k_i}^1 \rangle}{\langle v_{k_i}^-(\Delta k) | u_{k_i}^0 \rangle} \right). \quad (3.29)$$

Expanding this expression in terms of  $\Delta k$  and using the orthonormality conditions at zeroth and first order, we find that the first nonreal term is purely imaginary and of order  $\Delta k$ :

$$\sum_{i=0}^{N-1} \left( \langle u_{k_i}^1 | \frac{d}{dk} u_{k_i}^0 \rangle - \langle \frac{d}{dk} u_{k_i}^0 | u_{k_i}^1 \rangle \right) \Delta k. \quad (3.30)$$



This term gives rise to the same interaction term found in the CP scheme (3.23). Similarly to the case of the polarizability of an isolated system, the higher order terms of  $\Delta k$  in the finite-field functional (3.27), can be regarded as a perturbation to the CP functional (3.23). The lowest nonreal term of higher order determines how the  $\epsilon_\infty$  calculated by the finite-field scheme converges for increasing  $N$  to that calculated in the CP scheme. We find that the first nonreal term of higher order in (3.29) is of order  $\Delta k^3$ . Therefore, the leading term describing the difference between the finite-field (3.27) and CP (3.23) functionals is of order  $\Delta k^2$ . Hence, the  $\epsilon_\infty$  obtained with the finite-field scheme converges to the one obtained in the CP scheme like  $1/L^2$ , where  $L = N \cdot a$ .

To illustrate this behavior, we calculated the high-frequency dielectric constant  $\epsilon_\infty$  of bulk silicon within the CP and finite-field schemes. We used a theoretical lattice constant of 10.14 a.u. [56]. We carried out the finite-field calculation using a finite electric field of intensity <sup>3</sup>  $1 \cdot 10^{-3}$  a.u. We adopted cubic supercells and sampled their Brillouin zone at the  $\Gamma$  point, corresponding to a  $k$ -point sampling of the Brillouin zone of the primitive cubic cell as in (3.21). We used a normconserving pseudopotential [59] and an energy cutoff of 20 Ry in the plane-wave expansion of the valence wave functions. The exchange and correlation energy is given within the local density approximation. As a reference, we also calculated a fully converged value for  $\epsilon_\infty$  with the same technical ingredients using a 8-atom cubic cell and a set of 56 special  $k$ -points [60] in the irreducible Brillouin zone [70]. We found a converged value of 13.1, in good agreement with experiment (11.4) [58] and similar calculations in the literature (12.7) [62]. Figure 3.4 shows the results as a function of supercell size  $L$ . We considered supercells containing 8, 64, 216, and 512 Si atoms. At small  $L$ , the CP scheme shows significant deviations with respect to the converged result, but it is found to converge rapidly at large  $L$ . We found that the convergence of the CP result is well described by  $\exp(-L/\lambda)/L$  with  $\lambda = 15.2$  bohr. On the other hand, the finite-field result remains closer to the converged result over the range of investigated  $L$ , but its convergence rate at large  $L$  is inferior. The same qualitative behavior was observed for the finite-field calculation in Ref. [42]. In the inset of Fig. (3.4), we display the difference

---

<sup>3</sup>An electric field of  $0.5 \cdot 10^{-4}$  a.u. was used for the supercell containing 512 Si atoms.

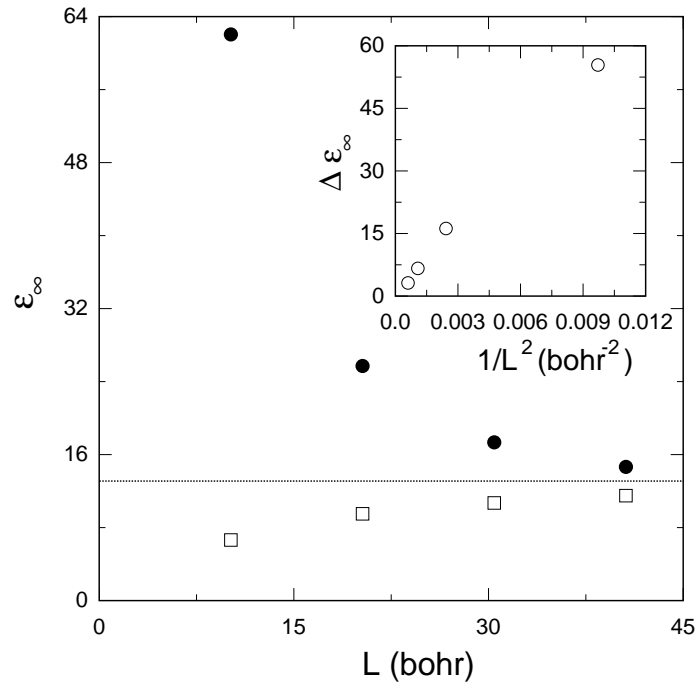


Figure 3.4: High-frequency dielectric constant  $\epsilon_\infty$  of bulk silicon versus the size  $L$  of the adopted cubic supercell, in the conventional perturbational (disc) and the finite-field (square) schemes, for a  $\Gamma$ -point sampling. The dotted line corresponds to the asymptotic value, obtained by a separate calculation with a sufficiently dense sampling of the Brillouin zone. Inset: Difference between the dielectric constants obtained with the two schemes, plotted versus  $1/L^2$ .

between the dielectric constants  $\epsilon_\infty$  in the two schemes as a function of  $1/L^2$ . The close to linear behavior confirms the general derivation exposed above.

The prefactor determining the  $1/L^2$  convergence rate of the finite-field dielectric constant towards the CP one depends on higher order derivatives of  $u_{k_i}^0$  with respect to  $k$ . In wide band-gap materials, the wave functions  $u_{k_i}^0$  as a function of  $k_i$  in the Brillouin zone are generally smoother than for silicon, resulting in a faster convergence. We illustrate this property for two practical cases, rather than deriving an explicit expression for the prefactor, which is cumbersome. We considered a 64-atom model of crystalline MgO as in Section 3.3 and a 72-atom model of vitreous silica [21]. In the previous section, we found using the finite-field scheme dielectric constants  $\epsilon_\infty$  of 2.79 and 2.00, respectively. These should be compared with 3.04 and 2.14, respectively, which we obtained using the CP scheme described in Chapter 2. The difference between the values obtained with the two schemes for MgO and vitreous silica (8 and 7%, respectively) is significantly lower than given in Fig. (3.4) for a 64-atom model of bulk silicon (63%), demonstrating the role of the prefactor. The relative difference between the two methods gives a measure of the expected error. For instance, we estimate an error of 4% for a model of vitreous silica containing 150 atoms, which is a system size within the scope of present calculations [63].

### 3.5 Extension to ultrasoft pseudopotentials

The finite field functional (3.1) can easily be generalized to treat ultrasoft pseudopotentials following the same approach introduced in Chapter 2. By using the same notation of Sec. 2.1, we can express the matrix elements  $S_{ij}$  in terms of *pseudo* wave functions:

$$S_{ij} = \langle \tilde{\Psi}_i | T^\dagger e^{2\pi i x/L} T | \tilde{\Psi}_j \rangle. \quad (3.31)$$

By applying the theorem (2.5), we can write:

$$T^\dagger e^{2\pi i x/L} T = e^{2\pi i x/L} + \sum_{k,l} |\beta_k\rangle \langle \langle \Phi_k | e^{2\pi i x/L} | \Phi_l \rangle - \langle \tilde{\Phi}_k | e^{2\pi i x/L} | \tilde{\Phi}_l \rangle \rangle \langle \beta_l|. \quad (3.32)$$

Therefore, we define:

$$C_{kl} = \int_R \left[ \Phi_k^*(\mathbf{r}) e^{2\pi i x/L} \Phi_l(\mathbf{r}) + \tilde{\Phi}_k^*(\mathbf{r}) e^{2\pi i x/L} \tilde{\Phi}_l(\mathbf{r}) \right] d\mathbf{r}. \quad (3.33)$$

The terms  $C_{kl}$  can be calculated from the augmentation charge functions  $Q_{k,l}$  defined in Sec. 2.1:

$$C_{kl} = \int_R Q_{k,l}(\mathbf{r}) e^{2\pi i x/L} d\mathbf{r}. \quad (3.34)$$

We finally obtain:

$$S_{ij} = \langle \tilde{\Psi}_i | \left[ e^{2\pi i x/L} + \sum_{kl} |\beta_k\rangle C_{kl} \langle \beta_l| \right] | \tilde{\Psi}_j \rangle. \quad (3.35)$$

It's worth noting that, for ultrasoft pseudopotentials, the terms  $S_{ij}$  depend on the positions of the nuclei in the unit cell. Therefore, an extra term appears in the expression of the atomic forces.

With the same reasoning, we extended the perturbative method for the dielectric tensors described in Ref. [42] to treat ultrasoft pseudopotentials. This method corresponds to the application of a perturbative expansion to functional (3.1). In the ultrasoft implementation, the pseudo-identity operator  $S$  [which must not be confused with  $S$  in Eq. (3.3)] does not depend on the perturbation (i.e. the electric field). Hence, the constraints order are imposed at first by projecting the gradient of the second order functional with respect to the first order wavefunctions on the subspace spanned by the unoccupied states. We use the operator (see Appendix B):

$$S \sum_c |\tilde{\Psi}_c^{(0)}\rangle \langle \tilde{\Psi}_c^{(0)}| = 1 - S \sum_v |\tilde{\Psi}_v^{(0)}\rangle \langle \tilde{\Psi}_v^{(0)}|, \quad (3.36)$$

where  $\tilde{\Psi}_i^{(0)}$  are the unperturbed wave functions, and the indices  $v$  and  $c$  run over the valence and conduction states, respectively (see Appendix B). We note that the extension of the finite-field functional (3.1) to treat ultrasoft pseudopotentials is considerably less involved than the treatment of these pseudopotentials within a perturbational approach (see Chapter 2).

## Chapter 4

# Application to v-SiO<sub>2</sub>

In this chapter we apply the scheme developed in Chapter 2 to study the Raman spectrum of vitreous silica. To estimate the accuracy of this approach, we first calculate the Raman intensities of  $\alpha$ -quartz, for which detailed experimental results are available. An overall agreement of 13% between theory and experiment supports the application of a first-principles approach to the Raman spectrum of vitreous silica. We calculate the Raman spectrum for a model of v-SiO<sub>2</sub> previously obtained by first principles molecular dynamics [21]. The accurate description of the Raman couplings allows us to estimate from the *experimental* Raman spectrum the concentration of three- and four-fold rings in this glass.

### 4.1 Raman spectrum of $\alpha$ -quartz

#### 4.1.1 Theoretical formulation: Raman activities in crystals

We outline the formulation which we used for the calculation of Raman activities. We only focus on first-order processes, which involve a single phonon excitation. The momentum conservation imposes that only phonons of wavevectors  $\mathbf{q}$  close to the center of the Brillouin zone can be excited. In practice, adopting the dipole approximation, we only consider center-zone phonons ( $\mathbf{q} = 0$ ) and account for the dependence on the direction of  $\mathbf{q}$  resulting from the long-range nature of the Coulomb field in polar materials [64, 65].

Using a similar notation as Gonze and Lee [24], we express the dynamical matrix for

$\mathbf{q} \rightarrow 0$  as a sum of an analytical and a non-analytical matrix:

$$\tilde{D}_{\alpha i, \beta j}(\mathbf{q} \rightarrow 0) = \tilde{D}_{\alpha i, \beta j}(\mathbf{q} = 0) + \tilde{D}_{\alpha i, \beta j}^{\text{NA}}(\mathbf{q} \rightarrow 0), \quad (4.1)$$

where the greek and latin indices run over the atoms in the primitive cell and over the three Euclidean directions, respectively. The analytical part is given by

$$\tilde{D}_{\alpha i, \beta j}(\mathbf{q} = 0) = \frac{1}{\sqrt{M_\alpha M_\beta}} \frac{\partial^2 E_{\text{tot}}}{\partial r_{\alpha i} \partial r_{\beta j}}, \quad (4.2)$$

where  $E_{\text{tot}}$  is the total energy of the system and  $M_\alpha$  are the masses of the atoms. The non-analytical part depends on the direction of the momentum  $\mathbf{q}$  exchanged with the radiation field [64]:

$$\tilde{D}_{\alpha i, \beta j}^{\text{NA}}(\mathbf{q} \rightarrow 0) = \frac{1}{\sqrt{M_\alpha M_\beta}} \frac{4\pi}{\Omega} \frac{(\sum_k \mathbf{q}_k Z_{\alpha, ki}^*) (\sum_i \mathbf{q}_{k'} Z_{\beta, k' j}^*)}{\sum_{kk'} \mathbf{q}_k \epsilon_{kk'}^\infty \mathbf{q}_{k'}}, \quad (4.3)$$

where  $\Omega$  is the volume of the primitive cell,  $\epsilon_{ij}^\infty$  the high-frequency dielectric tensor, and  $Z_{\alpha, ij}^*$  the Born dynamical charge tensors defined as the induced polarization along the direction  $i$  by a unitary displacement of atom  $\alpha$  in the direction  $j$  [66]:

$$Z_{\alpha, ij}^* = \frac{\partial^2 E_{\text{tot}}}{\partial \mathcal{E}_i \partial r_{\alpha j}}. \quad (4.4)$$

For a given direction of  $\mathbf{q}$ , the frequencies  $\omega_n$  and the corresponding normalized eigenmodes  $v_{\alpha i}^n$  of the excited phonons are obtained by diagonalizing the dynamical matrix in Eq. (4.1). The atomic displacements  $u_{\alpha i}^n$  associated with the mode  $n$  are then given by:

$$u_{\alpha i}^n = \frac{1}{\sqrt{M_\alpha}} v_{\alpha i}^n. \quad (4.5)$$

We obtain transverse-optic (TO) and longitudinal-optic (LO) modes as follows [24]. For a given mode  $n$  of the analytical part of the dynamical matrix, we define the associated three-component mode effective charge vector [24]:

$$\bar{Z}_i^n = \sum_{\alpha i} Z_{\alpha, ij}^* u_{\alpha j}^n. \quad (4.6)$$

When  $\mathbf{q} \cdot \bar{\mathbf{Z}}^n = 0$ , the eigenmode  $n$  of the analytical part is also an eigenmode with the same frequency of the full dynamical matrix, and is identified as a TO mode. In general,

the LO modes are obtained from the full dynamical matrix by taking  $\mathbf{q} \parallel \bar{\mathbf{Z}}^n$  for every  $\bar{\mathbf{Z}}^n$ . However, in practice, symmetry constraints often limit the number of different directions of  $\bar{\mathbf{Z}}^n$ .

In a Raman scattering process, an incoming photon of frequency  $\omega_L$  and polarization  $\mathbf{e}_L$  is scattered to an outgoing photon of frequency  $\omega_S$  and polarization  $\mathbf{e}_S$  either creating (Stokes process) or annihilating (anti-Stokes process) a phonon of frequency  $\omega_k$ . Because of energy conservation,  $\omega_S = \omega_L \pm \omega_k$ , where the minus (plus) sign applies to the (anti-)Stokes process. We here consider non-resonant Raman scattering processes which can be described in the Placzek approximation [16, 67]. The power cross section of the Stokes process involving a phonon of eigenmode  $k$  reads (in esu units) [16, 67]:

$$\begin{aligned} \frac{d\sigma}{d\Omega} &= |\mathbf{e}_S \cdot \mathbf{R}^k \cdot \mathbf{e}_L|^2 \\ &= \frac{\omega_S^4 V}{c^4} |\mathbf{e}_S \cdot \boldsymbol{\alpha}^k \cdot \mathbf{e}_L|^2 \frac{\hbar}{2\omega_k} (n_k + 1), \end{aligned} \quad (4.7)$$

where  $V$  is the volume of the scattering sample,  $c$  is the speed of light,  $n_k$  is the Boson factor,

$$n_k = \frac{1}{\exp(\hbar\omega_k/k_B T) - 1}. \quad (4.8)$$

The second rank tensor  $\mathbf{R}^k$  in Eq. (4.7) is referred to as the Raman tensor associated to the vibrational eigenmode  $k$  [16]. The Raman susceptibility  $\boldsymbol{\alpha}^k$  is defined as [16]:

$$\alpha_{ij}^k = \sqrt{\Omega} \sum_{\alpha l} \frac{\partial \chi_{ij}}{\partial r_{\alpha l}} u_{\alpha l}^k, \quad (4.9)$$

where  $\chi_{ij}$  is the dielectric susceptibility tensor:

$$\chi_{ij} = \frac{\epsilon_{ij}^\infty - \delta_{ij}}{4\pi}. \quad (4.10)$$

In the case of an anti-Stokes process, the definition of  $\omega_S$  changes and the factor  $(n_k + 1)$  in Eq. (4.7) must be replaced by  $n_k$ . We note that the Raman susceptibility defined in Eq. (4.9) is independent of the volume of the adopted cell  $\Omega$ , because  $\partial \chi_{ij} / \partial r_{\alpha l}$  scales as the inverse of  $\Omega$ .

### 4.1.2 Raman scattering in $\alpha$ -quartz

#### Structure

The  $\alpha$ -quartz structure is described by the space group  $D_3^4$  (P3<sub>1</sub>21) and its hexagonal primitive cell contains three SiO<sub>2</sub> units [68]. The atomic positions in the primitive cell are identified by four internal cell parameters:  $u$ ,  $x$ ,  $y$ , and  $z$ . We obtained relaxed structural parameters of  $\alpha$ -quartz within the local density approximation [69] to density functional theory [70]. The valence wave functions were expanded in a plane-wave basis set defined by an energy cutoff of 60 Ry, while the core-valence interactions were described by normconserving pseudopotentials for both Si (Ref. [59]) and O atoms [71]. We sampled the Brillouin zone using a single special  $k$ -point at  $(\frac{1}{3}, 0, \frac{1}{4})$  in crystalline coordinates, which is sufficient for obtaining converged results [73]. Our calculated structural parameters are reported in Table 4.1, where they are compared to experimental [72] and previous theoretical results [73]. The three sets of data are found to be in excellent agreement.

Table 4.1: Structural parameters of  $\alpha$ -quartz. Lattice cell parameters and bond lengths are given in Å, while internal cell parameters are in cell units.

	Theory		Experiment
	Present	Ref. [73]	Ref. [72]
$a$	4.870	4.814	4.916
$c$	5.346	5.321	5.405
$u$	0.471	0.461	0.470
$x$	0.415	0.410	0.413
$y$	0.265	0.281	0.267
$z$	0.121	0.108	0.119
Si-O	1.59		1.60
Si-O-Si	144.8°	139.1°	143.7°



### Dielectric tensor and Born charge tensors

Applying a linear response approach [19, 74], we calculated the high-frequency dielectric tensor and the Born charge tensors [70]. The dielectric tensor of  $\alpha$ -quartz is diagonal and assumes different values for parallel and perpendicular directions to the optical axis ( $z$ -axis). Our calculated results are reported in Table 4.2, where they are compared with experimental data [75] and results from a previous density-functional calculation [73]. The three sets of data are in excellent agreement.

In the structure of  $\alpha$ -quartz all Si atoms and all O atoms are equivalent by symmetry. We therefore give in Table 4.3 only the Born charge tensors of specific Si and O atoms. For comparison, also the results obtained in Ref. [73] are reported in Table 4.3. The agreement is very good. We attribute the small differences in the off-diagonal terms to the different structural parameters in the two calculations (see Table 4.1).

Table 4.2: Diagonal elements of the high-frequency dielectric tensor of  $\alpha$ -quartz, parallel ( $\epsilon_{\parallel}^{\infty}$ ) and perpendicular ( $\epsilon_{\perp}^{\infty}$ ) to the optical axis.

	Theory		Experiment
	Present	Ref. [73]	Ref. [75]
$\epsilon_{\parallel}^{\infty}$	2.457	2.383	2.566
$\epsilon_{\perp}^{\infty}$	2.429	2.356	2.527

### Vibrational frequencies

We considered first the analytic part of the dynamical matrix at the  $\Gamma$  point. The eigenmodes transform according to the irreducible representations of the symmetry group  $D_3$ : the nondegenerate  $A_1$  and  $A_2$ , and the doubly degenerate  $E$ . The representations  $A_2$  and  $E$  are infrared active, while  $A_1$  and  $E$  are Raman active.

To derive LO-TO splittings, we calculated the vector  $\bar{\mathbf{Z}}^n$  belonging to each eigenmode  $n$ . For the  $A_1$  modes,  $\bar{\mathbf{Z}}^n = 0$ . Hence, the  $A_1$  do not depend on the direction of  $\mathbf{q}$ . For

Table 4.3: Calculated Born charge tensors for silicon and oxygen atoms, compared to results of a previous calculation [73]. The charge tensors are given in atomic units.

Present			Ref. [73]		
Silicon atom in $(u, 0, 0)$					
3.021	0.000	0.000	3.016	0.000	0.000
0.000	3.671	-0.224	0.000	3.633	-0.324
0.000	0.257	3.450	0.000	0.282	3.453
Oxygen atom in $(x, y, z)$					
-1.413	0.564	0.505	-1.326	0.480	0.298
0.519	-1.915	-0.615	0.429	-1.999	-0.679
0.447	-0.648	-1.715	0.222	-0.718	-1.726

the  $A_2$  modes,  $\bar{\mathbf{Z}}^n$  is parallel to the  $z$ -axis, resulting in different frequencies for LO and TO excitations. In Table 4.4, we report frequencies for  $A_{2T}$  and  $A_{2L}$  modes obtained by diagonalizing the full dynamical matrix with  $\mathbf{q}$  orthogonal and parallel to the  $z$ -axis, respectively. The doubly degenerate modes  $E$  are characterized by a couple of orthogonal vectors  $\bar{\mathbf{Z}}^n$  spanning the  $xy$  plane. Thus, a LO-TO splitting of the  $E$  modes occurs for  $\mathbf{q}$  vectors orthogonal to the  $z$ -axis, while the  $E$  modes remain degenerate at the  $E_T$  frequencies for  $\mathbf{q}$  parallel to the  $z$ -axis.

In Table 4.4, we compare our calculated frequencies [70] with results from another density-functional calculation [73] and with two sets of experimental data. The first set of experimental data corresponds to extrapolations to 0 K of frequencies measured in Refs. [75] and [77], as detailed in Ref. [73]. The second set of experimental data was obtained in Ref. [78] at room temperature. Overall, the agreement between the present theoretical values and experiment is very good, with errors generally smaller than 5%. The differences between the theoretical approaches should again be attributed to the different equilibrium structures.

Table 4.4: Vibrational frequencies of  $\alpha$ -quartz at the  $\Gamma$  point. The frequencies are given in  $\text{cm}^{-1}$ .

Theory		Experiment		Theory		Experiment	
Present	Ref. [73]	Refs. [75, 77]	Ref. [78]	Present	Ref. [73]	Refs. [75, 77]	Ref. [78]
<i>A<sub>1</sub></i>							
193.7	238.9	219	207				
355.0	339.3	358	356				
460.1	461.7	469	464				
1123.3	1061.0	1082	1085				
<i>A<sub>2T</sub></i>				<i>A<sub>2L</sub></i>			
366.4	341.4	361.3		391.4	365.7	385	
489.3	493.4	499		533.8	540.5	553	
792.2	762.4	778		815.0	784.7	791	
1115.4	1056.5	1072		1272.6	1218	1230	
<i>E<sub>T</sub></i>				<i>E<sub>L</sub></i>			
120.9	133.3	133	128	121.0	133.4	133	128
257.3	261.3	269	265	258.5	263.2	269	265
390.0	377.6	393.5	394	398.6	389.2	402	401
448.0	443.8	452.5	450	500.2	498.6	512	509
703.3	690.8	698	697	708.7	694.5	701	697
809.6	791.7	799	795	824.0	803.9	811.5	807
1108.7	1045.0	1066	1072	1185.7	1123.9	1155	1162
1190.8	1128.1	1158	1162	1270.6	1209.5	1227	1235

### Raman activities

The Raman susceptibility defined in Eq. (4.9) requires the derivatives of the polarizability tensor with respect to the atomic displacements. We calculated these derivatives by finite differences using polarizability tensors obtained by applying a density-functional linear response approach [19, 74]. For every Cartesian direction, we used finite displacements of  $\pm 1$  and  $\pm 2\%$  of the unit cell parameter  $a$  to estimate the derivatives of the polarizability tensor [81, 79]. We calculated derivatives of the polarizability tensor only for displacements of a single O and a single Si atom. The results are given in Table 4.5. Note that the matricial norm of the O tensor in Table 4.5 is almost a factor of three larger than that of the Si tensor. The derivatives with respect to the displacements of the other atoms are determined by symmetry.

Table 4.5: Calculated derivatives of the dielectric polarizability tensor with respect to displacements along the Cartesian axes for silicon and oxygen atoms. The derivatives are given in  $(4\pi)^{-1} \cdot 10^{-2} \times \text{bohr}^{-1}$ .

$\partial\chi_{ij}/\partial x$			$\partial\chi_{ij}/\partial y$			$\partial\chi_{ij}/\partial z$		
Si atom in $(u, 0, 0)$								
-0.29	-0.06	0.01	0.11	-0.99	2.12	0.50	4.61	2.40
-0.06	0.04	2.64	-0.99	0.56	0.06	4.61	0.76	-0.05
0.01	2.64	-0.57	2.12	0.06	0.28	2.40	-0.05	1.52
O atom in $(x, y, z)$								
-3.46	-0.54	1.57	-3.30	-0.46	0.20	3.11	-0.65	-2.55
-0.54	-2.38	-0.13	-0.46	-9.02	0.63	-0.64	2.50	-0.45
1.57	-0.13	-3.35	0.20	0.63	-4.21	-2.55	-0.45	6.55

By symmetry, the Raman tensors assume a well defined form. Following the notation of Loudon [80], the Raman tensors of the  $A_1$  modes are given by

$$\begin{pmatrix} a & & \\ & a & \\ & & b \end{pmatrix}, \quad (4.11)$$

while those associated to  $E(x)$  and  $E(y)$  modes assume the forms

$$\begin{pmatrix} c & & \\ & -c & d \\ & d & \end{pmatrix} \text{ and } \begin{pmatrix} & -c & -d \\ -c & & \\ -d & & \end{pmatrix}, \quad (4.12)$$

respectively. For the modes  $E(x)$  and  $E(y)$ , the associated charge vectors  $\bar{\mathbf{Z}}^n$ , defined in Eq. (4.6), are parallel to the  $x$  and  $y$  axes, respectively.

The Raman tensors depend on the direction of the wavevector  $\mathbf{q}$ . The calculation proceeds as follows. First, we diagonalized the full dynamical matrix whose non-analytical term is determined by the direction of  $\mathbf{q}$ . The resulting eigenmodes together with the calculated derivatives of the polarizability tensor gave the Raman susceptibility in Eq. (4.9). The Raman tensors were then obtained from Eq. (4.7).

In order to compare with experimental data [78], we took  $\mathbf{q}$  parallel to the  $x$  axis. For this choice, three kind of modes are observed:  $A_1$ ,  $E_T$  and  $E_L$ . The forms of the Raman tensors associated to these modes are given in Eqs. (4.11) and (4.12). For this particular choice of  $\mathbf{q}$ , the  $E_T$  and  $E_L$  have the form of the  $E(y)$  and  $E(x)$  tensors, respectively. Calculated values of  $a^2$ ,  $b^2$ ,  $c^2$ , and  $d^2$  characterizing the Raman tensors for the Stokes process are given in Table (4.6). Note that the experimental data are generally obtained at room temperature, whereas the theoretical results account for the temperature only through the statistical Boson factor.

The absolute intensities associated to the strongest  $A_1$  mode (at about  $466 \text{ cm}^{-1}$ ) were determined experimentally by Gorelik and Sushchinskii [82]. Using an argon laser ( $\hbar\omega_L=15308 \text{ cm}^{-1}$ ), these researchers measured  $a^2$  and  $b^2$  to be  $0.2$  and  $0.3 \times 10^{-7} \text{ sterad}^{-1} \text{ cm}^{-1}$  [82, 16], in fair agreement with our calculated values of  $0.39$  and  $0.37 \times 10^{-7} \text{ sterad}^{-1} \text{ cm}^{-1}$ , respectively. In Table (4.6), we carried out a more detailed comparison between theory and experiment considering the more extensive set of Raman intensities measured by Masso, She, and Edwards [78]. However, because these authors only gave relative intensities, we estimated the unknown scaling factor  $f$  by minimizing the relative error  $\Delta$ ,

Table 4.6: Theoretical Raman intensities for the Stokes process in  $\alpha$ -quartz, obtained by first principles are compared to the experimental values of Ref. [78]. The vibrational modes are identified by the theoretical frequencies (in  $\text{cm}^{-1}$ ). The correspondence with the experimental modes is according to Table 4.4. The theoretical absolute intensities per unit volume can be obtained by multiplying the values in the table by  $\omega_S^4$  and by  $1/f=2.368 \cdot 10^{-70} \text{ sterad}^{-1} \text{cm}^{-1} \text{s}^4$ . The experimental data are only known on a relative scale [78].

Mode	First principles		Experiment		Mode	First principles		Experiment		
$A_1$	$a^2$	$b^2$	$a^2$	$b^2$						
193.7	601.5	693.7	484	619						
355.0	60.4	33.3	38	55						
460.1	898.7	864.3	906	1000						
1123.3	3.7	28.3	2.3	31						
$E_T$	$c^2$	$d^2$	$c^2$	$d^2$	$E_L$	$c^2$	$d^2$	$c^2$	$d^2$	
120.9	117.9	68.2	125	62	121.0	117.3	68.6	-	-	
257.3	1.6	22.6	<1	28	258.5	1.7	24.1	-	-	
390.0	21.6	1.0	11	<1	398.6	22.1	5.5	6	2	
448.0	0.3	19.1	<1	13	500.2	1.4	11.5	<1	10	
703.3	10.5	5.2	-	-	708.7	9.7	5.2	-	-	
809.6	2.5	17.8	<1	14	824.0	3.2	24.7	<1	20	
1108.7	1.5	13.7	<1	2.7	1185.7	25.2	11.2	-	-	
1190.8	32.6	5.8	23	5.5	1270.6	7.3	2.9	3.7	<1	

defined as:

$$\Delta = \sqrt{\frac{\sum_n (I_n^{\text{theo}} - f I_n^{\text{expt}})^2}{\sum_n f^2 (I_n^{\text{expt}})^2}}, \quad (4.13)$$

where  $I^{\text{theo}}$  and  $I^{\text{expt}}$  are the theoretical and experimental intensities, respectively, and where the sum over  $n$  is over all entry in Table (4.6) for which an experimental result is available. For the sake of comparison, the theoretical data in Table (4.6) were rescaled by the factor of  $1/f$ .

Calculated and measured intensities show overall good agreement. The theory correctly describes the important difference in magnitude between the intensities of the  $A_1$  and  $E$  modes. Among the  $A_1$  modes, the lines at 193.7 and 460.1  $\text{cm}^{-1}$  are found to be much stronger than those at 355.0 and 1123.3  $\text{cm}^{-1}$ , in agreement with the experimental trend. However, the relative ordering of the intensities  $a^2$  and  $b^2$  is not always reproduced. Among the  $E$  modes, the line at 120.9  $\text{cm}^{-1}$  stands out as the strongest and is well described by our theory. The quality of the comparison can be quantified by the error  $\Delta$  in Eq. (4.13), which is found to be 13% for the optimal scaling factor.

It is interesting to observe that the values of  $c^2$  and  $d^2$  for the two components of a LO-TO doublet are different due to the electrooptic effect associated with the E vibrations [78]. In particular, we focus on the three LO-TO doublets identified by the theoretical frequencies at 390-399, 448-500, and 810-824  $\text{cm}^{-1}$ , for which LO-TO ratios of intensities could be determined experimentally. For the ratio  $d^2(\text{LO})/d^2(\text{TO})$  associated to the 448-500 and 810-824 doublets, we found 0.60 and 1.38 in good agreement with the measured values of 0.79 and 1.43, respectively. The agreement between theory and experiment is less good for the ratio  $c^2(\text{LO})/c^2(\text{TO})$  of the 390-399 doublet, for which we calculated a value of 1.0 while a value of 0.55 was found experimentally.

The overall good agreement between the first-principles and the experimental Raman activities in  $\alpha$ -quartz justifies the first-principles calculation of the Raman spectrum for vitreous silica, a material of which the structure is not fully determined experimentally.

## 4.2 Raman spectrum of vitreous silica

### 4.2.1 Theoretical formulation

To model the Raman spectrum of a vitreous materials, we consider a large disordered structure in a periodic unit cell and apply the same scheme appropriate for crystalline systems described in Section 4.1.1. However, because of the space isotropy in vitreous materials, we then apply an opportune space average. In experimental setups, it is customary to record the Raman spectra in the HH and the HV configuration, in which the polarizations of the outgoing photons are parallel and orthogonal to the ingoing ones, respectively [67]. Using the isotropy of disordered solids, we express the contribution of the  $k$ th mode to the HH and HV Raman spectra as [16]:

$$I_{\text{HH}}^k = a_k^2 + \frac{4}{45}b_k^2, \quad (4.14)$$

$$I_{\text{HV}}^k = \frac{3}{45}b_k^2, \quad (4.15)$$

where  $a^k$  and  $b^k$  are obtained from:

$$\begin{aligned} a_k &= \frac{1}{3} \left( \alpha_{11}^k + \alpha_{22}^k + \alpha_{33}^k \right) \\ b_k^2 &= \frac{1}{2} \left[ \left( \alpha_{11}^k - \alpha_{22}^k \right)^2 + \left( \alpha_{11}^k - \alpha_{33}^k \right)^2 + \right. \\ &\quad \left. + \left( \alpha_{22}^k - \alpha_{33}^k \right)^2 \right] + 3 \left[ (\alpha_{12}^k)^2 + (\alpha_{13}^k)^2 + (\alpha_{23}^k)^2 \right]. \end{aligned} \quad (4.16)$$

Focusing on the Stokes process, in which a vibrational excitation is created by an incoming photon, we express the total power cross section as (in esu units):

$$I_{\text{HH,HV}}^P(\omega) = 4\pi \sum_k \frac{(\omega_L - \omega_k)^4 V}{c^4} I_{\text{HH,HV}}^k \frac{\hbar}{2\omega_k} [n(\omega_k) + 1] \delta(\omega - \omega_k), \quad (4.17)$$

where  $V$  is the volume of the scattering sample,  $\omega_L$  the frequency of the incoming photon,  $c$  the speed of light, and  $n(\omega)$  the Boson factor. In this work, we give the Raman intensities using the following reduced expression:

$$I_{\text{R}}^P(\omega) = \omega(\omega_L - \omega)^{-4} [n(\omega) + 1]^{-1} I^P(\omega). \quad (4.18)$$



Because of the lack of translational symmetry, we describe disordered materials by using unit cells of large size, and calculate the Raman spectra at the  $\Gamma$ -point without considering LO-TO splittings. Indeed, calculations for our model of v-SiO<sub>2</sub> showed that the LO-TO splittings of vibrational modes caused no significant change in the calculated Raman spectra.

### 4.2.2 First-principles Raman spectrum of v-SiO<sub>2</sub>

In our study of vitreous silica, we considered at first a model structure consisting of a network of cornersharing tetrahedra, generated by first-principles molecular dynamics [21]. This model structure contains 72 atoms in a periodically repeated cubic cell, at the experimental density (2.20 g/cm<sup>3</sup>). The inelastic neutron scattering and infrared absorption spectra were previously calculated for the same model structure and found in good agreement with experiment [22, 23]. The choice of this model structure was motivated by the opportunity of obtaining theoretical spectra associated to the three principal vibrational spectroscopies for the same atomic structure.

The polarizability was calculated within the local density approximation to density functional theory using the method developed in Chapter 2. We used a normconserving pseudopotential for Si [59] and an ultrasoft pseudopotential for O [31]. We used a plane wave basis to describe the wave functions and the electron density. We adopted cutoff energies of 24 Ry and 200 Ry for the wave functions and the electron density, respectively. The Brillouin zone was sampled at the sole  $\Gamma$  point. The vibrational frequencies  $\omega_k$  and eigenmodes  $\xi_j^k$  were taken from Ref. [22]. The derivatives  $\partial\chi/\partial\mathbf{R}$  were obtained for every atom in the model by taking finite differences of the polarizability tensors calculated as described above. We used atomic displacements of  $\pm 0.07$  bohr, in a regime in which the polarizability shows a linear dependence.

Theoretical and experimental spectra [5] are compared in Fig. 4.1. Since the experimental spectra are given on a relative scale, we rescaled the theoretical ones by a constant factor to match the integrated intensity of the experimental HH spectrum. The calculated Raman spectra show a fair agreement for the location of the principal peaks and for the

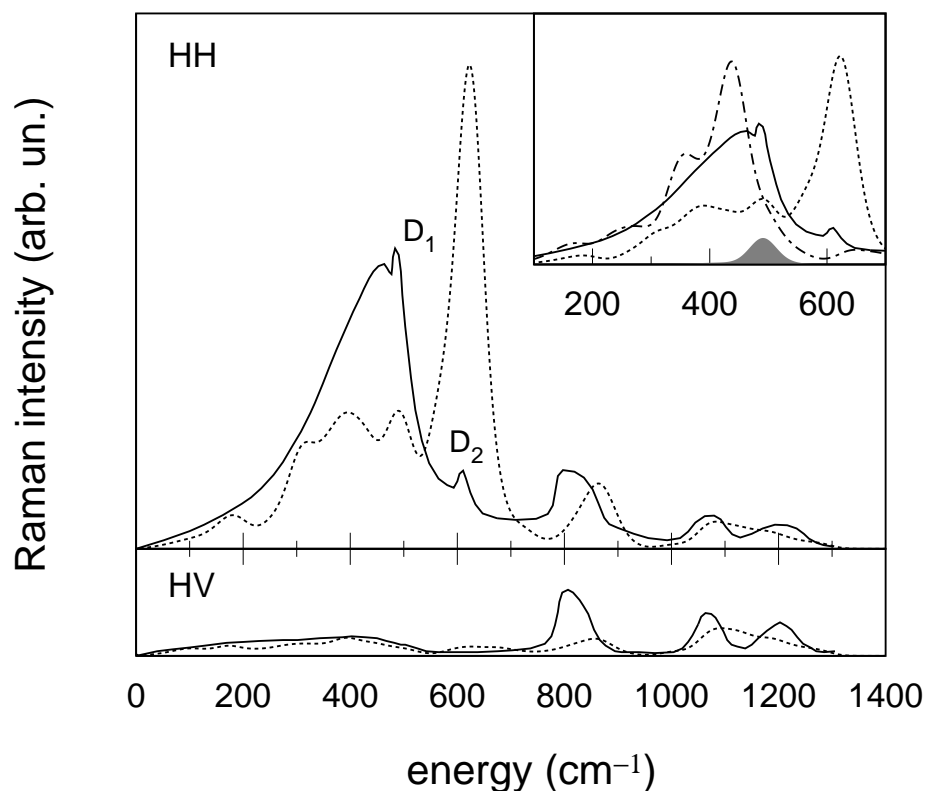


Figure 4.1: Calculated (dotted) and measured [5] (solid) reduced HH and HV Raman spectra of vitreous silica. The calculated spectra are scaled to match the integrated intensity of the experimental HH spectrum. The integrated Raman intensity under the theoretical HH curve is  $2.01 \cdot 10^{-7} \text{ bohr}^{-2} \cdot \text{amu}^{-1}$ . For clarity, the curves in the lower panel are magnified by a factor of two. A Gaussian broadening is used ( $22 \text{ cm}^{-1}$ ). Inset: HH Raman spectrum for the second model structure defined in the text (dot-dashed) compared to experiment (solid) and to the initial model structure (dotted). The contribution from the breathing vibration in the four-membered ring is shaded.

average ratio between the intensities of the HH and HV spectra. However, significant differences between theory and experiment occur in the HH spectrum for frequencies ranging from 300 to 700  $\text{cm}^{-1}$ , precisely where the  $D_1$  and  $D_2$  lines appear. In the calculated HH spectrum, the intensity of the large peak at  $\sim 450 \text{ cm}^{-1}$  is underestimated while the  $D_2$  line is more intense than in the experiment. This shift of intensity towards the  $D_2$  line is consistent with the occurrence of a high concentration of three-membered rings in our model structure [6], for which as much as 30% of the O atoms belong to such rings. This suggests that the differences between theory and experiment in Fig. 4.1 result from a different description of the intermediate range order in the model structure rather than from an inaccurate determination of the Raman intensities. This interpretation is supported by the good agreement between first-principles and experimental intensities found for  $\alpha$ -quartz (Sec. 4.1.2).

In order to define the properties that an improved model structure of vitreous silica should satisfy, we further analyze the sensitivity of the HH Raman spectrum to the intermediate range order. By considering the contribution from O and Si atoms separately, we found that the HH Raman spectrum in the frequency region below 1000  $\text{cm}^{-1}$  almost exclusively arises from the coupling to O motions. We then analyzed the tensors  $\partial\chi/\partial\mathbf{R}$  associated to O atoms in terms of a local basis set. This analysis shows that the intensity is principally given by the fully isotropic components resulting, for every O atom  $I$ , from bending motions along the bisector direction  $\hat{\mathbf{b}}_I$  of the Si-O-Si bond angle. The associated Raman coupling can thus be expressed in terms of a scalar coupling factor,

$$f_I = \frac{1}{3} V \text{Tr} \sum_{\gamma} \frac{\partial\chi_{\alpha\beta}}{\partial R_{I\gamma}} b_{I\gamma}, \quad (4.19)$$

normalized to be volume independent. The HH spectrum calculated on this basis is confronted in Fig. 4.2 with the one obtained with the full coupling tensors. This comparison shows that the  $f_I$  provide an excellent description of the HH spectrum for frequencies below 1000  $\text{cm}^{-1}$ . Note that the  $f_I$  do not contribute to the HV spectrum which arises solely from nonisotropic components [16]. This explains why the HV spectrum does not show defect lines.

The coupling factors  $f_I$  associated to the O atoms in the model structure show a clear

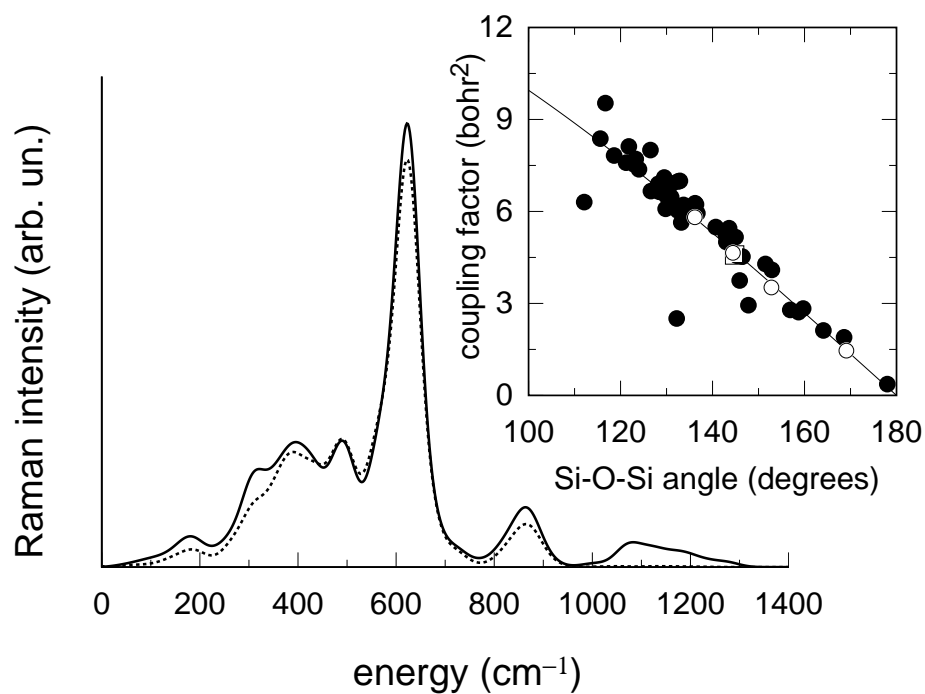


Figure 4.2: Full HH spectrum (solid) compared with the one obtained with coupling tensors in which only the fully isotropic components resulting from O bending motions are retained (dotted). Inset: Coupling factor  $f_I$  vs the Si-O-Si angle  $\theta$  for all O atoms in our model structure of vitreous silica (discs), in  $\alpha$ -quartz (square), and in a set of cristobalite structures (circles). The correlation is well described by Eq. (4.20) (solid).

correlation with the Si-O-Si bond angle  $\theta_I$  (Fig. 4.2, inset). This correlation is consistent with the relation:

$$f_I = (\alpha/3) \cos(\theta_I/2), \quad (4.20)$$

predicted by the bond polarizability model for a system of regular tetrahedral units as shown in Appendix A. Using the data in Fig. 4.2, we derived an optimal value of 46.5 bohr<sup>2</sup> for  $\alpha$ . The coupling factors calculated by first-principles for  $\alpha$ -quartz and for a set of cristobalite structures (see Appendix A) are also well described by (4.20) with the same value of  $\alpha$  (Fig. 4.2, inset).

### 4.2.3 Concentration of three- and four-membered rings

The modeling scheme introduced above provides us with a viable framework for deriving the concentration of three- and four-membered rings from the *experimental* HH Raman spectrum. We assumed that the contribution from O bending motions accounts for the entire Raman spectrum up to 1000 cm<sup>-1</sup>, via the coupling factors  $f_I$ . For the hypothetical case of a constant coupling factor, the intensity can be shown to be strictly proportional to the number of O atoms, because of the isotropic nature of the adopted coupling. Under such an assumption, the concentration of three- and four-membered rings has tentatively been estimated to be about 1% [83, 5]. In the present study, an estimate is provided which accounts for the dependence of the coupling factor on the Si-O-Si angle. On the basis of (4.20), we estimated this effect by considering the average Si-O-Si angle in three- ( $\theta_{3R} \approx 128^\circ$  [6]), and in four-membered rings ( $\theta_{4R} \approx 136^\circ$  [6]) with respect to that in vitreous silica ( $\langle\theta\rangle \approx 151^\circ$  [85, 86]). The ratios between the intensities of each of the defect lines and the background are therefore enhanced with respect to the concentration of O atoms in the small rings. We derived enhancement factors of  $\cos^2(\theta_{3R}/2)/\cos^2(\langle\theta\rangle/2) = 3.1$  and  $\cos^2(\theta_{4R}/2)/\cos^2(\langle\theta\rangle/2) = 2.2$  for the  $D_2$  and  $D_1$  lines, respectively. Using these enhancement factors and the experimental ratios between the intensities of the defect lines and the background, we obtained that 0.22% and 0.36% of the O atoms are found in three- and four-membered rings, respectively (Table 4.7). We stress that these results directly follow from the dependence on the Si-O-Si angle in (4.20), and do *not* depend on

the specificity of our model structure, nor on the value of  $\alpha$ .

Table 4.7: Oxygen concentrations in three- and four-membered rings as derived from the *experimental* HH Raman spectrum, compared to estimates from classical molecular dynamics (MD) [87, 88]. In parentheses, we give an upper bound as derived from the spread of intensities in the model structures. The values from Ref. [88] correspond to the lowest cooling rate.

	Present	MD simulations	
		Ref. [87]	Ref. [88]
O in threefold rings	0.22% (0.26%)	3%	6%
O in fourfold rings	0.36% (1.0%)	26%	36%

The estimated concentrations of O atoms in small rings differ significantly from those in our model structure (31% in three- and 17% in four-membered rings) [6], most likely as a consequence of the high cooling rate used in the first-principles generation procedure [21]. To verify that a better description of intermediate range order results in an improved accord between calculated and measured Raman spectra, we now consider a second model structure. From an extended set of 72-atom model structures generated by classical molecular dynamics [84], we selected the one with the lowest amount of small rings. The selected structure contains a single four-membered ring and no three-membered rings. The intermediate range order of this model structure is characterized by an average Si-O-Si angle of 152°, close to the experimental estimate of 151° [85, 86] and significantly different from the model structure used initially (137°). As for the initial model structure, we relaxed the atomic positions and calculated the vibrational frequencies and eigenmodes within a first-principles scheme. For the range of frequencies dominated by O bending motions, we obtained the associated HH Raman spectrum (Fig. 4.1, inset) using the coupling factors  $f_I$  as given by (4.20). The calculated spectrum for the second model structure noticeably improves the agreement between theory and experiment. The peak at  $\sim 440$  cm<sup>-1</sup> in the calculated spectrum agrees well, both in intensity and location, with the principal

experimental peak at  $\sim 450 \text{ cm}^{-1}$ . The theoretical spectrum does not show any feature in correspondence of the  $D_2$  line, in accord with the absence of three-membered rings. The contribution from the breathing vibration in the four-membered ring gives a peak<sup>1</sup> centered at  $490 \text{ cm}^{-1}$  in excellent agreement with the  $D_1$  line at  $495 \text{ cm}^{-1}$  [5].

To characterize the structure of vitreous silica beyond the short-range order, the ring-size statistics has emerged as a useful theoretical concept [2]. However, it has so far not been possible to provide any experimental data describing this statistics. Our results for the O concentrations trivially translate into amounts of three- and four-membered rings,<sup>2</sup> providing the first estimate of this kind based on an experimental Raman spectrum. We note that the atomic structures obtained with classical molecular dynamics simulations [87, 88] exhibit too large concentrations of small ring structures (Table 4.7), most likely because of excessively high cooling rates.

#### 4.2.4 Comparison with the vibrational density of states

Although the calculated HH and HV spectra differ from the experimental ones, this difference does not invalidate the significance of a comparison between the Raman spectra and the vibrational density of states, since both refer to the same model structure. The reduced HH Raman spectrum appears significantly different from the vibrational density of states (see Fig. 4.1). In part, this results from the intensity of the  $D_2$  line, which does not find a counterpart in the vibrational density of states. The  $D_1$  line associated to four-fold rings and occurring at about  $500 \text{ cm}^{-1}$  also modifies the HH spectrum with respect to the vibrational density of states. In the lowest part of the HH spectrum, up to  $200 \text{ cm}^{-1}$ , the Raman intensity appears suppressed with respect to the vibrational density of states. A resemblance between the HH spectrum and the vibrational density of states is only recognized for frequencies higher than  $\sim 750 \text{ cm}^{-1}$ . At variance, the HV reduced Raman spectrum closely resembles the vibrational density of states over the whole range of the

---

<sup>1</sup>This peak does not show up in the calculated spectrum because its width is overestimated as a result of the limited relaxation allowed in a 72-atom model structure [6].

<sup>2</sup>The values for three- and four-membered rings in the ring statistics (defined by shortest path analysis [2]) are obtained by multiplying the respective O concentrations by 2. We assumed isolated rings.

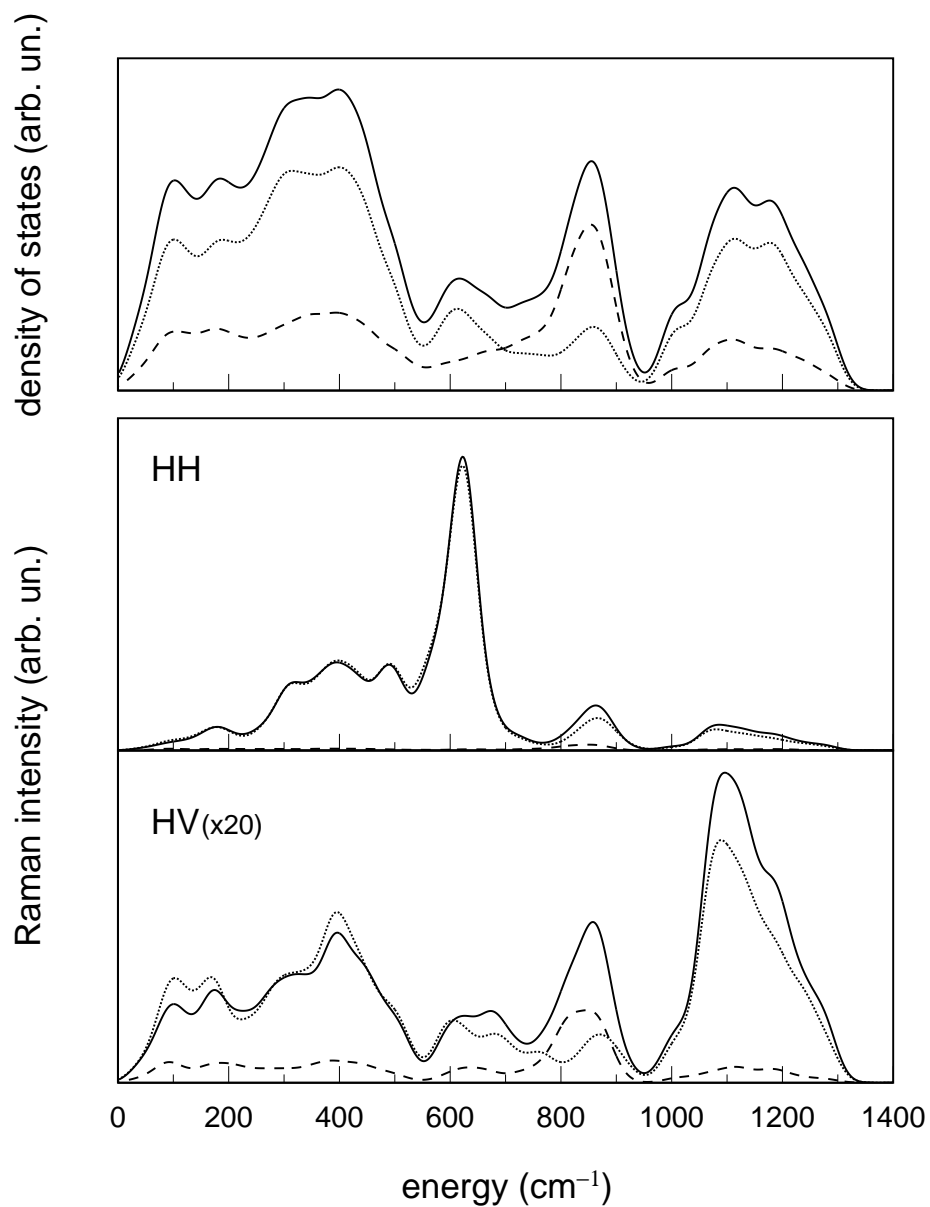


Figure 4.3: Vibrational density of states [22] and HH and HV reduced Raman spectra as calculated for the same model structure of vitreous silica (solid). Contributions from oxygen (dotted) and silicon (dashed) vibrations are given.



spectrum. This accord concerns both the location of the main peaks and their relative intensities. With respect to the vibrational density of states, only a slight enhancement of the high-frequency peak ( $> 1000 \text{ cm}^{-1}$ ) is found in the HV spectrum. The same effect is observed, to a lesser extent, for the peak at  $\sim 800 \text{ cm}^{-1}$ .

We extend further the comparison between the Raman spectra and the vibrational density of states by analysing the contributions from oxygen and silicon vibrations. The decomposition of the vibrational density of states into partial densities associated to specific atoms is well defined [22]. For the Raman spectra, we obtain partial spectra by considering only silicon or oxygen atoms in the sum over  $\alpha$  in Eq. (4.9). Unlike for the vibrational density of states, the sum of the partial Raman spectra does not recover the full spectrum, because of interference terms. However, this decomposition still gives a measure of the relative contributions from oxygen and silicon vibrations to the Raman intensities.

As shown in Fig. 4.3, the HH spectrum is dominated by oxygen vibrations, the silicon contribution being essentially negligible. The decomposition of the HV Raman spectrum further supports the resemblance with the vibrational density of states. The ratio between oxygen and silicon contributions appears only slightly higher in the HV spectrum than in the vibrational density of states.

Because of the prominent contribution of oxygen vibrations to the Raman spectra, we further decomposed this contribution according to three directions which characterize the local environment of each oxygen atom [89]. Considering the plane containing the Si atoms to which a given O atom is bonded, we defined the three directions as in Ref. [22]. We took the first direction orthogonal to the Si-O-Si plane (rocking), the second one along the bisector of the Si-O-Si angle (bending), and the third one orthogonal to the two previous ones (stretching). The decomposition was carried out by projecting the eigenmodes  $\mathbf{v}_\alpha^k$  on these directions prior to the calculation of the Raman tensors given in Eq. (4.9).

In Fig. 4.4, the oxygen contributions to rocking, bending, and stretching vibrations are expressed as ratios with respect to the total oxygen contribution. The decomposition of the vibrational density of states is from Ref. [22]. In all the decompositions in Fig. 2, the high-

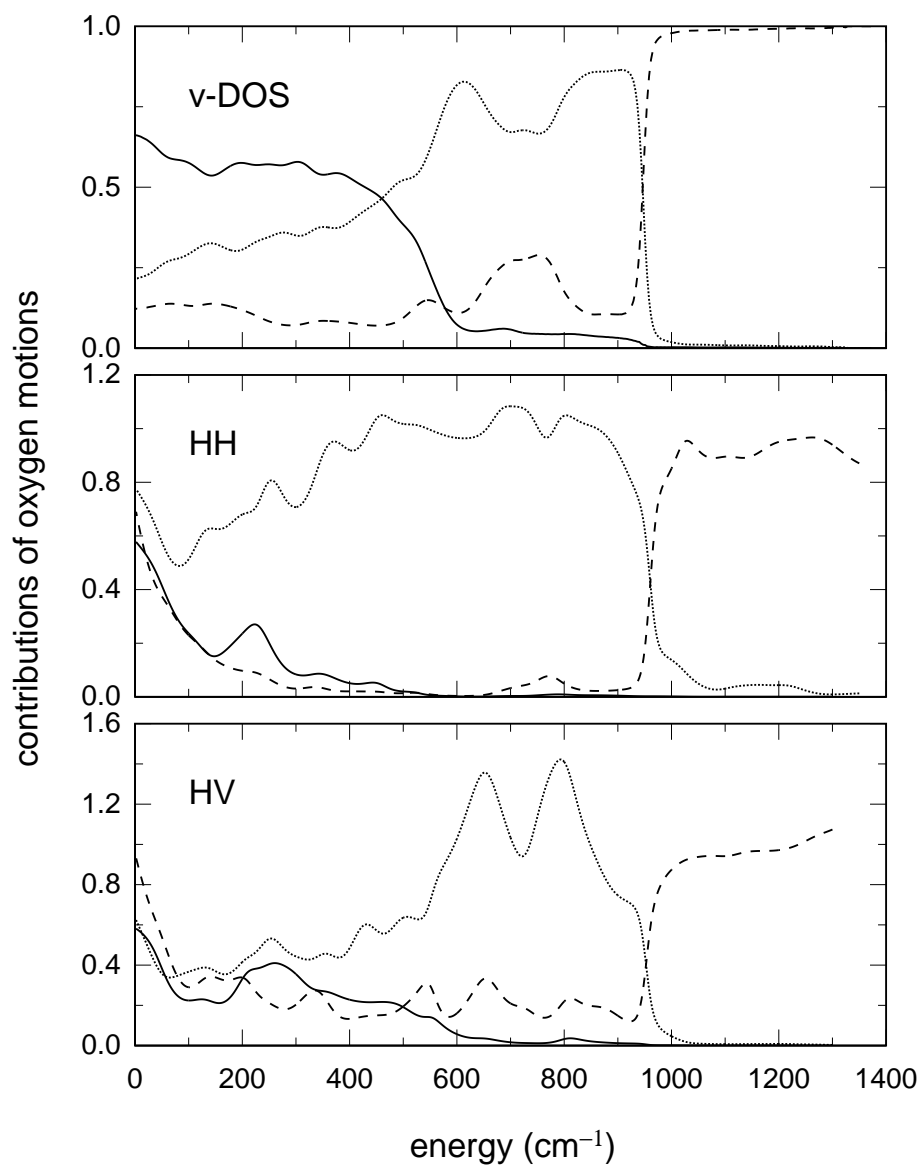


Figure 4.4: Contributions to the vibrational density of states [22], and to the HH and HV Raman spectra from oxygen vibrations decomposed according to rocking (solid), bending (dotted), and stretching (dashed) vibrations. The contributions are expressed as ratios with respect to the total oxygen contribution.

frequency part of the spectra ( $> \sim 1000 \text{ cm}^{-1}$ ) almost exclusively results from stretching vibrations. As far as the HH spectrum is concerned, the decomposition indicates that the bending motions dominate the rest of the spectrum. In particular, the contribution of rocking vibrations is suppressed with respect to their weight in the vibrational density of states. The decomposition of the HV Raman spectrum again shows the closest resemblance with the vibrational density of states. The rocking component is found to be smaller than in the vibrational density of states, but larger than in the HH Raman spectrum.



## Chapter 5

# Application to v-B<sub>2</sub>O<sub>3</sub>

This chapter is devoted to a comprehensive study of the structural and vibrational properties of vitreous boron trioxide (v-B<sub>2</sub>O<sub>3</sub>). For a large model structure, obtained by first-principles molecular dynamics, we calculated the neutron static structure factor, and the infrared and Raman spectra. The Raman susceptibilities and the infrared couplings are calculated by means of the finite field approach introduced in Chapter 3. The accurate description of the Raman susceptibilities and of the vibrational modes provides us with a way to derive an estimate for the concentration of boroxol rings embedded in the glass network from the *experimental* Raman spectrum.

### 5.1 The structure

We consider a model structure of v-B<sub>2</sub>O<sub>3</sub> previously obtained by A. Pasquarello using a Car-Parrinello molecular dynamics approach. A 160-atom model of the high-pressure B<sub>2</sub>O<sub>3</sub>-II crystalline polymorph [96] was first strained to fit a cubic unit cell in order to obtain the experimental density of the glass (1.84 g/cm<sup>-3</sup>). Then, the system was melted and equilibrated at 2500 K. A rapid quench to low temperatures yielded the present structure. Ultrasoft pseudopotentials were used for the boron and the oxygen atoms. The electronic wave functions and the charge density were described by plane wave basis sets with cutoffs of 24 and 250 Ry, respectively. The Brillouin zone was sampled at the sole

$\Gamma$  point. A generalized gradient approximation was adopted to describe the exchange and correlation energy [98].

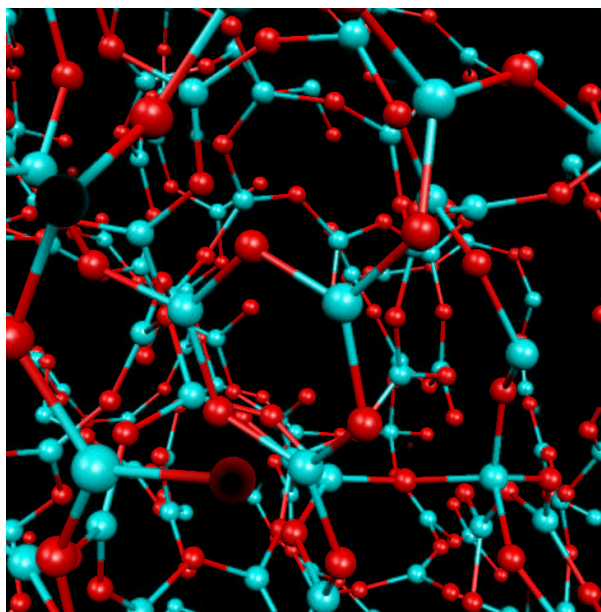


Figure 5.1: Ball and stick model of the model structure of  $v\text{-B}_2\text{O}_3$  investigated here. On the forefront a boroxol ( $\text{B}_3\text{O}_3$ ) ring is clearly visible.

The model structure consists of a regular network of cornersharing  $\text{BO}_3$  units, apart from a single boron atom which is fourfold coordinated and from a single oxygen atom which is threefold coordinated. The average B-O bond length is 2.60 bohr with a rms deviation of 0.05 bohr, in excellent agreement with the experimental value of 2.59 bohr from neutron diffraction [97]. Without considering the fourfold coordinated boron atom, the average O-B-O angle is  $119.96^\circ \pm 3.34^\circ$  in very good agreement with the experimental value of  $120^\circ$ , which corresponds to planar symmetric  $\text{BO}_3$  units. The average B-O-B angle (without considering the threefold coordinated oxygen atom) is of  $133.5^\circ \pm 9.6^\circ$ , which compares well with the experimental angle of  $130^\circ$ .

Two noncontiguous threefold (boroxol) rings are embedded in our model. The average

B-O-B angle in these rings is  $119.71^\circ \pm 0.46^\circ$ . The small deviation in the bond angles for the boroxol rings suggests a high structural regularity in these rings. The degree of planarity can be investigated by considering the sum of all the bond angles in the ring, which gives  $720^\circ$  for planar three-fold rings. We find  $717.2^\circ$  and  $718.4^\circ$  for the two boroxol rings in our model. Therefore, the boroxol rings in our model are very regular and almost planar.

Table 5.1: Ring statistics for our model of  $v\text{-B}_2\text{O}_3$ . The values are normalized to 3.

ring size							
3	4	5	6	7	8	9	10
0.095238	0.04761	0.07937	0.3333	0.8730	1.1270	0.4286	0.01587

The connectivity of our model structure can be characterized in terms of rings using the shortest path analysis [2]. For every threefold coordinated boron atom, we considered each of the three different pairs of neighboring oxygen atoms, and determined the shortest path connecting the oxygen atoms in each of the pairs. Closed paths containing  $n$  B-O segments are referred to as  $n$ -fold rings. In Table 5.1, we report the ring statistics for our model. The most frequent rings are the 8-fold rings. In general large rings with 6 to 9 B-O segments are more frequent than small rings. A single fourfold ring is found in the network.

## 5.2 Neutron static structure factor

To assess further the quality of our model structure, we address the neutron static structure factor. In neutron diffraction experiments the scattering function  $S(\mathbf{Q})$  is measured in terms of the exchanged momentum  $\mathbf{Q}$ . For isotropic materials only the magnitude  $Q$  of the momentum is considered. Adopting the harmonic approximation, the structure factor  $S(\mathbf{Q})$  is given by [100]:

$$S(\mathbf{Q}) = \frac{1}{N\langle b^2 \rangle} \sum_{ij} b_i b_j e^{-W_{ij}(\mathbf{Q})} e^{i\mathbf{Q} \cdot (\mathbf{R}_j - \mathbf{R}_i)} \quad (5.1)$$

where the indices  $i$  and  $j$  run over the  $N$  atoms with mass  $M_i$  and position  $\mathbf{R}_i$  in the unit cell. The interactions between the incoming neutrons and the nuclei are described by the neutron scattering lengths  $b_i$ ,

$$\langle b^2 \rangle = \frac{1}{N} \sum_i b_i^2, \quad (5.2)$$

being the average square scattering length. The Debye-Waller factors  $W_{ij}$  are given by:

$$W_{ij}(\mathbf{Q}) = \frac{1}{2} \langle [\mathbf{Q} \cdot (\mathbf{u}_i - \mathbf{u}_j)]^2 \rangle, \quad (5.3)$$

where  $\langle \dots \rangle$  indicates a temporal average and can be obtained by using:

$$\langle u_{i\alpha} u_{j\beta} \rangle = \sum_n \frac{\hbar}{\omega_n} \frac{v_{i\alpha}^n}{\sqrt{M_i}} \frac{v_{j\beta}^n}{\sqrt{M_j}} [n(\hbar\omega_n) + \frac{1}{2}], \quad (5.4)$$

where the index  $n$  runs over the vibrational modes of frequency  $\omega_n$  with corresponding normalized eigenmode  $\mathbf{v}^n$ , the temperature dependence enters through the Boson occupation number, and the greek indices run over the Cartesian directions.

For our model structure of v-B<sub>2</sub>O<sub>3</sub> we obtained the vibrational modes and frequencies by diagonalizing the dynamical matrix (see Sec. 4.1). We calculated the dynamical matrix numerically by taking finite differences of the atomic forces. Each atom was displaced by  $\pm 0.1$  bohr along the three Cartesian directions.

Due to the huge neutron absorption of the isotope <sup>10</sup>B, the samples of v-B<sub>2</sub>O<sub>3</sub> used in neutron scattering experiments generally only contain the isotope <sup>11</sup>B. We used a neutron scattering length of 6.65 fm for the <sup>11</sup>B isotope and of 5.805 fm for the O atom. In our study of the neutron static structure factor, we considered a dynamical matrix in which we used the mass of the <sup>11</sup>B isotope. In Fig. 5.2, we compare the calculated static structure factor  $S(Q)$  with the experimental one from Ref. [14]. Both factors refer to a temperature of 15 K. The good description of the short range order in our model is at the origin of the excellent agreement between calculated and measured structure factors for  $Q \geq 2 \text{ \AA}^{-1}$ . The good agreement for both the intensity and the position of the first sharp diffraction peak at  $Q_{\text{FSDP}} = 1.6 \text{ \AA}^{-1}$  indicates that also the intermediate range order is well reproduced in our model structure.



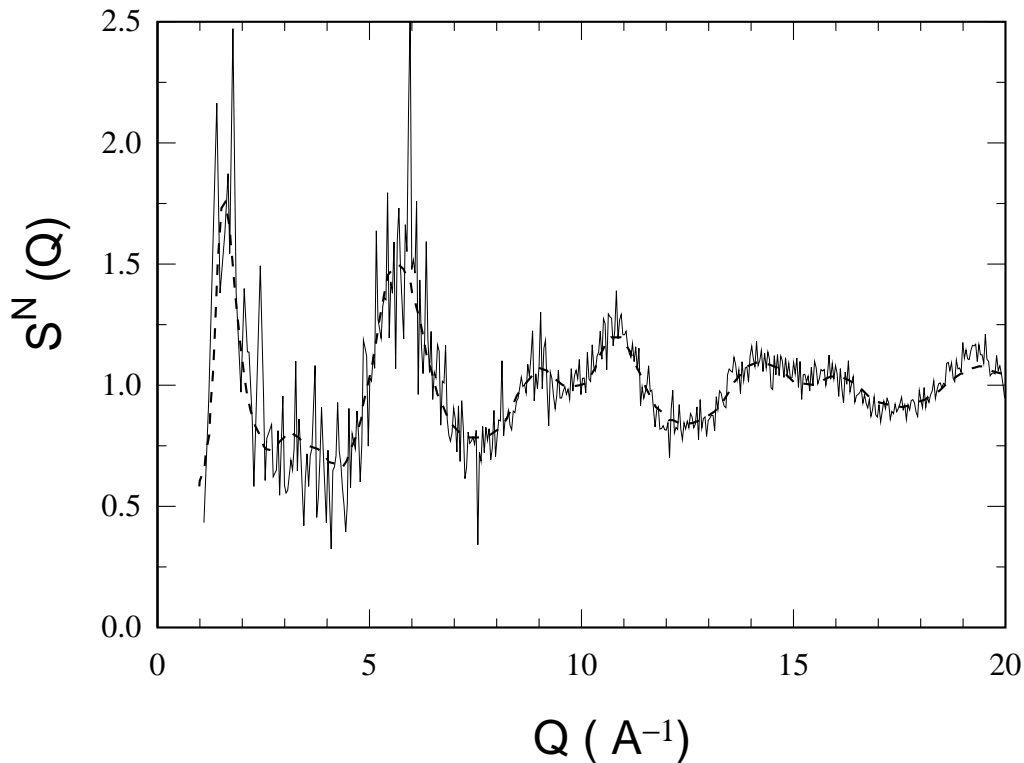


Figure 5.2: Neutron static structure calculated (solid) and measured (dashed) [14] at a temperature of 15 K.

### 5.3 Vibrational density of states

We analyzed the vibrational density of states by considering the vibrational frequencies and modes obtained as described in the previous section. Here, we took the mass of the boron atom according to its natural abundance.

In Fig. 5.3, we report the calculated vibrational density of states together with the decomposition into a component due to oxygen vibrations and a component due to boron vibrations, as done for vitreous silica in Sec. 4.2.4. Three main features are present in the vibrational density of states: a low frequency peak at  $\sim 100 \text{ cm}^{-1}$ , a central peak at  $\sim 650 \text{ cm}^{-1}$ , and, in the high frequency part of the spectrum, a doublet at  $\sim 1300\text{-}1450 \text{ cm}^{-1}$ . Note that there is a region with relatively few vibrational modes between  $\sim 800$  and  $\sim 1000$

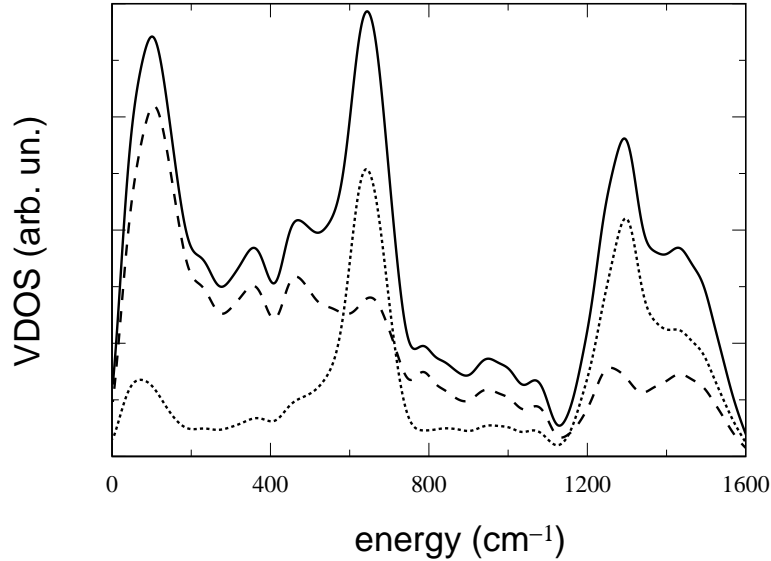


Figure 5.3: Vibrational density of states (solid) and its component due to oxygen (dashed), and boron motions (dotted). A gaussian broadening of  $22 \text{ cm}^{-1}$  was applied.

$\text{cm}^{-1}$ . The low frequency peak is mainly given by oxygen motions. On the contrary, the boron vibrations are prevalent in the high frequency feature. The peak at  $\sim 650 \text{ cm}^{-1}$  also presents a strong contribution from boron motions.

The motion of each oxygen atom can be further decomposed according to its first neighbor configuration, as done in Ref. [101] for vitreous silica. We call *bending* the motion along the direction of the bisector of the B-O-B angle. The motion along a direction orthogonal to the plane described by the oxygen atom and its two neighboring boron atoms is referred to as *rocking*. The motion along a third direction orthogonal to the other two is named *stretching*. In Fig. 5.4, we show the decomposition of the oxygen contribution to the vibrational density of states into rocking, bending and stretching components. The rocking motions are prevalent in the low frequency peak. The stretching motions are dominant in the high frequency feature. In the rest of the spectrum all three components contribute to the vibrational modes, with a larger participation of the bending motions.

In a similar way, we decomposed the boron vibrations. Because of the particular first neighbor configuration, we can only distinguish the direction perpendicular to the *ideal*

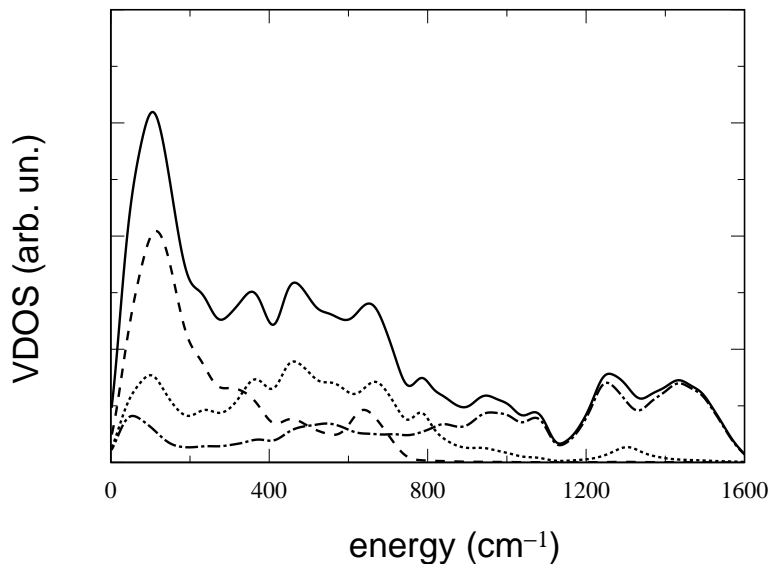


Figure 5.4: Decomposition of the oxygen contribution (solid) to the vibrational density of states in rocking (dashed), bending (dotted), and stretching (dot dashed) components. A gaussian broadening of  $22 \text{ cm}^{-1}$  was applied.

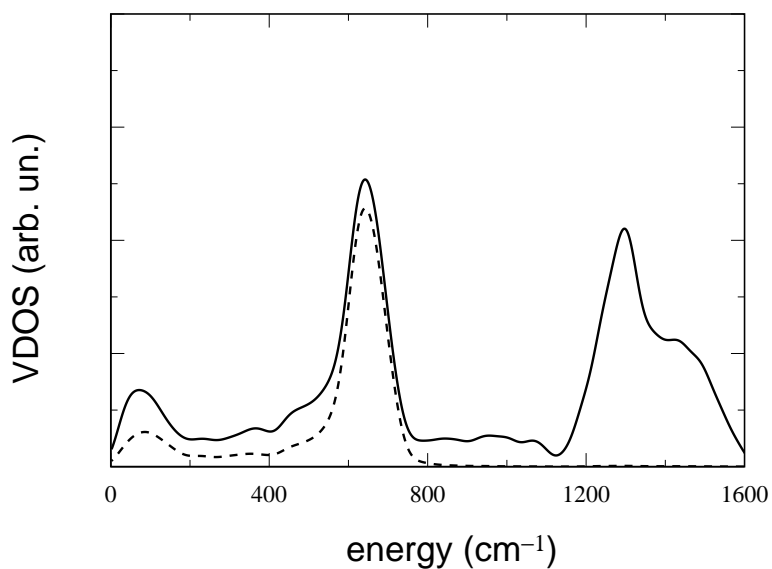


Figure 5.5: Boron contribution (solid) to the vibrational density of states and the component due to rocking motions of boron atoms (dashed). A gaussian broadening of  $22 \text{ cm}^{-1}$  was applied.

BO<sub>3</sub> planes, defined by the three oxygen atoms neighboring each boron atom. Motions along this directions are referred to as *rocking*. In Fig. 5.5, we show that the peak at  $\sim 650 \text{ cm}^{-1}$  is mainly given by rocking motions of the boron atoms.

## 5.4 Infrared spectrum

Following the approach introduced in Section 3.3, we calculated the high-frequency dielectric tensors and the effective charges by taking finite differences of the electric polarization and of the atomic forces, respectively. We used electric fields of  $\pm 0.001$  a.u. along the three Cartesian directions. By averaging over the three Cartesian directions, we found a value of 2.10 for the high-frequency dielectric constant  $\epsilon_\infty$ , in good agreement with the experimental value of 2.19 [102]. We can now calculate the dielectric response function in the long wavelength limit [103]. The real part of the dielectric response function reads:

$$\epsilon_1(\omega) = \epsilon_\infty + \frac{4\pi}{3\Omega} \sum_n \frac{|\mathbf{F}^n|^2}{\omega^2 - \omega_n^2}. \quad (5.5)$$

In Eq. (5.5), the oscillator strengths  $\mathbf{F}^n$  are given by:

$$F_k^n = \sum_{\alpha,i} Z_{\alpha,ik}^* u_{\alpha,i}^n, \quad (5.6)$$

where we adopted the notation introduced in Sec.4.1.1.

In Figure 5.6 we report the calculated and measured [102] real part of the dielectric constant  $\epsilon_1(\omega)$ . We find a good agreement with respect to experiment both for the positions of the two peaks at  $\sim 1200 \text{ cm}^{-1}$  and  $\sim 700 \text{ cm}^{-1}$  and for their relative intensities. The imaginary part  $\epsilon_2(\omega)$  of the dielectric constant in the infrared is given by [103]:

$$\epsilon_2(\omega) = \frac{4\pi^2}{3\Omega} \sum_n \frac{|\mathbf{F}^n|^2}{2\omega_n} \delta(\omega - \omega_n). \quad (5.7)$$

In Figure 5.7 we report the calculated and experimental [102]  $\epsilon_2(\omega)$ . As for the  $\epsilon_1$ , the imaginary part of the dielectric constant  $\epsilon_2$  shows a good agreement with experiment for the positions of the peaks at  $\sim 700 \text{ cm}^{-1}$  and  $\sim 1250 \text{ cm}^{-1}$  and for their relative intensities.

Along the lines of the experimental work in Ref. [103], we obtained the energy loss function in the infrared  $-\text{Im}[1/\epsilon(\omega)]$ . We proceeded in this way: first, we obtained from

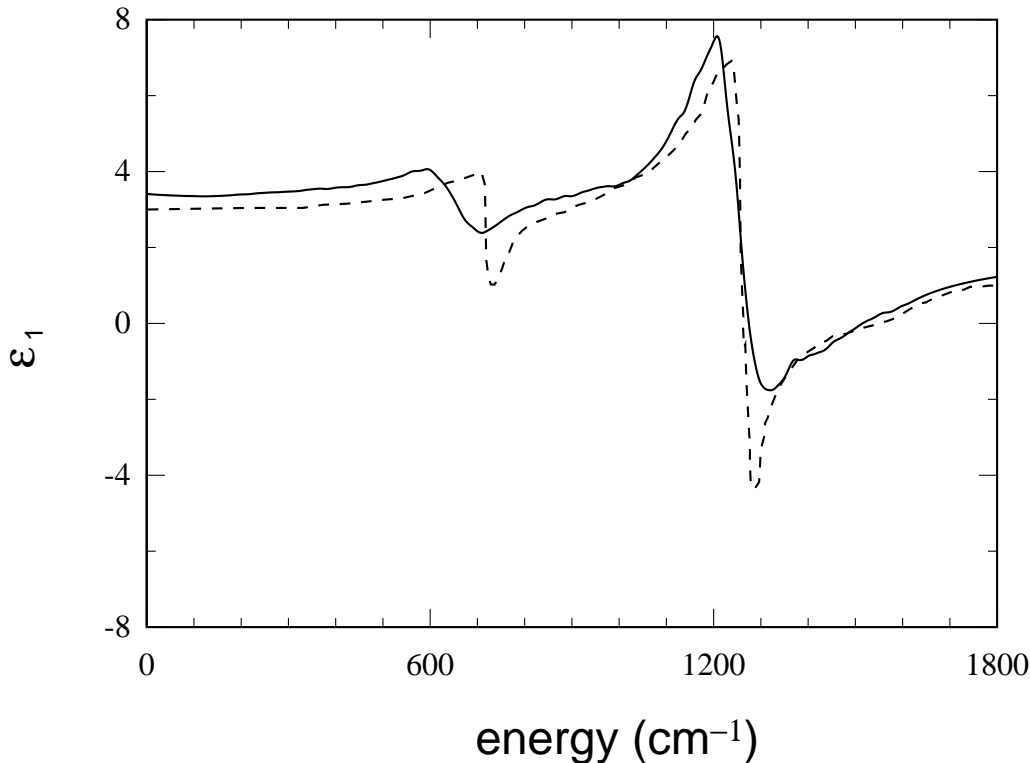


Figure 5.6: Real part of the infrared dielectric constant (solid). The experimental line (dashed) is taken from Ref. [102]. A Lorentzian broadening of  $0.0025 \text{ cm}^{-2}$  was applied.

Eq. (4.1) the longitudinal modes  $w_{\alpha,i}^{n,l}$  and frequencies  $w^{n,l}$  for the three Cartesian directions  $l$ ; then we applied the formula [103]:

$$-\text{Im}[1/\epsilon(\omega)] = \frac{1}{3} \sum_l \left[ \frac{4\pi^2}{\Omega \epsilon_\infty^{l2}} \sum_n \frac{(F_l^{n,l})^2}{2\omega_n} \delta(\omega - \omega_n) \right], \quad (5.8)$$

where the oscillator strengths  $\mathbf{F}^{n,l}$  are calculated from (5.6) by considering the vibrational modes relative to the direction  $l$ , and  $\epsilon_\infty^l$  is the calculated high-frequency dielectric constant along  $l$ . As for  $\epsilon_1$  and  $\epsilon_2$ , the energy loss function is in good agreement with the experimental one. The LO-TO splittings for the two main features occurring in the  $\epsilon_2(\omega)$  are defined as the separations with the analogous features in the energy loss function. We found a LO-TO splitting of  $22 \text{ cm}^{-1}$  for the low frequency peak and of  $318 \text{ cm}^{-1}$  for the

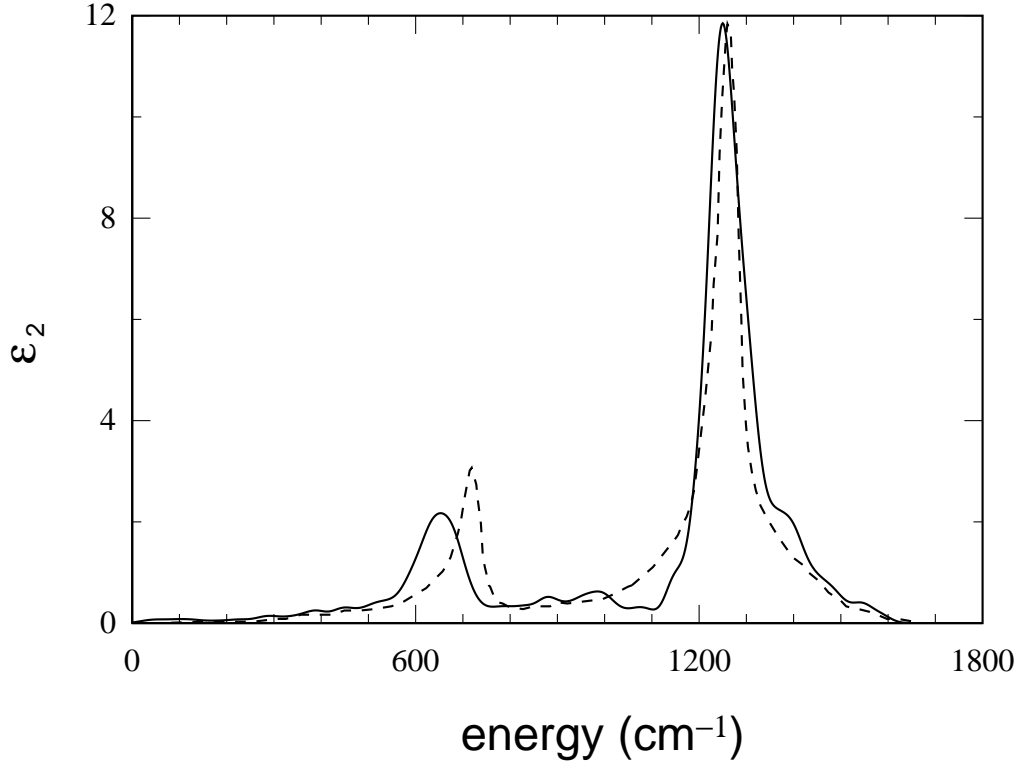


Figure 5.7: Imaginary part of the infrared dielectric constant (solid). The experimental line (dashed) is taken from Ref. [102]. A gaussian broadening of  $20 \text{ cm}^{-1}$  was applied.

high frequency peak, in good agreement with the experimental values of  $20 \text{ cm}^{-1}$  and  $290 \text{ cm}^{-1}$ , respectively.

## 5.5 Raman spectrum

The key ingredients for calculating the Raman spectrum are the derivatives  $\partial\chi_{ij}/\partial r_{\alpha k}$  of the dielectric susceptibility tensor with respect to the atomic displacements, as reported in Sec. 4.1.1. These third-rank tensors correspond to third order derivatives of the energy [24]:

$$\frac{\partial\chi_{ij}}{\partial r_{\alpha k}} = -\frac{4\pi}{\Omega} \left. \frac{\partial^3 E^{\mathcal{E}}}{\partial r_{\alpha k} \partial \mathcal{E}_i \partial \mathcal{E}_j} \right|_{\mathcal{E}=0}. \quad (5.9)$$

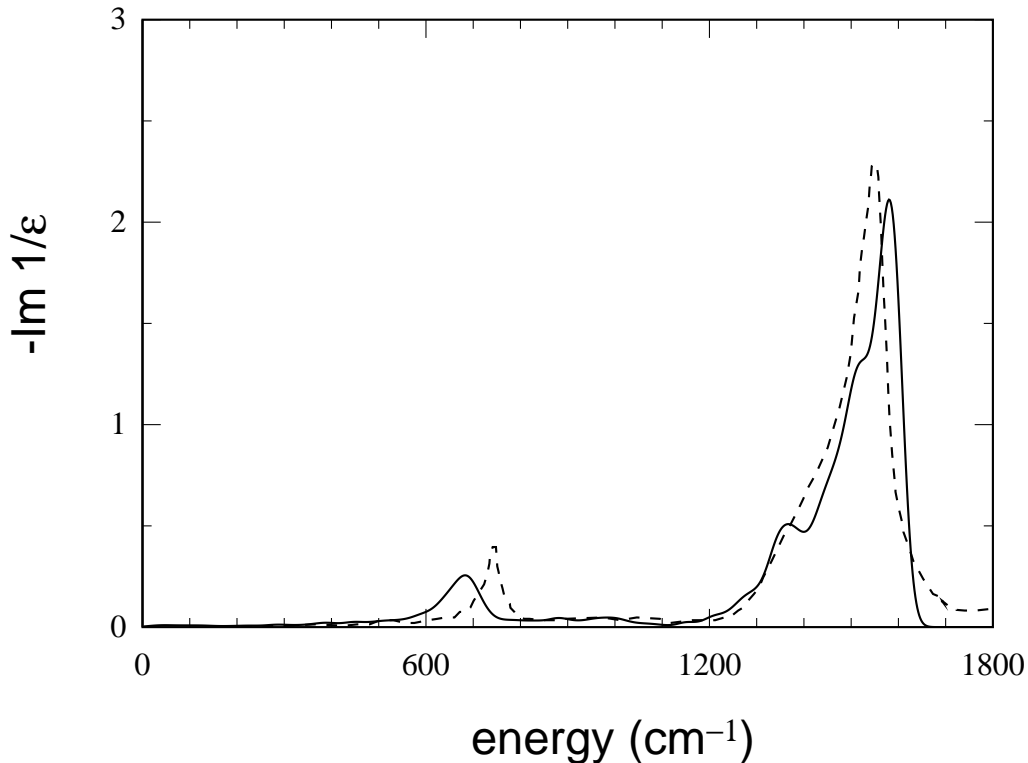


Figure 5.8: Energy loss spectrum in the infrared (solid). The experimental line (dashed) is taken from Ref. [102]. A gaussian broadening of  $20 \text{ cm}^{-1}$  was applied.

In Section 4.2.2, we calculated these tensors by taking finite differences of dielectric susceptibility tensors. This implies the selfconsistent computation of  $6N$  dielectric tensors, where  $N$  is the number of atoms in the unit cell. By using the finite field method introduced in Chapter 3, it is possible to calculate the same third rank tensors with considerably less computational effort, particularly in the case of a system with large  $N$ . In Eq. (5.9) we can write the derivatives  $\partial E^\mathcal{E} / \partial r_{\alpha k}$  as the atomic forces  $F_{r_{\alpha k}}^\mathcal{E}$  in the presence of an electric field  $\mathcal{E}$ :

$$\frac{\partial \chi_{ij}}{\partial r_{\alpha k}} = -\frac{4\pi}{\Omega} \left. \frac{\partial^2 F_{r_{\alpha k}}^\mathcal{E}}{\partial \mathcal{E}_i \partial \mathcal{E}_j} \right|_{\mathcal{E}=0}. \quad (5.10)$$

Hence, we can easily calculate the tensors  $\partial \chi_{ij} / \partial r_{\alpha k}$  by taking finite differences of the atomic forces. We obtained the diagonal terms  $\partial \chi_{ii} / \partial r_{\alpha k}$ , by considering values for the

electric field of  $\pm 0.001$  and  $\pm 0.0005$  a.u., and using the following formula for second order numerical derivatives:

$$\frac{d^2 f}{dx^2}(0) \simeq \frac{1}{12h^2} \left[ -f(-2h) + 16f(-h) - 30f(0) + 16f(h) - f(2h) \right]. \quad (5.11)$$

The Taylor development of  $F^\mathcal{E}$  offers a way to access the off-diagonal ( $i \neq j$ ) terms of  $\partial\chi_{ij}/\partial r_{\alpha k}$ :

$$F(\mathcal{E}_i, \mathcal{E}_j) = F(0, 0) + \left. \frac{\partial F}{\partial \mathcal{E}_i} \right|_0 \mathcal{E}_i + \left. \frac{\partial F}{\partial \mathcal{E}_j} \right|_0 \mathcal{E}_j + \frac{1}{2} \left. \frac{\partial^2 F}{\partial \mathcal{E}_i^2} \right|_0 \mathcal{E}_i^2 + \frac{1}{2} \left. \frac{\partial^2 F}{\partial \mathcal{E}_j^2} \right|_0 \mathcal{E}_j^2 + \left. \frac{\partial^2 F}{\partial \mathcal{E}_i \partial \mathcal{E}_j} \right|_0 \mathcal{E}_i \mathcal{E}_j + \dots \quad (5.12)$$

By defining a  $\mathcal{E}_i = \lambda$  and  $\mathcal{E}_j = \lambda$ , the mixed term  $\partial^2 F / \partial \mathcal{E}_i \partial \mathcal{E}_j$  is given by:

$$\left. \frac{\partial^2 F}{\partial \mathcal{E}_i \partial \mathcal{E}_j} \right|_0 = \frac{1}{2} \left. \frac{\partial^2 F}{\partial \lambda^2} \right|_0 - \frac{1}{2} \left. \frac{\partial^2 F}{\partial \mathcal{E}_i^2} \right|_0 - \frac{1}{2} \left. \frac{\partial^2 F}{\partial \mathcal{E}_j^2} \right|_0. \quad (5.13)$$

Therefore, we implemented in our code for the treatment of finite electric fields the possibility of applying simultaneously fields along two different Cartesian directions. We applied electric fields of intensity  $\pm 0.00035$  and  $\pm 0.0007$  a.u. along the three different couples of Cartesian directions, and used formula (5.11) for computing the derivative  $\partial^2 F / \partial \lambda^2$ . In this way, we could obtain all the tensors  $\partial\chi_{ij}/\partial r_{\alpha k}$  by 25 selfconsistent minimizations of the electric-field dependent energy functional. The numerical accuracy of the calculated tensors was verified *a posteriori* by noting no significant variation in the calculated Raman spectra when adopting the formula for  $d^2 f(x)/dx^2$  with only three points.

The Raman spectra were then obtained by using the procedure described in Section 4.2.2. In Figure 5.9 we show the calculated reduced HH and HV polarized Raman spectra together with the experimental spectra from Ref. [102]. The calculated spectra were scaled by a same factor, which was determined by matching the areas under the theoretical and experimental HH curves.

Although the differences between the intensities of the theoretical peaks with the corresponding experimental peaks are considerable, the theoretical spectra present most of the features appearing in the experimental ones. In particular both the HH and the HV spectra present a gap ranging from  $\sim 850$  to  $\sim 1200$   $\text{cm}^{-1}$ , and a boson peak at  $\sim 100$   $\text{cm}^{-1}$ . The calculated HH spectrum shows three peaks in the medium energy region at



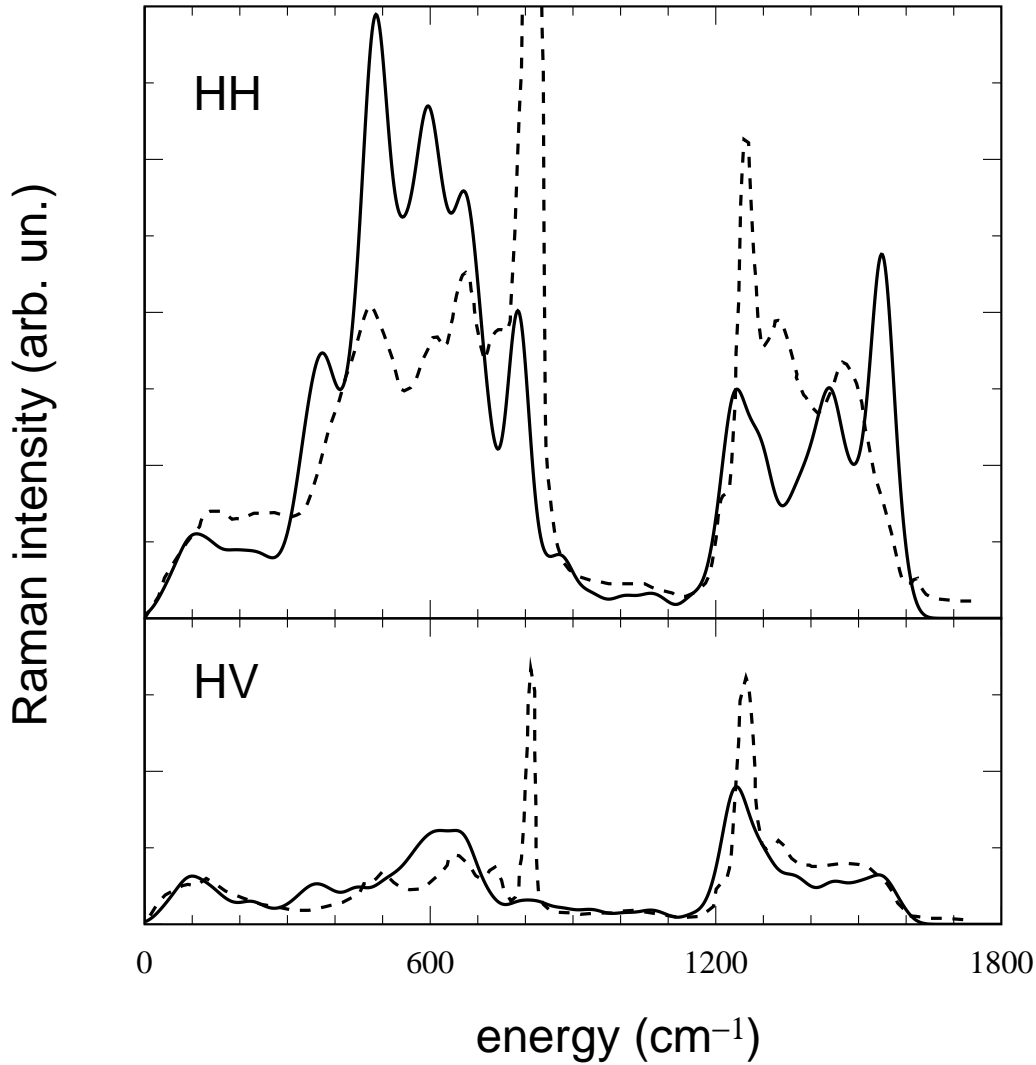


Figure 5.9: HH polarized and HV polarized reduced Raman spectrum (solid). A gaussian broadening of  $22 \text{ cm}^{-1}$  was used. The experimental lines (dashed) are taken from Ref. [102].

$482$ ,  $596$ , and  $662 \text{ cm}^{-1}$ , in correspondence to three peaks in the experimental spectrum at  $470$ ,  $610$  and  $670 \text{ cm}^{-1}$ . We find a peak at  $784 \text{ cm}^{-1}$  in the theoretical HH spectrum which corresponds to the experimental boroxol peak at  $808 \text{ cm}^{-1}$ . The integrated intensity of this feature is remarkably lower than the experimental integrated intensity. In the

high frequency region we find three peaks at 1242, 1436, and 1548 cm<sup>-1</sup> in the calculated HH spectrum. In the experimental spectrum, there are also three main peaks in the high frequency region, at 1260, 1325 and 1475 cm<sup>-1</sup>.

In the medium energy region of the HV spectrum we note three features at 498, 598, and 656 cm<sup>-1</sup>, while, in the experimental spectrum, three features are found at 500, 655, 740 cm<sup>-1</sup>. A peak corresponding to the experimental boroxol peak at 808 cm<sup>-1</sup>, is found in the calculated HV spectrum at 788 cm<sup>-1</sup>. As for the HH spectrum, the integrated intensity of this peak is significantly underestimated. The high frequency part of the calculated spectrum shows a peak at 1242 cm<sup>-1</sup> followed by a *plateau* up to  $\sim 1600$  cm<sup>-1</sup>. Similarly, in the experimental spectrum, we find a peak at 1260 cm<sup>-1</sup> followed by a *plateau* up to  $\sim 1550$  cm<sup>-1</sup>.

As observed in Chapter 4, the Raman spectrum of oxide glasses depends strongly on the intermediate range order. We attribute the nonimpressive agreement between the theoretical and experimental Raman spectrum to an inaccurate description of the intermediate-range structural properties in our model. This should be contrasted with the excellent agreement between theory and experiment for the neutron static structure factor and the infrared dielectric response, which mainly result from an accurate description of the short-range order in our model. Nevertheless, the overall good correspondence for the positions of the peaks in the HH and HV Raman spectra supports the validity of the theoretical description for understanding the origin of the experimental features.

To investigate the respective roles of oxygen and boron atoms in the Raman spectra, we obtain partial spectra by considering only one atomic species in the sum over  $\alpha$  in Eq. (4.9). Unlike for the vibrational density of states, the sum of the partial Raman spectra does not recover the full spectrum, because of interference terms. In Figure 5.10, we report the decomposition of the HH spectrum in contributions from oxygen and boron vibrations. At low and medium energies the Raman spectrum mainly results from the oxygen contribution. In this frequency region, the boron vibrations give rise to a significant peak at  $\sim 650$  cm<sup>-1</sup>. In the high frequency part of the spectrum the boron contribution prevails over the oxygen one.

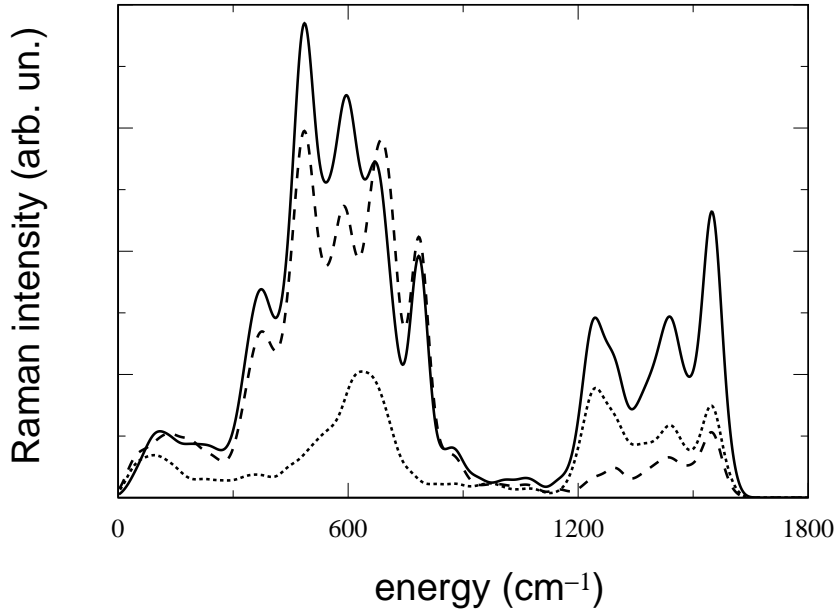


Figure 5.10: Partial contributions to the HH polarized reduced Raman spectrum (solid), from oxygen vibrations (dashed) and boron vibrations (dotted). A gaussian broadening of  $22 \text{ cm}^{-1}$  was used.

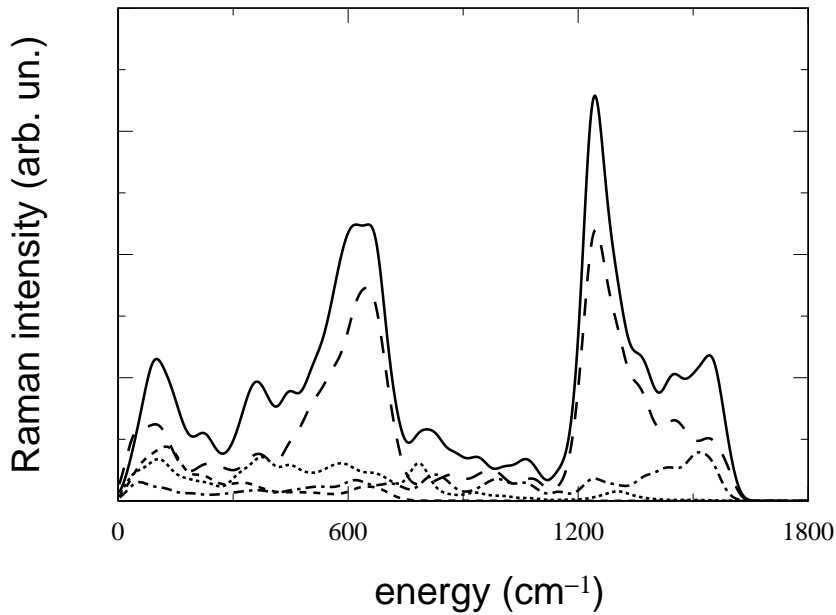


Figure 5.11: Partial contributions to the HV polarized reduced Raman spectrum (solid), from oxygen vibrations (dashed) and boron vibrations (dotted). A gaussian broadening of  $22 \text{ cm}^{-1}$  was used.

In Figure 5.11, we show the decomposition of the HV spectrum in contributions from oxygen and boron vibrations. The relative participations of oxygen and boron vibrations to the full spectrum is similar to what we found for the HH spectrum. However, the boron contribution is overall more relevant in this case. The presence of a strong contribution from boron vibrations, also in the middle energy part of the HH and HV spectra, should be contrasted with the decompositions of the Raman spectra for vitreous silica in Sec. 4.2.4, in which the contribution from silicon vibrations is always small.

We further decomposed the contributions of oxygen and boron vibrations to the Raman spectra according to the local environment of each oxygen and boron atom, as done in the previous section. For the oxygen atoms, we separately considered rocking, bending and stretching directions. For the boron atoms, we only considered the vibrations along the rocking directions. The miscoordinated atoms were not taken into account in the calculation of partial contributions.

In Figure 5.12, the oxygen contributions to the HH spectrum from rocking, bending, and stretching vibrations are reported together with the boron contribution from rocking vibrations. The contribution from oxygen vibrations along the bending directions is dominant up to  $\sim 850 \text{ cm}^{-1}$ . Around  $650 \text{ cm}^{-1}$  a strong contribution is given by the rocking vibrations of boron atoms. The lack of relevant partial contributions to the high frequency part of the spectrum indicates that in this energy region the spectrum mainly arises from boron vibrations in planes perpendicular to the rocking directions.

In Figure 5.13, the oxygen contributions to the HV spectrum from rocking, bending, and stretching vibrations are reported together with the boron contribution from rocking vibrations. The relative contributions show, in general, the same behavior as found for the HH spectrum. However, in the energy region around  $\sim 650 \text{ cm}^{-1}$ , the peak due to boron vibrations along rocking directions now dominates the contributions from oxygen bending vibrations.

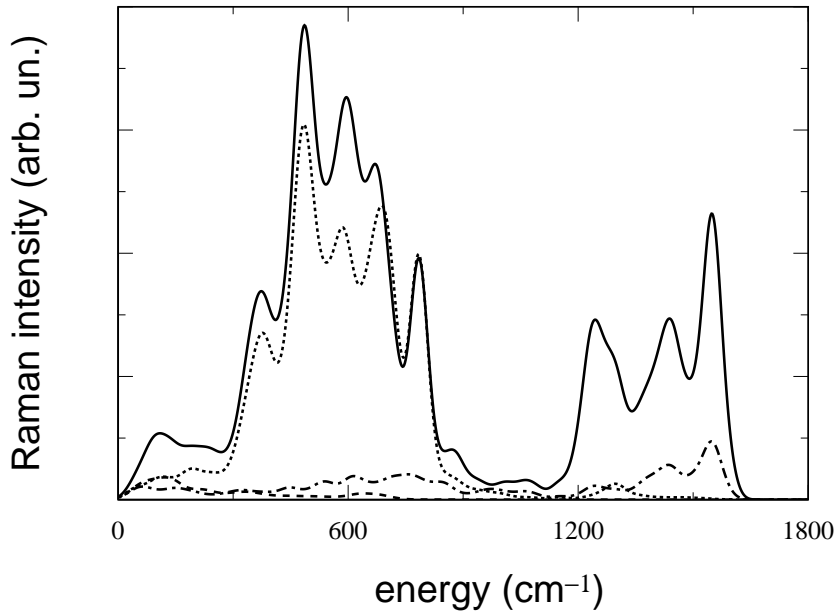


Figure 5.12: Contributions to the HH Raman spectrum (solid) from oxygen vibrations decomposed according to rocking (dashed), bending (dotted), and stretching (dot dashed) vibrations, and from boron vibrations in the rocking directions (long dashed). A gaussian broadening of  $22 \text{ cm}^{-1}$  was used.

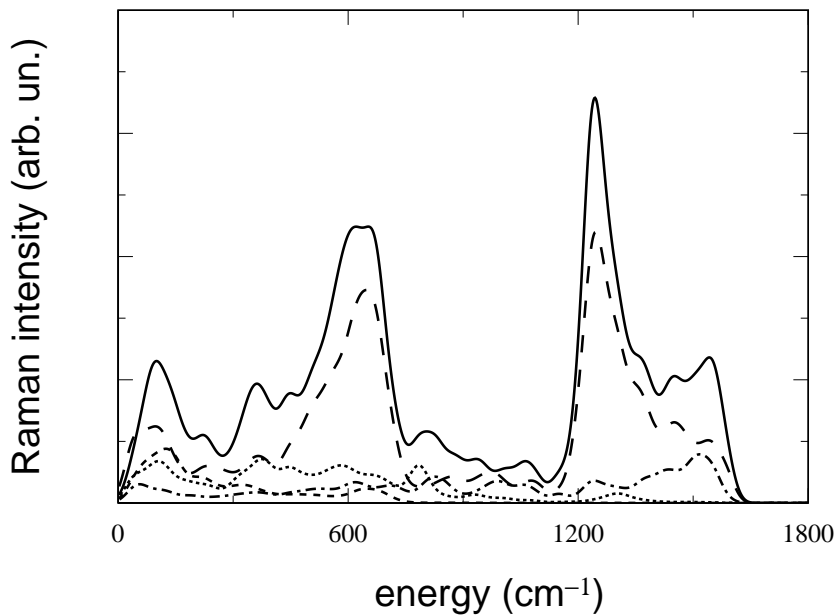


Figure 5.13: Contributions to the HV Raman spectrum (solid) from oxygen vibrations decomposed according to rocking (dashed), bending (dotted), and stretching (dot dashed) vibrations, and from boron vibrations in the rocking directions (long dashed). A gaussian broadening of  $22 \text{ cm}^{-1}$  was used.

## 5.6 Concentration of boroxol rings

In our model, the lines at  $784\text{ cm}^{-1}$  in the HH spectrum and at  $788\text{ cm}^{-1}$  in the HV one correspond to the in-phase breathing motion of oxygen atoms in boroxol rings. In Figures 5.14 and 5.15, we report the contribution to the HH and HV spectra due to the vibrations of oxygen atoms in boroxol rings moving towards the center of the *ideal* triangles described by these atoms. These contributions give rise to well defined peaks centered at  $784\text{ cm}^{-1}$ , in good correspondence with the experimental boroxol peaks at  $808\text{ cm}^{-1}$ . The experimental assignment of the line at  $808\text{ cm}^{-1}$  to in-phase breathing motions of oxygen atoms in boroxol rings was obtained in Ref. [9] by analysing the position of this feature in isotopically substituted  $v\text{-B}_2\text{O}_3$  samples. In particular, in a sample of  $v\text{-}^{11}\text{B}_2\text{O}_3$  the position of the boroxol peak was experimentally found to be shifted by  $48\text{ cm}^{-1}$  with respect to a vitreous sample with B isotopes according to the natural abundances. We obtained this shift for our model by calculating the vibrational frequencies and modes using the mass of the boron isotope  $^{11}\text{B}$ . We found a shift of the boroxol peak of  $42\text{ cm}^{-1}$  in good agreement with the experimental value. The ratio of the integrated intensities of the boroxol peaks in the HH and HV spectra corresponds to the depolarization ratio. We found a depolarization ratio of 0.05, to be compared with the experimental values of 0.04 found in Ref. [102] and of 0.07 in Ref. [104].

In our model the total integrated contribution to the HH spectrum from oxygen atoms in boroxol rings is only  $\sim 10\%$  larger than the integrated contribution from these atoms due to the in-phase breathing motions which are responsible for the boroxol peak. Hence, it is in principle possible to estimate the concentration of boroxol rings with arguments analogous to those in Sec. 4.2.3. Quantitative experimental data for the integrated Raman intensities of  $v\text{-B}_2\text{O}_3$  are only available for the polarized spectrum  $I_{\text{Pol}}$  [104]:

$$I_{\text{Pol}}(\omega) = I_{\text{HH}}(\omega) - \frac{4}{3}I_{\text{HV}}(\omega). \quad (5.14)$$

Therefore, we focused on the polarized Raman spectrum. In Figure 5.16, we show that in the frequency region up to the boroxol peak, the polarized spectrum mainly arises from oxygen bending vibrations and boron rocking vibrations. Moreover, the contribution from

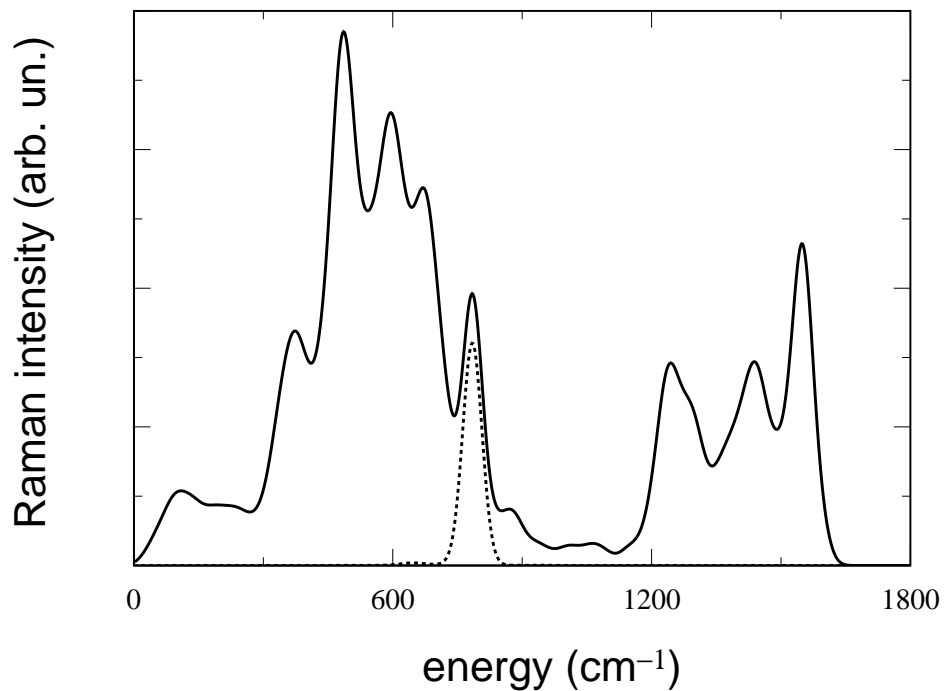


Figure 5.14: Contribution from in-phase *breathing* vibrations of oxygen atoms in boroxol rings (dashed), compared to the total HH intensity (solid). A gaussian broadening of  $22 \text{ cm}^{-1}$  was used.

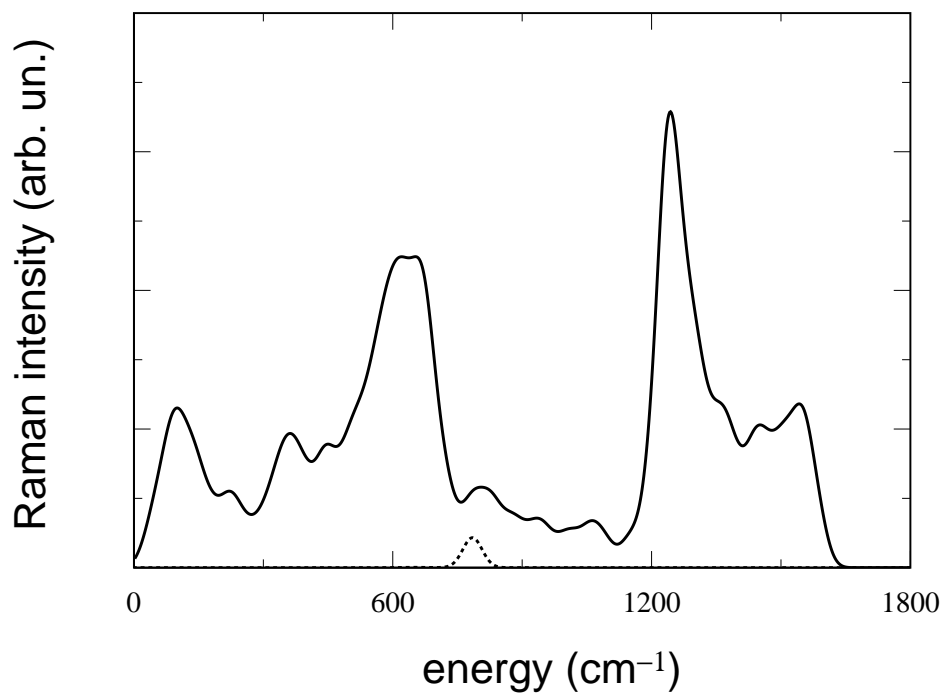


Figure 5.15: Contribution from in-phase *breathing* vibrations of oxygen atoms in boroxol rings (dashed), compared to the total HV intensity (solid). A gaussian broadening of  $22 \text{ cm}^{-1}$  was used.

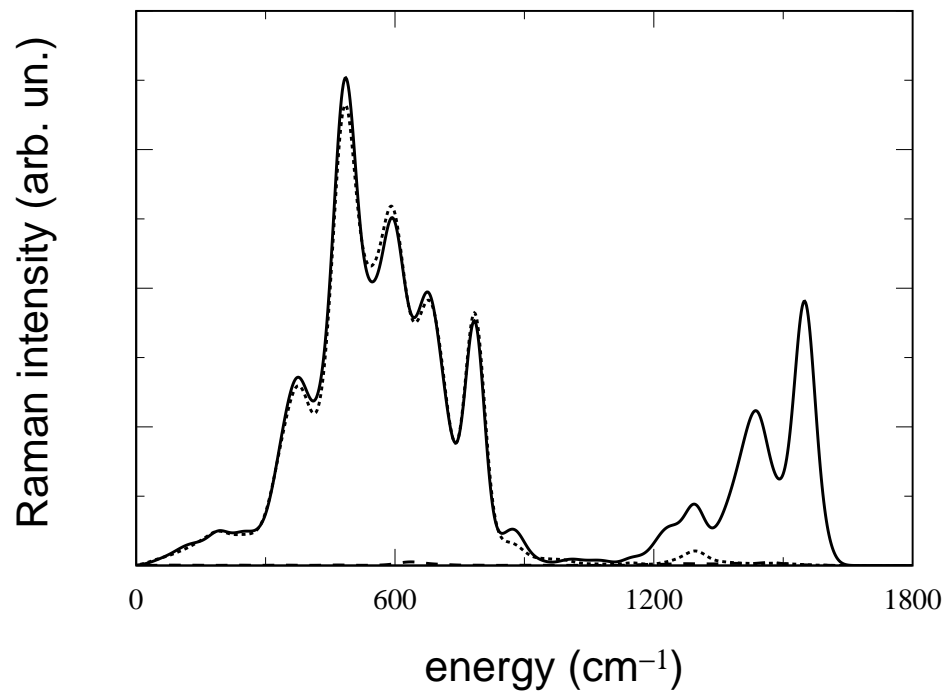


Figure 5.16: Calculated polarized Raman spectrum of  $v\text{-B}_2\text{O}_3$  (solid); contribution from oxygen bending vibrations and boron rocking vibrations (dotted), contribution from boron atoms in boroxol rings (dashed). A gaussian broadening of  $22 \text{ cm}^{-1}$  was used.



these vibrations is negligible at frequencies higher than that of the boroxol peak. We also note that the contribution due to boron atoms in boroxol rings is negligible over the whole spectrum. Hence, we consider the integrated Raman intensity  $I_{\text{Pol}}$  up to the boroxol peak and the integrated Raman intensity of the boroxol peak to be proportional to the number of oxygen atoms not belonging and belonging to boroxol rings, respectively. Hence, it is possible to express the ratio between the number of oxygen atoms in boroxol rings and the number of oxygen atoms outside of these rings, as a function of the integrated intensities of the boroxol peak and of the polarized spectrum up to the boroxol peak:

$$\frac{\#O_3}{\#O_{\text{tot}} - \#O_3} = f' \frac{I_{\text{peak}}}{I_{\text{contour}}}, \quad (5.15)$$

where  $\#O_3$  is the number of oxygen atoms belonging to boroxol rings,  $\#O_{\text{tot}}$  is the total number of oxygen atoms,  $I_{\text{peak}}$  is the integrated intensity of the boroxol peak, and  $I_{\text{contour}}$  is the integrated intensity of the polarized spectrum up to the boroxol peak. By obtaining  $f'$  from our model, we can estimate from the experimental polarized Raman spectrum the concentration of oxygen (boron) atoms in boroxol rings from Eq. (5.15).

We calculated  $I_{\text{peak}}$  by integrating the Raman contribution corresponding to the breathing motion of oxygen atoms in boroxol rings (see Fig. 5.14). In the available experimental data the intensity  $I_{\text{contour}}^{\text{exp}}$  is integrated starting from  $300 \text{ cm}^{-1}$ . Therefore, we integrated the polarized Raman spectrum from  $300 \text{ cm}^{-1}$  to  $850 \text{ cm}^{-1}$  and then subtracted the contribution  $I_{\text{peak}}$  to obtain  $I_{\text{contour}}$ .

We obtained a value of 0.59 for the factor  $f'$ . From the experimental ratio  $I_{\text{peak}}^{\text{exp}}/I_{\text{contour}}^{\text{exp}}$  (0.64) [104], we could estimate a concentration of 27% of oxygen atoms belonging to boroxol rings, which corresponds to a value of 40% for the concentration of boron atom atoms in these rings.



## Chapter 6

# Conclusions

In this thesis we described two new general methods to calculate from first-principles Raman spectra of large model structures. The first method concerns the extension of the perturbative variational approach for the calculation of dielectric tensors to the case of ultrasoft pseudopotentials, allowing a significant improvement in the size of the affordable systems. With the second method, we introduced a general scheme to treat finite electric fields in Car-Parrinello molecular dynamics simulations with periodic boundary conditions. In particular, in the case of large systems, the latter approach gives a further significant reduction of the computational effort required to obtain Raman spectra. This improvement allows one to further increase the size of affordable systems.

These methods were applied to the study of vitreous silica and vitreous boron oxide. First, the quality of the Raman spectra calculated by first-principles was assessed by investigating the Raman activities in  $\alpha$ -quartz. The good agreement with experiment supports the use of first-principles approaches. By applying our perturbative approach, based on ultrasoft pseudopotentials, we could obtain the Raman spectrum for a model structure of vitreous silica. The accurate description of the Raman coupling allowed us to derive an estimate for the concentration of oxygen atoms in three- and four-membered rings from the experimental spectrum. The finite field method was applied to calculate the Raman spectrum of a large model structure of vitreous boron oxide. By investigating the contributions to the Raman spectrum from vibrations of different symmetry, we could

extract from the experimental spectrum the concentration of boron atoms belonging to three-membered (boroxol) rings.

The theoretical methods presented in the first part of this thesis are of general application. In particular, it is now possible to study the dynamical evolution of an extended system in the presence of an electric field. Possible applications are the study of a liquids evolving in an electric field, of ionic conductivities, of structural relaxations in dielectric materials. Possible extensions might lead to the development of a time dependent scheme in the presence of a homogeneous electric field, and to a critical study of the exchange and correlation potential in the presence of an electric field.

# Appendix A

## Local Models for Raman susceptibilities

In this appendix we investigate simplified local models for Raman susceptibilities which can be applied to SiO<sub>2</sub> materials formed by cornersharing tetrahedra as  $\alpha$ -quartz and vitreous silica. The transferability properties of these models between different SiO<sub>2</sub> crystalline polymorphs are then discussed.

### A.1 Bond polarizability model

The bond polarizability model [90, 91] has successfully been applied to the calculation of Raman intensities in a large variety of systems [16]. In this approach, the polarizability is modeled in terms of bond contributions:

$$\alpha_{ij} = \frac{1}{3} (2\alpha_p + \alpha_l) \delta_{ij} + (\alpha_l - \alpha_p) \left( \frac{R_i R_j}{R^2} - \frac{1}{3} \delta_{ij} \right), \quad (\text{A.1})$$

where  $\mathbf{R} = \mathbf{R}_\beta - \mathbf{R}_\alpha$  is a vector which defines the direction and the distance of a pair of nearest neighbor atoms at sites  $\mathbf{R}_\alpha$  and  $\mathbf{R}_\beta$ . The parameters  $\alpha_l$  and  $\alpha_p$  correspond to the longitudinal and perpendicular bond polarizability, respectively.

The bond polarizability model further assumes that the bond polarizabilities  $\alpha_l$  and  $\alpha_p$  only depend on the length of the bond. Thus, the derivative of the bond polarizability

Table A.1: Parameters of the bond polarizability model derived for  $\alpha$ -quartz (BP) and for a cristobalite structure of space group  $F\bar{4}d2$  (BPC). For the purpose of comparison, the parameters derived for the cristobalite structure are rescaled to account for the volume of the primitive cell of  $\alpha$ -quartz. The values are given in  $(4\pi)^{-1}\cdot 10^{-3} \times \text{bohr}^{-1}$ .

Model	$\alpha$	$\beta$	$\gamma$
BP	771	196	56
BPC	773	144	34

with respect to the displacement of the atom  $\beta$  reads:

$$\begin{aligned} \frac{\partial \alpha_{ij}}{\partial R_{\beta k}} &= \frac{1}{3} (2\alpha'_p + \alpha'_l) \delta_{ij} \hat{R}_k + \\ &+ (\alpha'_l - \alpha'_p) (\hat{R}_i \hat{R}_j - \frac{1}{3} \delta_{ij}) \hat{R}_k + \\ &+ \frac{(\alpha_l - \alpha_p)}{R} (\delta_{ik} \hat{R}_j + \delta_{jk} \hat{R}_i - 2\hat{R}_i \hat{R}_j \hat{R}_k), \end{aligned} \quad (\text{A.2})$$

where  $\hat{\mathbf{R}}$  is a unit vector along  $\mathbf{R}$ , and  $\alpha'_l$  and  $\alpha'_p$  are the derivatives of the bond polarizabilities with respect to the bond length. Therefore, when one type of bond occurs, the bond polarizability model is completely defined by only three parameters:

$$\alpha = 2\alpha'_p + \alpha'_l, \quad \beta = \alpha'_l - \alpha'_p, \quad \gamma = (\alpha_l - \alpha_p)/R. \quad (\text{A.3})$$

We determined the parameters of the bond polarizability model for  $\alpha$ -quartz as follows. Adopting the standard tensorial norm, we minimized the deviations of the tensor  $\partial\chi/\partial\mathbf{r}$  with respect to our first-principles results given in Section 4.1. The parameters obtained in this way are given in Table A.1. In the following, we refer to this specific bond polarizability model as to the BP model. The deviations of tensor  $\partial\chi/\partial\mathbf{r}$  for Si and O atoms are 50% and 16%, respectively.

It is more significant to quantify the accuracy of the BP model on the basis of the Raman intensities. To this end, we used the same set of intensities as in Eq. (4.13). We first compared the intensities resulting from the BP model with those obtained by first-principles, finding a relative deviation of 15%. This deviation is small, despite the rather

large deviation found for the derivatives of the polarizability tensor with respect to the displacements of Si atoms. This effect results from a combination of factors. The tensors in Table 4.5 are intrinsically larger for O than for Si atoms. The contributions of the O atoms to the Raman intensities are further enhanced by the larger number of O atoms in the unit cell and by their lighter atomic mass.

We also compared the intensities of the BP model with experimental data [78]. We calculated  $\Delta$  as in Eq. (4.13) with the same scaling factor  $f$  as obtained previously, finding  $\Delta=25\%$ . As expected, this value of  $\Delta$  obtained within the BP model is worse than the corresponding value obtained by first principles (13%).

The parameters of the bond polarizability model are usually obtained by fitting the experimental intensities. Following this procedure, the parameters of the bond polarizability model remain indeterminate by a scaling factor, because the experimental intensities are only known on a relative scale. By minimizing  $\Delta$  in Eq. (4.13), we found a deviation of 20%, independent of the scaling factor  $f$ . It is worth noting that this deviation is substantially larger than the deviation found for the first-principles intensities (13%).

## A.2 Model dependent on local symmetry

In SiO<sub>2</sub> polymorphs composed of cornersharing tetrahedra, the Si atoms are at the centers of tetrahedra while the O atoms are at their vertices. The Si-O bond length and the O-Si-O angles generally do not deviate significantly from  $\sim 1.6$  Å and the tetrahedral angle, respectively. The great variety of such polymorphs results from the flexibility of the Si-O-Si angle and from the formation of different bonding networks.

Table A.2: Parameters of the local symmetry (LS) model obtained from first-principles results for  $\alpha$ -quartz. The parameters are given in  $(4\pi)^{-1} \cdot 10^{-2} \times \text{bohr}^{-1}$ .

s	O <sub>1</sub>	O <sub>2</sub>	O <sub>3</sub>	O <sub>4</sub>	O <sub>5</sub>
3.22	8.82	4.55	9.94	3.83	1.34

In the attempt of improving upon the bond polarizability model, we introduce a model for the tensor  $\partial\chi/\partial\mathbf{r}$ , based on the ideal symmetry of the first neighbor shells. In the following, we refer to this model as to the local symmetry (LS) model. In the case of Si atoms, we assumed the symmetry of the ideal tetrahedron ( $T_d$ ), while we took the  $C_{2v}$  symmetry group for describing the environment of the O atoms. We express the derivatives of the polarizability tensor with respect to Si and O displacements,  $\partial\chi/\partial\mathbf{r}_{\text{Si}}$  and  $\partial\chi/\partial\mathbf{r}_{\text{O}}$ , in terms of invariant tensors [92]. The third-order tensor  $\partial\chi/\partial\mathbf{r}$  transforms like a product of three polar vectors and is symmetric for exchanges of two of them.

Table A.3: Deviations  $\Delta\partial\chi/\partial\mathbf{r}$  for Si and O atoms with respect to the corresponding first-principles tensors of  $\alpha$ -quartz, as found for the bond polarizability (BP) and for the local symmetry (LS) models using the standard tensorial norm. Deviations of the intensities  $\Delta I$  with respect to first-principles and experimental results are determined using Eq. (4.13). The deviations are given in percent.

	BP	LS
with respect to first-principles		
$\Delta\partial\alpha/\partial\mathbf{r}(\text{Si})$	50	50
$\Delta\partial\alpha/\partial\mathbf{r}(\text{O})$	16	12
$\Delta I$	15	12
with respect to experiment		
$\Delta I$	25	23

By applying group theory, the form of the invariant tensors can be determined. For Si atoms a single invariant tensor is found, requiring the use of a single parameter for a full description. When the bonds of the Si atoms are oriented along the  $(1\ 1\ 1)$ ,  $(\bar{1}\ \bar{1}\ 1)$ ,  $(\bar{1}\ 1\ \bar{1})$  and  $(1\ \bar{1}\ \bar{1})$  directions, the explicit form of the tensor  $[(\partial\chi/\partial x), (\partial\chi/\partial y), (\partial\chi/\partial z)]$



reads:

$$\left[ \left( \begin{array}{cc} & \\ & s \\ s & \end{array} \right), \left( \begin{array}{cc} & s \\ & \\ s & \end{array} \right), \left( \begin{array}{cc} & s \\ & \\ s & \end{array} \right) \right]. \quad (\text{A.4})$$

In the case of O atoms, the lower symmetry allows as much as five different invariant tensors, and the full tensor thus remains indeterminate by five parameters. In order to obtain an explicit form, we located the O atom on the positive  $z$  axis and took the  $x$  axis along the segment connecting its Si neighbors. For this orientation, the tensor  $\partial\chi/\partial\mathbf{r}$  reads:

$$\left[ \left( \begin{array}{cc} & o_4 \\ & \\ o_4 & \end{array} \right), \left( \begin{array}{cc} & \\ & o_5 \\ & \\ o_5 & \end{array} \right), \left( \begin{array}{cc} o_1 & \\ & o_2 \\ & \\ & o_3 \end{array} \right) \right]. \quad (\text{A.5})$$

For SiO<sub>2</sub> polymorphs composed of cornersharing tetrahedra, the bond polarizability model results from the LS model as a special case. The following relations between the parameters hold:

$$\begin{aligned} s &= 2\sqrt{3}(\beta - 2\gamma)/9 \\ o_1 &= (\cos\theta)[\beta(3\sin^2\theta - 1) + \alpha - 6\gamma\sin^2\theta]/3 \\ o_2 &= (\cos\theta)(\alpha - \beta)/3 \\ o_3 &= (\cos\theta)[\beta(3\cos^2\theta - 1) + \alpha + 6\gamma]/3 - 2\gamma\cos^3\theta \\ o_4 &= (\cos\theta)[(\beta - 2\gamma)\sin^2\theta + \gamma] \\ o_5 &= \gamma\cos\theta, \end{aligned} \quad (\text{A.6})$$

where  $2\theta$  is the Si-O-Si angle.

The free parameters of the LS model, in Eqs. (A.4) and (A.5), are obtained from our first-principles results in Table 4.5 by symmetrization. The values of these parameters are reported in Table A.2. The deviations of the LS model tensors with respect to the tensors obtained by first principles reflect the significance of the contributions of the global environment which do not satisfy the symmetry of the first-neighbor shell. In order to estimate these deviations, we adopted the standard tensorial norm and found a relative

deviation of 50% and 12% for Si and O atoms, respectively. Because the BP model is a special case of the more general LS model, the latter necessarily provides a better description, as can be seen from the comparison in Table A.3. However, despite the use of six parameters instead of three, the LS deviations only marginally improve upon the BP ones.

This limited improvement is also evident when focusing on the intensities. The deviations of the LS and BP intensities do not differ significantly, neither when calculated with respect to the first-principles intensities nor to the experimental ones (Table A.3).

### A.3 Transferability

In order to examine the transferability of the simple models, we here consider in detail another SiO<sub>2</sub> polymorph composed of cornersharing tetrahedra. Because we were unable to find in the literature a polymorph other than  $\alpha$ -quartz for which detailed experimental Raman activities were available, we chose to consider a cristobalite structure of space group  $F\bar{4}d2$  [93, 94], and to use Raman activities calculated from first principles as reference. This cristobalite structure offers the computational advantage of a unit cell containing just two formula units and the possibility of selecting the Si-O-Si angle by applying an appropriate tensile or compressive strain [85]. We fixed the cubic lattice parameter at  $a=6.97$  Å, and relaxed the internal degree of freedom. The electronic structure was described with the same technical ingredients used for  $\alpha$ -quartz. The Brillouin zone was sampled with two special  $k$ -points at  $(\frac{1}{4}, \frac{1}{4}, \frac{1}{4})$  and  $(\frac{1}{2}, \frac{1}{2}, \frac{1}{4})$  with respective weights of  $\frac{1}{4}$  and  $\frac{3}{4}$  [95].

We found a Si-O bond length of 1.58 Å and a Si-O-Si angle of 144.4° upon relaxation. We chose on purpose to work with a Si-O-Si angle close to that of  $\alpha$ -quartz (143.7°) in order to avoid the consideration of additional parameters in our investigation of the transferability of the simple models.

The vibrational modes at the  $\Gamma$  point of the Brillouin zone belong to the irreducible representations of the  $D_{2d}$  group: the nondegenerate  $A_1$ ,  $A_2$ ,  $B_1$ ,  $B_2$  modes and the doubly degenerate  $E$  mode. The calculated vibrational frequencies are reported in Table A.4 where they are ordered according to the symmetry of their eigenmodes. All the modes

but those of  $A_2$  symmetry are Raman active. Following the notation of Loudon [80], the forms of the Raman tensors read:

$$\begin{pmatrix} a & & \\ & a & \\ & & b \end{pmatrix}, \begin{pmatrix} c & & \\ & -c & \\ & & \end{pmatrix}, \begin{pmatrix} & & d \\ & & \\ d & & \end{pmatrix}, \quad (\text{A.7})$$

for the nondegenerate modes  $A_1$ ,  $B_1$  and  $B_2$ , respectively, and

$$\begin{pmatrix} & & \\ & e & \\ e & & \end{pmatrix}, \begin{pmatrix} & & e \\ & & \\ e & & \end{pmatrix}, \quad (\text{A.8})$$

for the doubly degenerate modes  $E(x)$  and  $E(y)$ , defined as in the case of  $\alpha$ -quartz. The calculated parameters for the Raman tensor of each mode are given in Table A.4. The  $A_1$  mode at  $342.6 \text{ cm}^{-1}$  and the  $E$  mode at  $135.5 \text{ cm}^{-1}$  are the strongest Raman lines.

We used our first-principles results as a reference to test the transferability of the BP and LS models. Using the standard tensorial norm, we calculated the deviations  $\Delta\partial\chi/\partial\mathbf{r}$  with respect to the first-principles tensors. The accuracy of the BP and LS models were found to be similar, with deviations of 32 and 23% for Si and O atoms, respectively. In order to quantify the deviation with respect to the first-principles intensities, we calculated an average deviation  $\Delta I$  as in Eq. (4.13) using all the entries in Table A.4. We found a deviation of 16 and 25% for the BP and LS models, respectively. Table A.5 summarizes the results of these transferability tests. From Table A.5, it clearly appears that the LS model which depends on six parameters does not bring any advantage with respect to the three-parameter BP model. The BP model reproduced the first-principles intensities of  $\alpha$ -quartz and cristobalite with a similar deviation (15 and 16%, respectively). The intensities calculated with the BP model are shown in Table A.4, where they are compared with the first principles results. By comparison, the LS model reproduced the first-principles intensities of cristobalite with a deviation of 25%, substantially larger than the corresponding deviation found for  $\alpha$ -quartz (12%).

We further examined the transferability of the bond polarizability model by extracting a new set of parameters  $\alpha$ ,  $\beta$ , and  $\gamma$  from the tensors  $\partial\chi/\partial\mathbf{r}$  calculated for the cristobalite

structure. The parameters of this new bond polarizability model, which we refer to as the BPC model, are reported in Table A.1, where they are rescaled to the volume of the primitive cell of  $\alpha$ -quartz for permitting a comparison with the parameters of the BP model. The difference between the parameters  $\alpha$ ,  $\beta$  and  $\gamma$  are smaller than 3% with respect to the size of the largest parameter  $\alpha$ . We also added in Table A.5 the deviations  $\Delta\partial\chi/\partial\mathbf{r}$  and  $\Delta I$  for the BPC model. This comparison shows that the BPC model, which corresponds to the optimal bond polarizability model for the cristobalite structure, only marginally improves upon the BP model originally derived for  $\alpha$ -quartz. All these results provide additional evidence in support of the transferability of the bond polarizability model.

While the LS model slightly improves upon the BP model in describing the Raman intensities of  $\alpha$ -quartz, it now clearly appears that this is achieved at the cost of degrading the transferability properties. We attribute the better transferability properties of the bond polarizability model to the validity of the underlying physical picture.

We here only addressed two structures with close Si-O-Si bond angles. It is of interest to extend the simple models to structures with different angles. In principle, the parameters of the simple models should be optimized for each angle separately. However, in the case of the bond polarizability model, this angular dependence follows from the physical picture on which the model is based (Eqs. A.6).

Table A.4: Transverse-optic vibrational frequencies at the  $\Gamma$  point and corresponding Raman intensities for a cristobalite structure of space group  $F\bar{4}d2$  [93, 94]. Intensities obtained by first principles and by applying the bond polarizability model BP, originally derived for  $\alpha$ -quartz, are compared. The absolute Raman intensities per unit volume can be obtained by multiplying the values in the table by  $\omega_S^4$  and by  $1/f=2.368\cdot 10^{-70}$   $\text{sterad}^{-1}\text{cm}^{-1}\text{s}^4$ .

Symmetry	Mode		Calculated intensity	
	Frequency ( $\text{cm}^{-1}$ )		First-principles	BP
$A_1$	342.6	$a^2$	1501.6	1630.3
		$b^2$	1241.4	1001.0
$A_2$	1158.3	Raman inactive		
	359.8	Raman inactive		
$B_1$	1114.0	$c^2$	38.9	70.7
	445.9		24.5	13.9
$B_2$	779.2	$d^2$	4.2	5.3
	442.3		0.0	33.6
$E$	1144.0	$e^2$	5.6	16.8
	815.8		38.1	24.6
	474.4		0.8	1.5
	135.5		281.8	100.5

Table A.5: Deviations  $\Delta\partial\chi/\partial\mathbf{r}$  and  $\Delta I$  with respect to first-principles results for a cristobalite structure of space group  $F\bar{4}d2$ , as found for the local symmetry (LS) and the bond polarizability (BP and BPC) models. The parameters of the BP and BPC models were derived for the  $\alpha$ -quartz and cristobalite structures, respectively. The deviations were calculated as in Table A.3.

	LS	BP	BPC
$\Delta\partial\boldsymbol{\alpha}/\partial\mathbf{r}(\text{Si})$	32	32	30
$\Delta\partial\boldsymbol{\alpha}/\partial\mathbf{r}(\text{O})$	23	23	19
$\Delta I$	25	16	10

## Appendix B

# Minimization of second order variational functionals

In this appendix, we address the minimization of a generic second order energy functional with respect to a generic perturbation, for the case of ultrasoft pseudopotentials. In the case of ultrasoft pseudopotentials, a generic second order variational functional (using the notation of Chapter 2) reads:

$$E^2 = \sum_v \left( \langle \tilde{\Psi}_v^1 | H^0 - \epsilon_v^0 S^0 | \tilde{\Psi}_v^1 \rangle + \langle \tilde{\Psi}_v^1 | H^1 - \epsilon_v^0 S^1 | \tilde{\Psi}_v^0 \rangle + \langle \tilde{\Psi}_v^0 | H^1 - \epsilon_v^0 S^1 | \tilde{\Psi}_v^1 \rangle \right), \quad (\text{B.1})$$

where the index  $v$  runs over the valence states. The first order wave functions  $\tilde{\Psi}_v^1$  must satisfy the following constraints:

$$\langle \tilde{\Psi}_v^1 | S^0 | \tilde{\Psi}_{v'}^0 \rangle + \langle \tilde{\Psi}_v^0 | S^0 | \tilde{\Psi}_{v'}^1 \rangle + \langle \tilde{\Psi}_v^0 | S^1 | \tilde{\Psi}_{v'}^0 \rangle = 0. \quad (\text{B.2})$$

These constraints can be imposed by introducing appropriate Lagrange multipliers in  $E^2$ :

$$E'^2 = \sum_v \left( \langle \tilde{\Psi}_v^1 | H^0 - \epsilon_v^0 S^0 | \tilde{\Psi}_v^1 \rangle + \langle \tilde{\Psi}_v^1 | H^1 - \epsilon_v^0 S^1 | \tilde{\Psi}_v^0 \rangle + \langle \tilde{\Psi}_v^0 | H^1 - \epsilon_v^0 S^1 | \tilde{\Psi}_v^1 \rangle \right) (\text{B.3}) \\ - \sum_{v,v'} \lambda_{v,v'} \left( \langle \tilde{\Psi}_v^1 | S^0 | \tilde{\Psi}_{v'}^0 \rangle + \langle \tilde{\Psi}_v^0 | S^0 | \tilde{\Psi}_{v'}^1 \rangle + \langle \tilde{\Psi}_v^0 | S^1 | \tilde{\Psi}_{v'}^0 \rangle \right).$$

The gradient  $\delta E'^2 / \delta \langle \tilde{\Psi}_i^1 |$  reads:

$$\frac{\delta E'^2}{\delta \langle \tilde{\Psi}_i^1 |} = (H^0 - \epsilon_v^0 S^0) | \tilde{\Psi}_v^1 \rangle + (H^1 - \epsilon_v^0 S^1) | \tilde{\Psi}_v^0 \rangle - \sum_{v'} \lambda_{v,v'} S^0 | \tilde{\Psi}_{v'}^0 \rangle \quad (\text{B.4})$$

At the minimum,  $\delta E'^2/\delta\langle\tilde{\Psi}_i^1|$  vanishes and the Lagrange multipliers are given by:

$$\lambda_{v,v'} = \langle\tilde{\Psi}_v^0|H^0 - \epsilon_v^0 S^0|\tilde{\Psi}_{v'}^1\rangle + \langle\tilde{\Psi}_v^0|H^1 - \epsilon_v^0 S^1|\tilde{\Psi}_{v'}^0\rangle. \quad (\text{B.5})$$

By inserting (B.5) in Eq. (B.4), we find that, at the minimum the following relation holds:

$$\left(1 - \sum_{v'} S^0|\tilde{\Psi}_{v'}^0\rangle\langle\tilde{\Psi}_{v'}^0|\right) \left(H^0 - \epsilon_v^0 S^0|\tilde{\Psi}_v^1\rangle + (H^1 - \epsilon_v^0 S^1)|\tilde{\Psi}_v^0\rangle\right) = 0, \quad (\text{B.6})$$

where the second term in parenthesis is equal to the gradient  $\delta E^2/\delta\langle\tilde{\Psi}_v^1|$ . We define the following projector operator, as done in Ref. [56]:

$$P_c^\dagger = 1 - S^0 \sum_{v'} |\tilde{\Psi}_{v'}^0\rangle\langle\tilde{\Psi}_{v'}^0| \quad (\text{B.7})$$

At the minimum the projection of the gradient  $\delta E^2/\delta\langle\tilde{\Psi}_v^1|$  by the operator  $P_c^\dagger$  must vanish:

$$P_c^\dagger \frac{\delta E^2}{\delta\langle\tilde{\Psi}_v^1|} = 0 \quad (\text{B.8})$$

For minimizing  $E^2$ , within a Car-Parrinello scheme, we start from a set of trial states  $\tilde{\Psi}_v^1$  which satisfy (B.2). Then, we update, at each time step, the first order wave functions by considering the fictitious dynamics:

$$\mu \frac{d^2 \tilde{\Psi}_v^1}{dt^2} = -P_c^\dagger \frac{\delta E^2}{\delta\langle\tilde{\Psi}_v^1|}, \quad (\text{B.9})$$

where  $\mu$  is the fictitious mass of the electrons, and the constraints (B.2) are imposed, at each time step, on the updated wave functions. We found that this approach is equivalent to a minimization of  $E^2$  based on an explicit calculation of the lagrange multipliers at each time step.



# Bibliography

- [1] W.H. Zachariasen, *J. Am. Chem. Soc.* **54**, 3841 (1932).
- [2] S. V. King, *Nature* **213**, 1112 (1967).
- [3] R.H. Stolen, J.T. Krause, and C.R. Kurkjian, *Discuss. Faraday Soc.* **50**, 103 (1970).
- [4] F.L. Galeener and G. Lukovsky, *Phys. Rev. Lett.* **37**, 1474 (1976).
- [5] F.L. Galeener, *Solid State Commun.* **44**, 1037 (1982). *J. Non-Cryst. Solids* **49**, 53 (1982).
- [6] A. Pasquarello and R. Car, *Phys. Rev. Lett.* **80**, 5145 (1998).
- [7] C.T. Kirk, *Phys. Rev. B* **38**, 1255 (1988).
- [8] J.M. Carpenter and D.L. Price, *Phys. Rev. Lett.* **54**, 441 (1985).
- [9] C.F. Windisch Jr. and W.M. Risen Jr., *J. Non-Cryst. Solids* **48**, 307 (1982)
- [10] S.R. Elliott, *Philos. Mag. B* **37**, 425 (1978)
- [11] J. Swenson and L. Börjesson, *Phys. Rev. B* **55**, 11138 (1997).
- [12] K. Suzuya, Y. Yoneda, S. Kohara, and N. Umesaki, *Phys. Chem. Glas.* **41**, 282 (2000).
- [13] G.E. Jellison Jr., L.W. Panek, P.J. Bray and G.B. Rouse Jr, *J. Chem. Phys.* **66**, 802 (1977).

- [14] A.C. Hannon, D.I. Grimley, R.A. Hulme, A.C. Wright, and R.N. Sinclair, *J. Non-Cryst. Solids* **177**, 299 (1994).
- [15] M.C. Tobin and T. Baak *J. Opt. Soc. Am.* **60**, 368 (1970).
- [16] “*Light Scattering in Solids II*”, editors: M. Cardona and G. Güntherodt (Springer-Verlag, Berlin, 1982).
- [17] G. Placzek, *Handbuch der Radiologie* edited by E. Marx, (Akad. Verlagsgesellschaft, Leipzig) **6**, Pt. 2, 205 (1934).
- [18] R. Car and M. Parrinello, *Phys. Rev. Lett.* **55**, 2471 (1985).
- [19] S. Baroni, P. Giannozzi and A. Testa, *Phys. Rev. Lett.* **58**, 1861 (1987).
- [20] A. Pasquarello, K. Laasonen, R. Car, C. Lee, and D. Vanderbilt, *Phys. Rev. Lett.* **69**, 1982 (1992); K. Laasonen, A. Pasquarello, R. Car, C. Lee, and D. Vanderbilt, *Phys. Rev. B* **47**, 10142 (1993).
- [21] J. Sarnthein, A. Pasquarello, and R. Car, *Phys. Rev. Lett.* **74**, 4682 (1995); *Phys. Rev. B* **52**, 12690 (1995).
- [22] J. Sarnthein, A. Pasquarello, and R. Car, *Science* **275**, 1925 (1997); A. Pasquarello, J. Sarnthein, and R. Car, *Phys. Rev. B* **57**, 14133 (1998).
- [23] A. Pasquarello and R. Car, *Phys. Rev. Lett.* **79**, 1766 (1997).
- [24] X. Gonze and C. Lee, *Phys. Rev. B* **55**, 10355 (1997).
- [25] P. Umari and A. Pasquarello, *Phys. Rev. Lett.* **89** 157602 (2002).
- [26] P. Umari, A. Pasquarello, and A. Dal Corso, *Phys. Rev. B* **63**, 94305 (2001).
- [27] P. Umari, X. Gonze, and A. Pasquarello, *Phys. Rev. Lett.* **90** 07401 (2003).
- [28] P.E. Blöchl, *Phys. Rev. B* **50**, 17953 (1994).

- [29] F. Mauri and S.G. Louie, Phys. Rev. Lett. **76**, 4246 (1996); F. Mauri, B.G. Pfroemer, and S.G. Louie, Phys. Rev. Lett. **77**, 5300 (1996).
- [30] O.K. Andersen, Phys. Rev. B **12**, 3060 (1975).
- [31] D. Vanderbilt, Phys. Rev. B **41**, 7892 (1990).
- [32] Other differences between the PAW and the US methods are discussed in: G. Kresse and D. Joubert, Phys. Rev. B **59**, 1758 (1999).
- [33] X. Gonze, Phys. Rev. B **55**, 10337 (1997).
- [34] W.F. Murphy, Mol. Phys. **33**, 1701 (1977); *ibid* **36**, 727 (1978).
- [35] A. Briley, M.R. Pederson, K.A. Jackson, D.C. Patton, and D.V. Porezag, Phys. Rev. B **58**, 1786 (1998).
- [36] A. Stirling, J. Chem. Phys. **104**, 1254 (1996).
- [37] D. Berejemo, R. Escibano, and J.M. Orza, J. Mol. Spec. **65**, 345 (1977).
- [38] *Handbook of Chemistry and Physics*, edited by D. R. Lide (CRC Press, New York, 1998), p. 12-52.
- [39] H.J. Bernstein, in *Vibrational Intensities in Infrared and Raman Spectroscopy*, edited by W.B. Person and G. Zerbi (Elsevier, Amsterdam , 1982).
- [40] R. Resta and A. Baldereschi, Phys. Rev. B **23**, 6615 (1981).
- [41] A. Dal Corso and F. Mauri, Phys. Rev. B **50**, 5756 (1994); A. Dal Corso, F. Mauri, and A. Rubio, Phys. Rev. B **53**, 15638 (1996).
- [42] A. Putrino, D. Sebastiani, and M. Parrinello, J. Chem. Phys. **113**, 7102 (2000).
- [43] G. H. Wannier, Phys. Rev. **117**, 432 (1960).
- [44] G. Nenciu, Rev. Mod. Phys. **63**, 91 (1991).
- [45] R. W. Nunes and D. Vanderbilt, Phys. Rev. Lett. **73**, 712 (1994).

- [46] R. D. King-Smith and D. Vanderbilt, *Phys. Rev. B* **47**, 1651 (1993); R. Resta, *Ferroelectrics* **111**, 15 (1992); A.K. Tagantsev, *Phase Transitions* **35**, 119 (1991); M. Posternak *et al.*, *Phys. Rev. Lett.* **64**, 1777 (1990).
- [47] R. Resta, *Rev. Mod. Phys.* **66**, 899 (1994).
- [48] P. Fernández, A. Dal Corso, and A. Baldereschi, *Phys. Rev. B* **58**, R7480 (1998).
- [49] R. W. Nunes and X. Gonze, *Phys. Rev. B* **63**, 155107 (2001).
- [50] R. Resta, *Berry Phase in Electronic Wavefunctions*, (Troisième Cycle de la Physique en Suisse Romande, Lausanne, 1996); *Phys. Rev. Lett.* **80**, 1800 (1998).
- [51] X. Gonze and J.-P. Vigneron, *Phys. Rev. B* **39**, 13120 (1989).
- [52] I. Souza, J. Íñiguez, and D. Vanderbilt, *Phys. Rev. Lett.* **89**, 117602 (2002).
- [53] H.R. Philipp, in *Handbook of Optical Constants of Solids*, edited by D. Palik (Academic Press, San Diego, 1998), p. 749.
- [54] D. Porezag and M.R. Pederson, *Phys. Rev. B* **54**, 7830 (1996).
- [55] I.J. John, G.B. Backsay, and N.S. Hush, *Chem. Phys.* **51**, 49 (1980).
- [56] A. Dal Corso, A. Pasquarello, A. Baldereschi and R. Car, *Phys. Rev. B* **53**, 1180 (1996).
- [57] M. E. Lines, *Phys. Rev. B* **41**, 3372 (1990); *Handbook of Chemistry and Physics*, edited by D. R. Lide (CRC Press, New York, 1998), p. 12-52.
- [58] H.W. Icenogle, B.C. Platt, and W.L. Wolfe, *Appl. Opt.* **15**, 2384 (1976).
- [59] G. B. Bachelet, D. R. Hamann, and M. Schlüter, *Phys. Rev. B* **26**, 4199 (1982).
- [60] H.J. Monkhorst and J.D. Pack, *Phys. Rev. B* **13**, 5188 (1976).
- [61] N.Sai, K.M. Rabe, and D.Vanderbilt, *Phys. Rev. B* **66**, 104108 (2002).
- [62] A. Dal Corso, S. Baroni, and R. Resta, *Phys. Rev. B* **49** 5323 (1994).

- [63] A. Pasquarello, M.S. Hybertsen, and R. Car, *Nature* **396**, 58 (1998); A. Pasquarello, I. Petri, P. S. Salmon, O. Parisel, R. Car, E. Tóth, D. H. Powell, H. E. Fischer, L. Helm, A. E. Merbach, *Science* **291**, 856 (2001).
- [64] M. Born and K. Huang, *Dynamical Theory of Crystal Lattices*, (Oxford University Press, Oxford, 1954).
- [65] W. Cochran and R. A. Cowley, *J. Phys. Chem. Solids* **23**, 447 (1962).
- [66] Ph. Ghosez, J.-P. Michenaud and X. Gonze, *Phys. Rev. B* **58**, 6224 (1998).
- [67] *Phonons: Theory and Experiments II*, edited by P.Brüesch (Springer-Verlag, Berlin, 1986).
- [68] W.G. Wyckoff, *Crystal Structures* (Interscience, New York, 1974), 4th ed.
- [69] J. P. Perdew and A. Zunger, *Phys. Rev. B* **23**, 5048 (1981).
- [70] We used the PWSCF and PHONON codes developed by S. Baroni, P. Giannozzi, S. de Gironcoli, A. Dal Corso and others.
- [71] N. Troullier and J. L. Martin, *Phys. Rev. B* **43**, 8861 (1991).
- [72] L. Levien, C. T. Prewitt and D. Weidner, *Am. Mineral.* **65**, 920 (1980).
- [73] X. Gonze, D. C. Allan and M. P. Teter, *Phys. Rev. Lett.* **68**, 3603 (1992).
- [74] P. Giannozzi, S. de Gironcoli, P. Pavone, and S. Baroni, *Phys. Rev. B* **43**, 7231 (1991).
- [75] F. Gervais and B. Piriou, *Phys. Rev. B* **11**, 3944 (1975).
- [76] X. Gonze, P. Ghosez and R. W. Godby, *Phys. Rev. Lett.* **74** 4035 (1995).
- [77] E. K. Zakharova, V. G. Zubov and L. P. Osipova, *Sov. Phys. Crystallogr.* **19**, 489 (1975).
- [78] J.D. Masso, C.Y. She, and D.F. Edwards, *Phys. Rev. B* **1**, 4179 (1970).

- [79] S. Baroni and R. Resta, Phys. Rev. B **33**, 5969 (1986).
- [80] R. Loudon, Advan. Phys. **13**, 423 (1964).
- [81] P. Giannozzi and S. Baroni, J. Chem. Phys. **100**, 8537 (1994).
- [82] V.S. Gorelik and M.M. Sushchinskii Sov. Phys. Solid State **12** 1157 (1970).
- [83] J. C. Mikkelsen, Jr. and F. L. Galeener, J. Non-Crystal. Solids **37**, 71 (1980).
- [84] A. Bongiorno and A. Pasquarello, Phys. Rev. Lett. **88**, 125901 (2002).
- [85] F. Mauri, A. Pasquarello, B.G. Pfrommer, Y-G Yoon and S.G. Louie, Phys. Rev. B **62**, R4786 (2000).
- [86] R.L. Mozzi and B.E. Warren, J. Appl. Crystallogr. **2**, 164 (1969); E. Dupree and R.F. Pettifer, Nature **308**, 523 (1984).
- [87] J. P. Rino, *et al.*, Phys. Rev. B **47**, 3053 (1993).
- [88] K. Vollmayr, W. Kob, and K. Binder, Phys. Rev. B **54**, 15808 (1996).
- [89] J.R. Bell, P. Dean and Hibbins-Butler *J. Phys. C* **4**, 1241 (1971); J.R. Bell and Hibbins-Butler *J. Phys. C* **8**, 787 (1975).
- [90] M. V. Wolkenstein, C. R. Acad. Sc. U.R.S.S. **30**, 791 (1941).
- [91] M. A. Eliashevich and M. V. Wolkenstein, J. Phys. URSS **9**, 101 (1944).
- [92] M. Lax, *Symmetry principles in solid state and molecular physics*, (Wiley, New York, 1974).
- [93] A.F. Wright and A.J. Leadbetter, Philos. Mag. **31**, 1391 (1975).
- [94] F. Liu, S.H. Garofalini, R.D. King-Smith, and D. Vanderbilt, Phys. Rev. Lett. **70**, 2750 (1993).
- [95] R.A. Evarestov and V.P. Smirnov, Phys. Status Solidi B **119**, 9 (1983).

- [96] C.T. Prewitt and R.D. Shannon, *Acta Crystallogr. B* **24**, 869 (1968).
- [97] P.A.V. Johnson, A.C. Wright, and R.N. Sinclair, *J. Non-Crystal. Solids* **50**, 281 (1982).
- [98] J.P. Perdew and Y. Wang (unpublished); J.P. Perdew, in *Electronic Structure of Solids '91*, edited by P. Ziesche and H. Eschrig (Akademie Verlag, Berlin, 1991).
- [99] D.L. Price and J.M. Carpenter, *J. Non-Crystal. Solids* **92**, 153 (1987).
- [100] A. Pasquarello, *Phys. Rev. B* **61**, 3951 (2000).
- [101] A. Pasquarello, J. Sarnthein, and R. Car, *Phys. Rev. B* **57**, 14133 (1998).
- [102] F.L. Galeener, G. Lucovsky, and C. Mikkelsen Jr., *Phys. Rev. B* **22**, 3983 (1980).
- [103] M.F. Thorpe and S.W. de Leeuw, *Phys. Rev. B* **33**, 8490 (1986).
- [104] G.E. Walrafen, S.R. Samanta, and P.N. Krishnan, *J. Chem. Phys.* **72**, 1 (1980).





# Acknowledgments

I am very grateful to Alfredo for having taught me how to do research in physics. My stay in the ugly irrma building was made easy and pleasant by all (present and past) irrma people: Alain, Felix, Carol, Max, Claudia, Feliciano, Angelo, Mascha, Zeljko, Rainer, Sandro, Tristan, Vincent, Stephane, Federica, Luigi, John, Giovanni, Thomas. The best souvenir of the time spent in Lausanne are all the friends I met: Michele, Markus, Varvara, Kai, Julie, Simon, Soleil, Nevena, Jelena, Marija, Aleksandra, Rama, Slavica, Tristan, Andrea and many others. I passed many Wednesday mornings working in the fair trade shop, hoping in a more equal world, I thank all the staff of the *magasin du monde*. Finally, I am very thankful to my parents Marisa and Giorgio.



# Curriculum vitae

Name: Paolo Umari

Date and place of birth: 21.8.1974 Trieste, Italy

Citizenship: Italian

Languages: Italian, French, English, German

Education:

- 1999-2003 Ph.D. thesis under the direction of Prof. A. Pasquarello  
Swiss Federal Institute of Technology in Lausanne (EPFL)  
"Raman spectra of disordered oxides from first principles"
- 1993-1999 Undergraduate studies at the University of Trieste, Italy  
Diploma thesis under the direction of Prof R. Resta  
"Microscopic theory of dielectric polarization"  
Score: 110/110 cum laude
- 1996-1997 RWTH Aachen, Germany

### List of Publications:

- Umari P, Dal Corso A, Resta R *Inside dielectrics: microscopic and macroscopic polarization* AIP-Conference-Proceedings. **582**, 107 (2001).
- Umari P, Pasquarello A, Dal Corso A *Raman scattering intensities in alpha-quartz: A first-principles investigation* PHYSICAL REVIEW B **63**, 094305 (2001).
- Umari P, Pasquarello A *Modeling of the Raman spectrum of vitreous silica: concentration of small ring structures* PHYSICA B **316**, 572 (2002).
- Umari P, Pasquarello A *Ab initio molecular dynamics in a finite homogeneous electric field* PHYSICAL REVIEW LETTERS **89**, 157602 (2002).
- Umari P, Gonze X, Pasquarello A *Concentration of small ring structures in vitreous silica from a first-principles analysis of the Raman spectrum* PHYSICAL REVIEW LETTERS **90**, 027401 (2003).
- Umari P, Pasquarello A *First-principles analysis of the Raman spectrum of vitreous silica: comparison with the vibrational density of states* JOURNAL OF PHYSICS: CONDENSED MATTER **15**, S1547 (2003).
- Umari P, Pasquarello A *Car-Parrinello Molecular Dynamics in a Finite Homogeneous Electric Field* AIP-Conference-Proceedings, 'Fundamental Physics of Ferroelectrics 2003' accepted .
- Umari P, Pasquarello A *Polarizability and dielectric constant in density-functional supercell calculations with discrete k-point samplings* PHYSICAL REVIEW B accepted.